DOCTORAL SCHOOL
UNIVERSITÀ *MEDITERRANEA* DI REGGIO CALABRIA

DIPARTIMENTO DI INGEGNERIA DELL'INFORMAZIONE, DELLE INFRASTRUTTURE E DELL'ENERGIA SOSTENIBILE (DIIES)

PHD IN
INFORMATION ENGINEERING

S.S.D. ING-INF/02
XXX CICLO

SYNTHESIS OF INNOVATIVE ELECTROMAGNETIC DEVICES VIA INVERSE SCATTERING TECHNIQUES

CANDIDATE
Roberta PALMERI

ADVISOR
Prof. Tommaso ISERNIA

COORDINATOR
Prof. Claudio DE CAPUA

REGGIO CALABRIA, APRIL 2018

Finito di stampare nel mese di **Aprile 2018**

Edizione 

Quaderno N. 35
Collana *Quaderni del Dottorato di Ricerca in Ingegneria dell'Informazione*
Curatore *Prof. Claudio De Capua*

ISBN 978-88-99352-23-3

Università degli Studi *Mediterranea* di Reggio Calabria
Salita Melissari, Feo di Vito, Reggio Calabria

ROBERTA PALMERI

SYNTHESIS OF INNOVATIVE ELECTROMAGNETIC DEVICES VIA INVERSE SCATTERING TECHNIQUES

The Teaching Staff of the PhD course in
INFORMATION ENGINEERING
consists of:

Claudio DE CAPUA (coordinator)
Giovanni ANGIULLI
Pier Luigi ANTONUCCI
Giuseppe ARANITI
Francesco BUCCAFURRI
Rosario CARBONE
Riccardo CAROTENUTO
Salvatore COCO
Francesco DELLA CORTE
Fabio FILIANOTI
Sofia GIUFFRE'
Antonio IERA
Tommaso ISERNIA
Gianluca LAX
Aime' LAY EKUAKILLE
Giacomo MESSINA
Antonella MOLINARO
Andrea Francesco MORABITO
Rosario MORELLO
Fortunato PEZZIMENTI
Sandro RAO
Domenico ROSACI
Giuseppe RUGGERI
Francesco RUSSO
Valerio SCORDAMAGLIA
Domenico URSINO

Insegnami la dolcezza ispirandomi la caritá,
insegnami la disciplina dandomi la pazienza
e insegnami la scienza illuminandomi la mente.
Sant'Agostino

Acknowledgment

At the end of my PhD studies, thanks are due to those people that have allowed the drafting of this thesis.

First of all, my absolute gratitude is to my advisor Prof. Tommaso Isernia, for having given me the possibility of join his research team and taught me how to scientifically face any problem, with unfailing support and dedication along the way. All the stimulating interactions I had with him have provided the keys to open the not yet explored parts of my mind.

During my PhD research activity, I was surrounded by precious coworkers. My greatest thanks to Dr. Martina Bevacqua. She has been a reference point for me from the beginning and working together, day by day, has made me grown a lot. I wish to express also my gratitude to Dr. Andrea Morabito for his kindness and support. Working with him, even if for a short time, it has been an honor. In covering all the LEMMA Research Group, my sincere thanks also go to my laboratory colleagues, Engs. Gennaro Bellizzi and Giada Battaglia, for the great time we spent together and for all the not-only professional discussions we had.

Moreover, I am thankful to Prof. Gino Sorbello and Dr. Loreto Di Donato. I will never forget my origin, so I would sincerely thank them for the time they dedicated me during the Bachelor and Master thesis, respectively, thus allowing me to explore the amazing world of electromagnetism.
I would like to thank also Dr. Lorenzo Crocco for the stimulating and fruitful discussions and for his invaluable collaborations during these years, partially testified in this thesis.

But in life there is more than work. So, my sincere thanks also go to all the guys of Chemistry's Laboratory, in particular to Fabiola for having shared both beautiful and hard moments during the PhD: they have been my family in Reggio Calabria.

Last, but not least, a special thank goes to my family and Angela for their support and, in particular, to Giuseppe for always being close to me when I need and for pushing me to believe in myself.

Abstract

This Thesis deals with the synthesis of innovative microwave devices via inverse scattering based theoretical tools and actual procedures. The electromagnetic scattering phenomenon occurs when the presence of an inhomogeneity in the space originates a perturbation of the field which is propagating. In the considered region of space, a new electromagnetic field occurs and such a total field is nothing but a superposition of the original one and the perturbation caused by the obstacle (or scatterer), which is called "scattered field". The usual aim of an inverse scattering problem is to retrieve the location, the shape and the electromagnetic parameters of the scatterer by processing measurements of the scattered field. Several difficulties come into play in solving such a diagnosis problem, since the non linearity and the ill-posedness of the problem must be faced. Therefore, efficient solution strategies and regularization techniques have to be exploited to reach accurate and meaningful solutions.

Interestingly, the inverse scattering problem can be turned into a synthesis problem, provided the starting data is no longer a collection of measurements but rather some field specifications arising from design constraints. In the Thesis, some methodologies already available in the inverse scattering community for diagnosis applications are extended and modified for design purposes. Theoretical results include a new representation for non radiating sources and spectral analysis of some scattering approximations which are both of interest for design of invisibility devices. Methodological results include two new effective solution procedures for the general inverse scattering problem. Moreover, a well known inversion procedure is considerably modified and extended in order to include the synthesis of the excitations of some primary sources. Last, but not least, a new procedure is proposed for the synthesis of Artificial Materials based devices which outperforms a more intuitive homogenization based method. Finally, the developed approaches and procedures are validated through the synthesis of an optimal monopulse antennas as well as of new invisibility cloaks.

Contents

List of Figures

List of Tables

1

INTRODUCTION

1.1 Inverse scattering problems: basics and difficulties

The electromagnetic scattering [1–3] phenomenon occurs when the presence of an inhomogeneity in the space originates a perturbation of the field which is propagating, namely the *incident* field. In the considered region of space, a new electromagnetic field occurs and such a *total* field it is nothing but a superposition of the original one and the perturbation caused by the obstacle (or scatterer). This latter is called *scattered* field and it is generated by the target that interacts with the incident field during its propagation. As a matter of fact, from a physical point of view, the inhomogeneity (penetrable or metallic, magnetic or not) becomes a "source" for the scattered field.

The electromagnetic scattering can be faced by considering two types of problem, the *forward scattering problem* and the *inverse scattering problem* [4]. The former deals with the evaluation of the scattered field given the electromagnetic properties of the obstacle (and supposing obviously that the incident field is known). The latter copes with retrieving information on the scatterer by handling the measurements of the total (or scattered) field.

The direct and the inverse scattering problem are linked each other by a sort of *duality*. In fact, from a physical point of view, the *cause* of the phenomenon is the interaction between the incident field and the obstacles, while the corresponding *effect* is the scattered field which originates in the space. Notably, the role of the two problems can be inverted and the formulation of one implies the formulation of the other.

In the literature, the direct problem is the most investigated and a lot of work has been done in developing more and more efficient numerical methods and computational techniques. Conversely, the inverse scattering problem has deserved less attention, probably because of its much increased difficulty. In fact, it is very challenging because of two different reasons, i.e., ill-posedness (according to the Hadamard's definition [5]) and non-linearity. Obviously, a strong effort has been done by research

groups in developing effective solution strategies which counteract both ill-posedness and non-linearity in order to solve the inverse problem at best.

Finding solution methods that allow to accurately solve the problem is an important task in a lot of application fields, thanks to the capability of microwaves of investigating non-accessible scenarios in a non-invasive way. Among all possible applications involving in inverse scattering problems, it is worth to mention some of the most relevant area, which are:

- subsurface prospection including ground penetrating radar (GPR) and humanitarian demining [6–9];
- non-destructive evaluation, as for example the search of small cracks inside structures [10, 11];
- military and civil security surveillance, such as *through-the-wall* and *intra-the-wall* imaging [12, 13];
- medical imaging for tumor anomalies detection [14, 15].

In a classical inverse scattering experiment, a given region of the space is assumed to be illuminated by a set of incident fields radiated by some antennas located in the close-proximity or in the far field of the interested area. The interaction of the incident fields with the target in the region gives rise to a scattered field which is measured by a set of receiving antennas. These measured fields become the data of the inverse scattering problem and, by a proper processing of such data, the solution of the problem is obtained. In particular, depending on the problem at hand, one may attain information about position, dimension, shape, number of scatterers and so on. Anyway, the most general problem consists in the retrieval of both the geometrical and electromagnetic properties of the scenario at hand. Generally speaking, the more refined and detailed information about the scenario are required, the more difficult the solution of the inverse problem at hand.

For the reasons above, in the last three decades several models and approaches have been proposed to provide accurate *qualitative* (geometrical features) or *quantitative* (geometrical and electromagnetic features) solutions. However, several difficulties come into play which challenge the inverse scattering community towards the development of more and more convenient solution approaches.

First of all, the ill-posedness of the problem entails that only a finite number of parameters can be extracted from the scattered field data, as these latter have a finite essential dimension due to their band-limitedness property with respect to both incidence and observation variables [16–18].

Second, a crucial difficulty comes from the non-linearity of the problem. In fact, the non linear relationship among the physical parameters and the scattered fields represents a severe obstacle to the achievement of reliable solutions, as the so called "false solutions" [19] (i.e. retrieved profiles completely different from the actual one) may occur.

The mathematical formulation of the inverse scattering problem as well as a deeper insight into the ill-posedness and non linearity are given in the Sections which follow.

1.2 The inverse scattering problem: basic equations

By the sake of simplicity (most results of the thesis can be easily extended), let us consider the canonical bi-dimensional (2D) scalar scattering problem in a free space homogeneous background. Also, let us suppose to deal with non-magnetic dielectric scatterers whose cross-sections Σ are embedded in a region $\Omega \subseteq \mathcal{R}^2$. The electromagnetic properties of the scatterer, at the angular frequency $\omega = 2\pi f$, are described by the contrast function:

$$\chi(\boldsymbol{r}) = \frac{\tilde{\varepsilon}_r(\boldsymbol{r})}{\tilde{\varepsilon}_b} - 1 = \frac{\varepsilon_r(\boldsymbol{r}) - j\sigma_r(\boldsymbol{r})/(\omega\varepsilon_0)}{\varepsilon_b - j\sigma_b/(\omega\varepsilon_0)} - 1 \tag{1.1}$$

where $\boldsymbol{r} = (x, y) \in \Omega$, ε_0 is the permittivity of the free space, while ε_r, σ_r, ε_b, σ_b are the relative permittivity and the electrical conductivity of the scatterer (subscript r) and the homogeneous background medium (subscript b), respectively.

Let suppose that an electric field, oriented along the z-axis, is radiated by a set of antennas located on a circumference Γ and impinges on Ω from a given incident direction $\boldsymbol{r}_t = (r_r, \theta_t) \in \Gamma$. By assuming and omitting, for the sake of brevity, the time harmonic factor $\exp(j\omega t)$, the equations ruling the inverse scattering problem, for the 2D TM scalar problem at hand, read [1–3]:

$$\begin{aligned} E(\boldsymbol{r}, \boldsymbol{r}_t) &= E_i(\boldsymbol{r}, \boldsymbol{r}_t) + k_b^2 \int_\Omega g(\boldsymbol{r}, \boldsymbol{r}')\chi(\boldsymbol{r}')E(\boldsymbol{r}', \boldsymbol{r}_t)d\boldsymbol{r}' \\ &= E_i(\boldsymbol{r}, \boldsymbol{r}_t) + \mathcal{A}_i[\chi(\boldsymbol{r})E(\boldsymbol{r}, \boldsymbol{r}_t)], \qquad \boldsymbol{r} \in \Omega, \boldsymbol{r}_t \in \Gamma \end{aligned} \tag{1.2}$$

$$\begin{aligned} E_s(\boldsymbol{r}_o, \boldsymbol{r}_t) &= k_b^2 \int_\Omega g(\boldsymbol{r}_o, \boldsymbol{r}')\chi(\boldsymbol{r}')E(\boldsymbol{r}', \boldsymbol{r}_t)d\boldsymbol{r}' \\ &= \mathcal{A}_e[\chi(\boldsymbol{r})E(\boldsymbol{r}, \boldsymbol{r}_t)], \qquad \boldsymbol{r} \in \Omega, \boldsymbol{r}_o, \boldsymbol{r}_t \in \Gamma \end{aligned} \tag{1.3}$$

where E_i, E_s and E are the incident, scattered and total field, respectively, $\boldsymbol{r}_o = (r_o, \theta_o) \in \Gamma$ denotes the observation position, while $\mathcal{A}_e$ and $\mathcal{A}_i$ are a short notation for the integral radiation operators, in which $g(\boldsymbol{r}, \boldsymbol{r}') = -j/4H_0^{(2)}(k_b\,|\boldsymbol{r} - \boldsymbol{r}'|)$ is the

Green's function of the background medium, $H_0^{(2)}$ being the Hankel function of zero-th order and second kind.

We refer to eq.(1.2) as *state* equation or, equivalently, *electric field integral equation (EFIE)*, and to eq.(1.3) as *data* equation. In particular, the first one describes the total electric field inside the domain Ω, while the second one represents the scattered electric field in the region outside the investigation domain.

The aim of an inverse scattering problem is to retrieve the contrast function $\chi(\boldsymbol{r})$ from the knowledge of the scattered field $E_s(\boldsymbol{r}_o, \boldsymbol{r}_t)$, which represents the data of the problem, and the incident field E_i. As already mentioned, the problem is both non linear and ill-posed. In fact, one can immediately observe that the total field inside the domain, which is obviously unknown as well, depends from the contrast function. In particular, in terms of the couple $(\chi(\boldsymbol{r}), E(\boldsymbol{r}), \boldsymbol{r} \in \Omega)$, the inverse scattering problem is a *bi-linear* problem, i.e., the unknowns appear as a product between them: if we fix one of the two unknowns, the problem would become linear in the other one. The ill-posedness is instead related to the compactness of the radiation operator $\mathcal{A}_e$ [4]. More details on ill-posedness and non linearity properties, as well as on the corresponding impact on the problem solution, are given in the subsections which follow.

As a possible alternative, one can consider the currents induced inside the object as auxiliary unknowns instead of the total field. By defining the contrast source as $W(\boldsymbol{r}) = \chi(\boldsymbol{r})E(\boldsymbol{r})$, the *source type integral equation (STIE)* formulation reads:

$$\begin{aligned} W(\boldsymbol{r}, \boldsymbol{r}_t) &= \chi(\boldsymbol{r})E_i(\boldsymbol{r}, \boldsymbol{r}_t) + k_b^2 \chi(\boldsymbol{r}) \int_\Omega g(\boldsymbol{r}, \boldsymbol{r}')W(\boldsymbol{r}', \boldsymbol{r}_t)d\boldsymbol{r}' \\ &= \chi(\boldsymbol{r})E_i(\boldsymbol{r}, \boldsymbol{r}_t) + \chi(\boldsymbol{r})\mathcal{A}_i[W(\boldsymbol{r}, \boldsymbol{r}_t)], \qquad \boldsymbol{r} \in \Omega, \boldsymbol{r}_t \in \Gamma \end{aligned} \tag{1.4}$$

while the data equation is turned into:

$$E_s(\boldsymbol{r}_o, \boldsymbol{r}_t) = k_b^2 \int_\Omega g(\boldsymbol{r}_o, \boldsymbol{r}')W(\boldsymbol{r}', \boldsymbol{r}_t)d\boldsymbol{r}' = \mathcal{A}_e[W(\boldsymbol{r}, \boldsymbol{r}_t)], \quad \boldsymbol{r} \in \Omega, \boldsymbol{r}_o, \boldsymbol{r}_t \in \Gamma \tag{1.5}$$

where the new unknowns are the contrast function $\chi(\boldsymbol{r})$ and the contrast source $W(\boldsymbol{r})$. Notably, the new data equation is now linear in the unknown $W(\boldsymbol{r})$ [20,21]. At a first glance, it would seem that one can solve it, and then substitute the achieved value for $W(\boldsymbol{r})$ in the state equation and solve it for $\chi(\boldsymbol{r})$. Unfortunately, this is not the case, as one cannot safely invert eq.(1.5) since it is a severely ill-posed problem.

1.2.1 Ill-posedness

A problem is defined ill-posed if it is not well-posed in the Hadamard's sense [5]. In particular, a problem is *well-posed* if its solution (i) exists, (ii) is unique and

(*iii*) continuously depends on data. Otherwise, in the lack of one or more of these requirements, the problem is ill-posed.

Since for the inverse scattering problem at hand (involving non magnetic isotropic scatterers) the uniqueness of the solution is proved [22, 23] and it always exists, let us focus on the third requirement, which is herein missing. Such a circumstance leads to a 'physical meaningless' solution, since in presence of measurement uncertainties it may happen that to small variations occurring on data, do not correspond small variations in the solution which will be completely corrupted by noise.

From a mathematical point of view, in case of single-view experiment (i.e., a single illuminating incident field is used) the ill-posedness is due to the "compactness" of the scattering operator $\mathcal{A}_e$ [4] which relates the unknown target's properties to scattered fields. As a matter of fact, the inverse of a compact operator cannot be continuous, so that the continuity requirement from the Hadamard's definition is violated. In particular, the generic unknown contrast belonging to an infinite dimensional space cannot be retrieved from the finite dimensional space of the collected information. In fact, whatever the kind of the scattering experiment, only a finite number of independent information can be reached, the so-called *Degrees of Freedom* (DoF) of the field [17,18]. Unfortunately, also in case of multi-view experiments (more illuminating incident waves are used) the problem remains ill-posed. This is due to the fact that also the incident fields belong to a compact set and, by paralleling the arguments for the single-view case, the scattering operator is still compact. Therefore, the number of independent equations is limited and a finite number of scattering experiments can be actually considered [18].

Note this latter circumstance (which is indeed undesired in recovery problems) is instead of interest in design problems, as one only needs to check (to enforce) a finite number of equations.

1.2.2 Non-linearity

The solution of the inverse scattering problem is usually pursued, in a least square sense, by minimizing a proper cost functional which takes into account both the data and the state equations. Due to the non-linearity of the underlying problem, this cost functional is a non-quadratic one, so that it may have many local minima which are "false solutions" of the problem [19]. In this kind of problem, a key role is played by the starting point of the minimization procedure, since if it does not belong to the attraction basin of the actual solution, a local minimum is reached and a solution far from the ground truth is obtained.

To get a better insight into the non-linearity, a physical interpretation of the issue could be sketched. When an incident wave interacts with objects in the space, a mutual scattering phenomenon occurs, i.e., higher order mutual interactions must be considered in the relationship between the scattered field and the objects.
By formally inverting the state equation (1.2) for the unknown E and substituting the result in eq.(1.3), the following expression is obtained:

$$E_s = \mathcal{A}_e[\chi(\mathcal{I} - \mathcal{A}_i\chi)^{-1}E_i] \tag{1.6}$$

By exploiting the Neumann series for the term in round brackets, for $\|\mathcal{A}_i\chi\| < 1$, the final expression for the scattered field reads:

$$E_s = \mathcal{A}_e\chi[\mathcal{I}E_i + \mathcal{A}_i\chi E_i + \mathcal{A}_i\chi\mathcal{A}_i\chi E_i + \cdots] \tag{1.7}$$

where each addendum in brackets represents how gradually the mutual interactions increase, thus increasing the non linearity of the problem.

1.3 Rationale and contents of the thesis

The inverse scattering problem involves reconstruction of the property of a scatterer from the knowledge of its scattering data. During the years, the challenging nature of the problem has brought the inverse scattering community to develop more and more solution strategies for imaging problems. Needless to say, diagnosis methodologies deserved interest especially in fields in which the human's health and safety is of interest, like biomedical imaging for cancer detection and brain-stroke monitoring, investigation of the reinforcement and condition of roads, bridges, and airport runways, the identification of structural integrity of buildings, demining, and so on.

On the contrary, in this thesis the inverse scattering problem is considered from the point of view of *design* problems. Saying it in other words, starting from a specification of a field pattern which takes the place of the scattering data, the corresponding scatterer (and eventually the amplitude of the primary sources, see the following) are synthesized. Note that such a change of the point of view allows to keep unaltered the problem's formulation and hence the more general applicability of the theory.

Obviously, the intrinsic difficulties of the inverse scattering problem keep unchanged as well. However, since the imaging of an object is no longer of interest, the non-linearity issue is not a crucial point. In fact, whatever synthesized contrast function able to satisfy the (imposed) data of the problem is an admissible solution. This notwithstanding, a priori information as well as similar arguments of the usual

diagnosis problem can be exploited in order to proper conditioning the (still) ill-posed problem at hand and find the optimal solution.

The remainder of this thesis is composed by four chapters (including Conclusions) and five appendices (where mathematical details are deepened), and it is structured as follows.

In Chapter 2, after a brief summary of existing results, new theoretical and methodological contributions are presented for the inverse scattering problem.
Coming to details, first (in the same spirit of the Born approximation) a Fourier based spectral analysis is derived for effective approximated solution strategies like the *Extended Born*, the *Contrast Source Extended Born* and the *Strong Permittivity Fluctuation* approximations. Beside their interest on the kind of profiles which can be actually retrieved or synthesized, the results also open the way to an accurate and reliable application of the recently introduced Compressive Sensing (CS) techniques (whose hypothesis do hold true).
Among the approximation-based solution strategies, the 'virtual experiments' (VE) framework has been recently introduced in literature as an effective approach for imaging non weak objects. Starting from its basic formulation, in the Chapter is presented an extension of the VE to the case of inhomogeneous scenarios and hence the so-called *distorted virtual experiments* (DVE) approximation. Interestingly, VE and DVE can be jointly exploited into an iterative scheme to further enlarge the range of validity of the approximation itself. To this aim, the *distorted iterated virtual experiments* (DIVE) strategy is also derived and discussed. Beside the methodologies handling the non linearity property of the inverse scattering problem, an effective regularization procedure based on CS is also proposed. In fact, CS has been developed, in the last years, as an effective tool for the solution of linear problems by exploiting a reduced number of data with respect to the unknowns; to this aim, this latter must be 'sparse' (i.e., with few elements different from zero) in a proper representation basis. Starting from this concept, the CS-based regularization is exploited for the solution of the approximated inverse scattering problem for both the DVE and DIVE strategies, thus allowing to reach more and more accurate solutions with respect to common regularization approaches in case of both numerical and experimental data.
Finally, by exploiting the well-known Devaney and Wolf' theorems [24], a novel representation for the non-radiating currents is derived and assessed. Such a result is of interest both in the synthesis of invisibility devices as well as in antenna synthesis. In fact, the addition of a "non radiating" source to a given already synthesized source may simplify actual realization of the antenna.

In Chapter 3, the formulation of the inverse scattering problem as a design problem is introduced. In this thesis, the problem is tackled in its full non linearity and the well-known *Contrast Source Inversion* (CSI) method is adopted. However, a proper reformulation of the CSI is proposed by considering the amplitudes of the incident fields as further unknowns, in order to deal with an accurate matching of the field specifications through possibly simpler devices. In this Chapter, the synthesis of dielectric profile antennas is pursued. Firstly, the synthesis of canonical lenses is attained as an assessment of the strategy. Then, antennas generating generic given patterns are looked for.

Although the reached devices show good performances and hence represent an innovative solution *by per se*, a further step toward actual manufacturing can be pursued by looking at *artificial materials* (AMs) based devices. As a first possibility, the synthesized gradient index (GRIN) dielectric profiles by means of the modified CSI is turned into a *graded artificial materials* (GAMs) device by exploiting homogenization theories. The second and more original strategy concerns instead to directly synthesize a GAMs by using a proper representation basis for the unknown contrast function into the CSI functional.

Chapter 4 is then devoted to the synthesis of cloaks for invisibility scopes. In this thesis, volumetric cloaks are considered and the CSI method as well as several regularization techniques, already exploited for diagnosis problem, are herein adopted for the synthesis of cloaks with different characteristics. Among them, physical feasibility properties are the most interesting since they allow to deal with 'natural' material, thus avoiding metamaterials, which are the common solution for this kind of problem. Moreover, the exploitation of the AMs-based solution introduced in Chapter 3 is also performed which make the GAMs cloaks the most effective solution. Finally, the spectral analysis introduced in Chapter 2 is herein turned into a possible way to design undetectable objects.

Conclusions and recommendations for further developments are finally drawn in Chapter 5.

2

THEORETICAL AND METHODOLOGICAL ADVANCES IN INVERSE SCATTERING

2.1 Some existing solution strategies

In this Chapter, some tools for inverse scattering facilities are first reviewed in order to have a better insight of their possible usefulness in design problems. In this spirit, some canonical strategies are briefly recalled, by taking care on the basic linear approximations as well as on their advanced variations which allow to extend the range of validity and taking into account some a priori information of the unknowns of the problem. Along the same line, the recent paradigm of Compressive Sensing is briefly recalled and commented. Then, a spectral analysis of different useful approximations is introduced. As a second original contribution, two new solution strategies are proposed, both based on the new framework of 'virtual experiments', the *distorted virtual experiments* (DVE) and the *distorted iterated virtual experiments* (DIVE) approximations. Last, but not least, a new approach for the representation of non-radiating currents is proposed.

As already stressed, two not trivial issues make the inverse scattering phenomenon a complex problem, namely the ill-posedness and the non-linearity. In the following subsections, the main regularization techniques as well as strategies to counteract the non-linearity are briefly reviewed.

2.1.1 Regularization techniques

It was explained that the DoF of the scattered field constitute an upper bound for the significant data of the problem, for each scattering experiment [17, 18]. Therefore, a first possibility to increase such an amount of data is to perform additional scattering experiments. Several possibilities can be outlined: spatial diversity, frequency diversity or a combination of them. More in details, the spatial diversity aims at performing a number of experiments moving the illumination direction all around the investigation space, in such a way that the collected data include the system's response from

different points of view. Recently, new methods have been proposed in order to increase diversity [25, 26]. However, the above mentioned solutions cannot restore the well-posedness of the inverse scattering problem, since the number of independent information remains limited [18].

In order to restore the well-posedness of the problem, a huge amount of regularization techniques have been developed. The principle of the regularization methods is to use additional a priori information on the unknown in an explicit way in order to restore a unique solution compatible with the data.

As a first possibility, an energetic constraint can be added to the least square solution in order to keep minimum the energy of the solution; for instance, the Tikhonov regularization method [4, 27] aims to retrieve a minimum ℓ_2-norm energy.

However, some specific a priori information on the actual unknown (i.e., the contrast function) can be exploited and/or enforced. Just to mention a few:

i. enforcing a piecewise constant behavior on the contrast function [28–31];
ii. inducing physics bounds on the values of the unknown permittivity and conductivity functions;
iii. imposing a given finite alphabet of values for the permittivity function [32];
iv. imposing an upper bound on the dimensionality of the space where the unknown function is looked for ('regularization by projection') [33–40].

The above listed techniques act on the contrast function χ; however, similar concepts have been exploited on the auxiliary unknown $W(\boldsymbol{r})$ [41].

Recently, the new paradigm of Compressive Sensing (CS) [42, 43] has been introduced in literature for linear problems. The key idea is that an ill-conditioned problem can be solved even if the number of data is lower than the number of unknowns, since the 'sparsity' or 'compressibility' of the unknown can act as regularizer of the problem. Essentials of the CS theory will be recalled with some detail in Section 2.2.

2.1.2 Methods to tackle the non-linearity

The adoption of linearizing approaches seems to be attractive to counteract the non-linearity of the inverse scattering problem, since the problem itself is simplified and different regularization techniques can be applied in a straightforward fashion. A lot of approximations have been proposed in literature during the years. Obviously, each approximation concerns a specific rationale and a situation of interest, that means they look for a particular class of objects by exploiting proper a priori information. On the other hand, they suffer from several limitations induced by the range of validity

of the introduced approximation.

The main linear approximations are listed below.

- The *Born* approximation (BA) [44] is valid for 'weak scatterers', i.e., when the internal characteristics of the scatterers are very close to those of the external medium and its dimension is very small as compared to the incoming wavelength. From a practical point of view, this assumption leads to substitute the unknown total field inside the operator's kernel with the incident field, thus completely neglecting the presence of the object. Notably, by referring to eq.(1.7), the BA means to consider only the first term of the series, thus neglecting higher order mutual interactions. If the linearization is performed around a nominal scenario different from a homogeneous background, the underlying approximation is referred to as *distorted Born* approximation (DBA) [45].
- The *Rytov* approximation (RA) [46] holds for scatterers whose contrast function is smooth and low with respect to the background medium; moreover, no limits in the object's dimension are considered since the total field is only approximated in its phase.
- The *Kirchhoff* or *Physical optics* approximation (PO) [46] is suitable for electrically large and strong scatterers; conversely with respect to the other methods, PO refers to the auxiliary unknown contrast source $W(\boldsymbol{r})$, thus dealing with a kind of inverse source problem.
- The *Strong permittivity fluctuation* approximation (SPF) [47, 48] is instead valid for a set of different small scatterers and the problem is linearized and solved by means of an auxiliary unknown.

As an improvement with respect to the linearized methods, the *quadratic* approach [49, 50] is also worth being mentioned. In this latter, a weak degree of non-linearity is introduced by adopting a second order approximation for the unknown-data mapping operator. As a consequence, the range of validity is wider compared to the BA, but also in this case the solution could be meaningfulness if the target's parameters exceed the validity of the approximation.

Interestingly, by looking at different classes of scatterers, the BA has given rise to a number of different approximations. For instance, when non-weak scatterers are considered, the BA can be incorporated inside an iterative scheme. The arising solution approaches are the so-called *Born iterative method* (BIM) [51] and *distorted Born iterative method* (DBIM) [52]. At each iteration, the inverse problem is solved by applying the BA while the direct problem by updating the internal field (and the Green's function in DBIM). Obviously, both approaches outperform the standard BA

but the final outcome and performances depend on the starting guess as well as on the range of validity of the intermediate linearizations. Other solution methods deriving from BA are the *Extended Born approximation* (EBA) [53–56] and the *Contrast Source Extended Born approximation* (CS-EBA) [35, 57], which are viable in case of lossy host medium; in fact, by relying on the picked behavior of the Green's function and the reduced intensity of mutual interactions in such a case, the inverse scattering basic equations can be simplified and the arising linear problem is solved for an auxiliary unknown.
A more detailed explanation of some of the above approximations which includes a rigorous mathematical formulation is given in Section 2.3.

In order to overcome the limits due to the range of validity of each approximation, iterative optimization procedures which tackle the inverse problem in its full nonlinearity have been proposed in literature. In this case, global optimization schemes should be adopted in order to avoid 'false solutions' [19], but they are not viable in case of large number of unknowns due to the exponential growth of the computational complexity. On the other hand, local iterative optimizations seem to be good candidates. Among these, the modified gradient method [34, 58, 59], the *Contrast Source Inversion* (CSI) method [20], the *Contrast Source Extended Born* model [21, 35] and the *Subspace Optimization Method* (SOM) [60] deserve to be mentioned.
It is worth to note that several strategies could be adopted in order to reduce the occurrence of 'false solutions'. In particular, a good initial guess (e.g., reached by a pre-processing step) and/or some a priori information could constrain the minimization procedure in such a way that the searching space is reduced.

2.2 The Compressive Sensing (CS) paradigm

In the last years, the Compressive Sensing (CS) framework has emerged as an effective way to find meaningful solutions to undetermined systems describing linear models. As demonstrated by several contributions [61–63], the field of CS evolves from four decades. However, the idea of CS got a new life in 2004 when David Donoho, Emmanuel Candes, Justin Romberg, and Terence Tao gave important results regarding the mathematical foundation of CS [42, 64, 65].

The CS theory asserts that one can recover signals and images from far fewer samples or measurements than is possible using traditional methods, like for instance the Nyquist theory [65]. As it can be easily guessed, such a remarkable result is useful in very many scenarios in which limited number of samples can be actually collected [66].

As a matter of fact, part of the success of the CS paradigm (as witnessed by the very large number of papers being published on the subject) comes from statements such as 'the possibility of overcoming the Nyquist criterion' or to achieve 'super-resolution' in a number of recovery (and imaging) problems [65]. To make this possible, CS relies on two principles: *sparsity*, which pertains to the signals of interest, and *incoherence*, which pertains to the sensing modality. A signal is said *sparse* in a given representation basis, if it can be exactly represented by means of few non-zero elements; more precisely, the idea is that the 'information rate' of a continuous time signal may be much smaller than suggested by its bandwidth, or that a discrete-time signal depends on a number of DoF which is comparably much smaller than its (finite) length. As far as the *incoherence* property concerns, it is a concept related to the measurement process [65].

Provided the proper expansion is used in order to guarantee a sparse or compressible representation of the unknown function, CS theory guarantees that an accurate retrieval of the unknown is possible even for a number of data much lower than the overall number of basis coefficient, but sufficiently larger than the number of non-zero elements [65].

The above described peculiar features of CS has led to investigate such a recovery algorithm for inverse scattering problems, in particular for biomedical monitoring and non-invasive inspections [13, 67–74]. However, the adoption of the CS theory is not straightforward and the reason is twofold: first, the choice of a convenient representation basis for the specific problem at hand is not a trivial task; second, the intrinsic non-linear nature of the electromagnetic inverse scattering problem does not fulfill the theoretical results well developed and assessed for linear models.

For the reasons above, CS was firstly adopted for imaging of 'point-like' scatterers in conjunction with linear approximations such as the BA [69,75] or the DBIM [72,76]; later, the recovery of extended target has been exploited by considering the RA and the total variation (TV) approach [28]. Note that the CS tool allows to perform a 'super resolution' diagnosis by acting as a regularizer of the problem, but the validity of the mentioned approximations keeps still limited.
Recently, an effective imaging approach which exploits CS facilities for the solution of the inverse scattering problem in its full non-linearity has been proposed [77].

Interesting applicative and theoretical results have been also obtained in the field of antenna arrays diagnosis, both for linear [78–80] and non linear [81] models. In particular, for this latter case stimulating arguments about the *incoherence* property have been derived [81].

In this thesis, the CS paradigm will be exploited as a facilitator for design purposes. In fact, supposing a *sparse* unknown for the problem means that such a function is made by few elements different from zero. Correspondingly, the arising solution of the inverse scattering problem will be a more easily realizable device.
Applications of the CS paradigm in inverse scattering for design will be shown in the following Chapters, while for some simple understanding (and basics) the reader is deferred to Appendix A.

2.3 A spectral interpretation of approximated solution strategies.

In this Section, an insight into the implication of the approximated approaches for the solution of the inverse scattering problem introduced in Sect.2.1 is given. In particular, by paralleling the results of the well-known BA [82], a Fourier analysis is proposed for the EBA, the CS-EBA and the SPF approximation (SPFA), which allows to gather a spectral interpretation of the strategy at hand.

Since the formulation for the EBA and CS-EBA is actually the same, a unique spectral analysis derivation will be tackled in the following.

2.3.1 The extended Born model

As is well known, the inverse scattering problem within the BA is viable and accurate when weak scatterers are looking for. As a matter of fact, the total field inside the investigation domain is approximated with the background electric field, thus neglecting the effects that the scatterer induces into the field itself.

An improvement over the BA is achieved in the extended Born model [53], which results from an approximation arising from the peaked behavior of the Green's function in case of lossy background. Notably, in the same way as for the Born model, an extended Born series can be derived.
In this respect, let consider the *STIE* formulation for the state equation [21, 35]:

$$W(\boldsymbol{r}, \boldsymbol{r}_t) = \chi(\boldsymbol{r}) E_i(\boldsymbol{r}, \boldsymbol{r}_t) + \chi(\boldsymbol{r}) \int_\Omega g(\boldsymbol{r} - \boldsymbol{r}') W(\boldsymbol{r}', \boldsymbol{r}_t) d\boldsymbol{r}' \tag{2.1}$$

so that in the following it will refer to the *contrast source extended Born* (CS-EB) model.
By adding and subtracting $W(\boldsymbol{r}, \boldsymbol{r}_t)$ into the integral operator, the new state equation becomes:

$$
\begin{aligned}
W(\boldsymbol{r},\boldsymbol{r}_t) &= \chi(\boldsymbol{r})E_i(\boldsymbol{r},\boldsymbol{r}_t) \\
&+ \chi(\boldsymbol{r})W(\boldsymbol{r},\boldsymbol{r}_t)\int_\Omega g(\boldsymbol{r}-\boldsymbol{r}')d\boldsymbol{r}' + \chi(\boldsymbol{r})\int_\Omega g(\boldsymbol{r}-\boldsymbol{r}')\left[W(\boldsymbol{r}',\boldsymbol{r}_t)-W(\boldsymbol{r},\boldsymbol{r}_t)\right]d\boldsymbol{r}' \\
&= \chi(\boldsymbol{r})E_i(\boldsymbol{r},\boldsymbol{r}_t) + \chi(\boldsymbol{r})W(\boldsymbol{r},\boldsymbol{r}_t)f_\Omega(\boldsymbol{r}) + \chi(\boldsymbol{r})\mathcal{A}_{iMOD}\left[W(\boldsymbol{r},\boldsymbol{r}_t)\right] \quad (2.2)
\end{aligned}
$$

where:

$$
f_\Omega(\boldsymbol{r}) = \int_\Omega g(\boldsymbol{r}-\boldsymbol{r}')d\boldsymbol{r}'
$$

$$
\mathcal{A}_{iMOD}\left[W(\boldsymbol{r},\boldsymbol{r}_t)\right] = \int_\Omega g(\boldsymbol{r}-\boldsymbol{r}')\left[W(\boldsymbol{r}',\boldsymbol{r}_t)-W(\boldsymbol{r},\boldsymbol{r}_t)\right]d\boldsymbol{r}'
$$

By formally inverting twice eq.(2.2), one initially achieves:

$$
W(\boldsymbol{r},\boldsymbol{r}_t) = p(\boldsymbol{r})E_i(\boldsymbol{r},\boldsymbol{r}_t) + p(\boldsymbol{r})\mathcal{A}_{iMOD}\left[W(\boldsymbol{r},\boldsymbol{r}_t)\right] \quad (2.3)
$$

in which:

$$
p(\boldsymbol{r}) = \frac{\chi(\boldsymbol{r})}{\mathcal{I}-\chi(\boldsymbol{r})f_\Omega(\boldsymbol{r})}
$$

and then, by defining $\mathcal{I}$ the identity operator:

$$
W(\boldsymbol{r},\boldsymbol{r}_t) = \left(\mathcal{I}-p(\boldsymbol{r})\mathcal{A}_{iMOD}\right)^{-1}p(\boldsymbol{r})E_i(\boldsymbol{r},\boldsymbol{r}_t) \quad (2.4)
$$

If $\|p(\boldsymbol{r})\mathcal{A}_{iMOD}\| < 1$, $\|\cdot\|$ being the ℓ_2-norm, a series expansion for the inverse operator can be performed, thus obtaining the CS-EB series:

$$
W(\boldsymbol{r},\boldsymbol{r}_t) = \sum_{n=0}^{+\infty}\left(p(\boldsymbol{r})\mathcal{A}_{iMOD}\right)^n p(\boldsymbol{r})E_i(\boldsymbol{r},\boldsymbol{r}_t) \quad (2.5)
$$

Note that, as discussed is [21], the CS-EB series has been proved to be more rapidly converging that the Born series also in very many cases where the background is lossless.

From the singular nature of $g(\boldsymbol{r}-\boldsymbol{r}')$ when $\boldsymbol{r}'=\boldsymbol{r}$ one may expect that the dominant contribution to the integral in eq.(2.2) is given by points close to $\boldsymbol{r}'=\boldsymbol{r}$. Moreover, the integrand of the second integral in eq.(2.2) is now integrable since the quantity in the square brackets vanish as $\boldsymbol{r}'\to\boldsymbol{r}$ where g is singular. As a consequence, in the CS-EB approximation (CS-EBA) the second integral in eq.(2.2) is neglected since the first one plays a more significant role in deriving an approximation for the total field. Saying it in other words, the first term in the series (2.5) is the dominant one, so that the arising state equation for the CS-EBA reads:

$$
W(\boldsymbol{r},\boldsymbol{r}_t) = p(\boldsymbol{r})E_i(\boldsymbol{r},\boldsymbol{r}_t) \quad (2.6)
$$

Finally, when the new approximation (2.6) is considered into the data equation, a linear inverse scattering problem in the unknown $p(\boldsymbol{r})$ is achieved [21, 35]:

$$E_s(\boldsymbol{r}_o, \boldsymbol{r}_t) = \mathcal{A}_e \left[p(\boldsymbol{r}) E_i(\boldsymbol{r}, \boldsymbol{r}_t) \right] \tag{2.7}$$

Note that, if the EFIE is considered rather than the STIE and the term $\chi(\boldsymbol{r})E(\boldsymbol{r})$ is added and subtracted into the integral operator, the same approximated model (2.6)-(2.7) can be derived for the *extended Born approximation* (EBA) [54, 55].

By paralleling the results of the BA, interesting arguments can be inferred when plane waves incident fields and far field observations are considered. In fact, under these assumptions, the expression for the scattered field reads:

$$E_s(\boldsymbol{k}_t, \boldsymbol{k}_o) = C \int_\Omega p(\boldsymbol{r}') e^{-j(\boldsymbol{k}_t - \boldsymbol{k}_o)\cdot \boldsymbol{r}'} d\boldsymbol{r}' \tag{2.8}$$

in which $\boldsymbol{k}_t$ and $\boldsymbol{k}_o$ are the vector of incidence and observation direction, respectively, while C is a constant value arising from the asymptotic expansion of the radiation operator.

Interestingly, eq.(2.8) shows useful relationship with the Fourier transform $\mathscr{F}[\cdot]$ of the auxiliary function. In fact, when this latter is evaluated, the following expression is gathered:

$$\mathscr{F}\left[p(\boldsymbol{r})\right] = \widetilde{p}(\boldsymbol{\mathcal{K}}) = \int_\Omega p(\boldsymbol{r}') e^{-j\boldsymbol{\mathcal{K}}\cdot\boldsymbol{r}'} d\boldsymbol{r}' = \int_\Omega p(x,y) e^{-j(k_x x' + k_y y')} dx' dy' \tag{2.9}$$

The above equations (2.8)-(2.9) show that exists a relation between the scattered field and the spatial Fourier transform of the auxiliary variable $p(\boldsymbol{r})$ encoding the original contrast function $\chi(\boldsymbol{r})$; in particular, $E_s(\boldsymbol{k}_t, \boldsymbol{k}_o) = \widetilde{p}(\boldsymbol{k}_t - \boldsymbol{k}_o)$. In other words, E_s can be considered to be the restriction of the Fourier transform to the circle such that:

$$k_x = k_{tx} + k_{ox}$$

$$k_y = k_{ty} + k_{oy}$$

as long as $k_{tx}^2 + k_{ty}^2 = \omega^2 \varepsilon \mu$ and $k_{ox}^2 + k_{oy}^2 = \omega^2 \varepsilon \mu$, ε and μ being the permittivity and permeability of the homogeneous free space, respectively. Therefore, the spatial frequencies set $\boldsymbol{\mathcal{K}}$ maps, $\forall$ experiment $\boldsymbol{k}_t$, the surface of a sphere of radius $|\boldsymbol{k}_o|$ that is centered at the point $\boldsymbol{\mathcal{K}} = -\boldsymbol{k}_t$ in the $\boldsymbol{\mathcal{K}}$ space, see fig.2.1(a). This sphere is known as *Ewald sphere*.

By considering a number of experiments $|\boldsymbol{k}_t|$, the final scattered field would be given by $\widetilde{p}(\boldsymbol{\mathcal{K}})$ over the union of the surfaces of a number of Ewald spheres, namely over the bigger sphere with a radius of $2|\boldsymbol{k}_o|$ (the so-called Ewald limiting sphere), see fig.2.1(b).

2.3.2 Strong Permittivity Fluctuation model

The SPF approximation (SPFA) has been introduced by Tsang and Kong [47] by exploiting the singularity of the Green's function for the solution of the vectorial

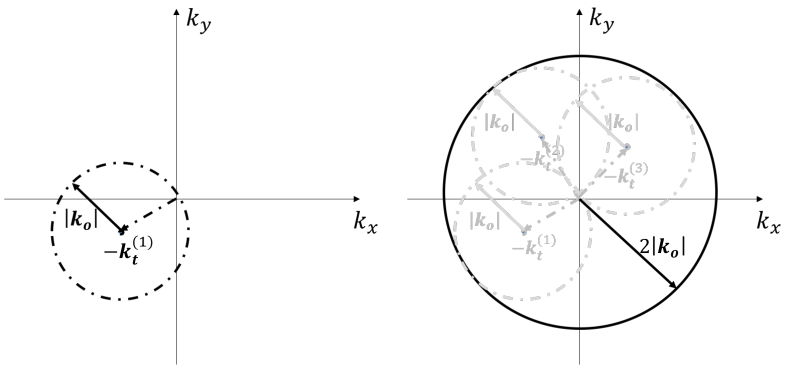

(a) (b)

Fig. 2.1. Spectral interpretation of the CS-EBA (and also EBA). (a) Spectral coverage for the t-th experiment: the Ewald sphere. (b) Spectral coverage for a set of experiments: the Ewald limiting sphere.

problem of wave scattering by random medium in case of both small and large variance of the permittivity function. As a matter of fact, until then such a singular nature of the dyadic Green's function was not taken into account thus applying and validating the random medium theory only in case of weak fluctuation.

Let us consider the state equation for the 2D vectorial case:

$$\begin{aligned}\boldsymbol{E}(\boldsymbol{r},\boldsymbol{r}_t) &= \boldsymbol{E}_i(\boldsymbol{r},\boldsymbol{r}_t) + \int_\Omega \overline{\overline{\boldsymbol{G}}}(\boldsymbol{r},\boldsymbol{r}')\Delta k^2 \cdot \boldsymbol{E}(\boldsymbol{r}',\boldsymbol{r}_t)d\boldsymbol{r}' \\ &= \boldsymbol{E}_i(\boldsymbol{r},\boldsymbol{r}_t) + \boldsymbol{A}_i\left[\Delta k^2 \cdot \boldsymbol{E}(\boldsymbol{r},\boldsymbol{r}_t)\right], \quad \boldsymbol{r}\in\Omega \end{aligned} \tag{2.10}$$

in which:

$$\overline{\overline{\boldsymbol{G}}}(\boldsymbol{r},\boldsymbol{r}') = \left(\overline{\overline{\boldsymbol{\mathcal{I}}}} - \frac{1}{k_b^2}\nabla\nabla\right) g(\boldsymbol{r},\boldsymbol{r}')$$

is the dyadic Green's function for homogeneous background medium, $\overline{\overline{\boldsymbol{\mathcal{I}}}}$ is the 2D identity operator, $g(\boldsymbol{r},\boldsymbol{r}')$ is the 2D scalar Green's function and $\Delta k^2 = k^2 - k_b^2$, k being the wavenumber of the random medium. The symbol $(\cdot)$ states for the inner product.

As it is known, the $g(\boldsymbol{r},\boldsymbol{r}')$ function becomes singular when the observation point is inside the source region and therefore the integral equation (2.10) results indeterminate. In order to overcome such a difficulty, by following the approach in [83], the singularity can be treated by means of the *principal volume method*, namely, by splitting the integration domain into a small volume Ω_δ surrounding the discontinuity and then let it approaches to zero, plus the remain $\Omega - \Omega_\delta$ part:

$$\begin{aligned}\boldsymbol{E}(\boldsymbol{r},\boldsymbol{r}_t) &= \boldsymbol{E}_i(\boldsymbol{r},\boldsymbol{r}_t) + \lim_{\Omega_\delta\to 0}\left[\int_{\Omega-\Omega_\delta}\overline{\overline{\boldsymbol{G}}}(\boldsymbol{r},\boldsymbol{r}')\Delta k^2\cdot\boldsymbol{E}(\boldsymbol{r}',\boldsymbol{r}_t)d\boldsymbol{r}'\right.\\ &\qquad\left.+\int_{\Omega_\delta}\overline{\overline{\boldsymbol{G}}}(\boldsymbol{r},\boldsymbol{r}')\Delta k^2\cdot\boldsymbol{E}(\boldsymbol{r}',\boldsymbol{r}_t)d\boldsymbol{r}'\right]\\ &= \boldsymbol{E}_i(\boldsymbol{r},\boldsymbol{r}_t) + \lim_{\Omega_\delta\to 0}\int_{\Omega-\Omega_\delta}\overline{\overline{\boldsymbol{G}}}(\boldsymbol{r},\boldsymbol{r}')\Delta k^2\cdot\boldsymbol{E}(\boldsymbol{r}',\boldsymbol{r}_t)d\boldsymbol{r}' - \frac{\overline{\overline{\boldsymbol{L}}}\cdot\Delta k^2\boldsymbol{E}(\boldsymbol{r},\boldsymbol{r}_t)}{k_b^2}\end{aligned} \tag{2.11}$$

where $\overline{\overline{\boldsymbol{L}}}$ is a dyad depending on the shape of Ω_δ. After simple manipulations, one achieves:

$$\left(\overline{\overline{\boldsymbol{\mathcal{I}}}} + \frac{\Delta k^2}{k_b^2}\overline{\overline{\boldsymbol{L}}}\right)\cdot\boldsymbol{E}(\boldsymbol{r},\boldsymbol{r}_t) = \boldsymbol{E}_i(\boldsymbol{r},\boldsymbol{r}_t) + P.V.\int_\Omega\overline{\overline{\boldsymbol{G}}}(\boldsymbol{r},\boldsymbol{r}')\Delta k^2\cdot\boldsymbol{E}(\boldsymbol{r}',\boldsymbol{r}_t)d\boldsymbol{r}' \tag{2.12}$$

where $P.V.\int_\Omega$ stands for a shape dependent principal value integral. In particular, if a cylinder is considered as volume Ω_δ, $\overline{\overline{\boldsymbol{L}}} = \frac{\overline{\overline{\boldsymbol{\mathcal{I}}}}}{2}$, while for a sphere $\overline{\overline{\boldsymbol{L}}} = \frac{\overline{\overline{\boldsymbol{\mathcal{I}}}}}{3}$ [83].
By defining [47, 48]:

$$\boldsymbol{F}(\boldsymbol{r},\boldsymbol{r}_t) = \left(\overline{\overline{\boldsymbol{\mathcal{I}}}} + \frac{\Delta k^2}{k_b^2}\overline{\overline{\boldsymbol{L}}}\right)\cdot\boldsymbol{E}(\boldsymbol{r},\boldsymbol{r}_t) = \left(\overline{\overline{\boldsymbol{\mathcal{I}}}} + \chi\overline{\overline{\boldsymbol{L}}}\right)\cdot\boldsymbol{E}(\boldsymbol{r},\boldsymbol{r}_t)$$

$$\overline{\overline{\boldsymbol{q}}}(\boldsymbol{r}) = \Delta k^2\left(\overline{\overline{\boldsymbol{\mathcal{I}}}} + \frac{\Delta k^2}{k_b^2}\overline{\overline{\boldsymbol{L}}}\right)^{-1} = \overline{\overline{\boldsymbol{\mathcal{I}}}}q(\boldsymbol{r})$$

$$q(\boldsymbol{r}) = \Delta k^2\left(1+\frac{\chi(\boldsymbol{r})}{2}\right)^{-1}$$

the following state equation for the SPF model is derived:

$$\begin{aligned}\boldsymbol{F}(\boldsymbol{r},\boldsymbol{r}_t) &= \boldsymbol{E}_i(\boldsymbol{r},\boldsymbol{r}_t) + P.V.\int_\Omega\overline{\overline{\boldsymbol{G}}}(\boldsymbol{r},\boldsymbol{r}')\overline{\overline{\boldsymbol{\mathcal{I}}}}q(\boldsymbol{r}')\cdot\boldsymbol{F}(\boldsymbol{r}',\boldsymbol{r}_t)d\boldsymbol{r}'\\ &= \boldsymbol{E}_i(\boldsymbol{r},\boldsymbol{r}_t) + \boldsymbol{A}_{iSPF}\left[\overline{\overline{\boldsymbol{\mathcal{I}}}}q(\boldsymbol{r})\cdot\boldsymbol{F}(\boldsymbol{r},\boldsymbol{r}_t)\right]\end{aligned} \tag{2.13}$$

As already done in Section 2.3.1, it is possible to formally invert (2.13):

$$\boldsymbol{F}(\boldsymbol{r},\boldsymbol{r}_t) = \left(\overline{\overline{\boldsymbol{\mathcal{I}}}} - \boldsymbol{A}_{iSPF}\left[\overline{\overline{\boldsymbol{\mathcal{I}}}}q(\boldsymbol{r})\right]\right)^{-1}\cdot\boldsymbol{E}_i(\boldsymbol{r},\boldsymbol{r}_t) \tag{2.14}$$

and define a series in case of $\left\|\boldsymbol{A}_{iSPF}\left[\overline{\overline{\boldsymbol{\mathcal{I}}}}q(\boldsymbol{r})\right]\right\| < 1$, which reads:

$$\boldsymbol{F}(\boldsymbol{r},\boldsymbol{r}_t) = \sum_{n=0}^{+\infty}\left(\boldsymbol{A}_{iSPF}\left[\overline{\overline{\boldsymbol{\mathcal{I}}}}q(\boldsymbol{r})\right]\right)^n\cdot\boldsymbol{E}_i(\boldsymbol{r},\boldsymbol{r}_t) \tag{2.15}$$

Finally, for $\left\|\boldsymbol{A}_{iSPF}\left[\overline{\overline{\boldsymbol{\mathcal{I}}}}q(\boldsymbol{r})\right]\right\| \ll 1$ which surely holds true in case of the overall scattering system is constituted by many different (unconnected) small scatterers, the SPF approximation (SPFA) is obtained by considering only the first term of the summation (2.15):

$$\boldsymbol{F}(\boldsymbol{r},\boldsymbol{r}_t) = \boldsymbol{E}_i(\boldsymbol{r},\boldsymbol{r}_t) \tag{2.16}$$

and by substituting the expression (2.16) into the data equation:

$$\boldsymbol{E}_s(\boldsymbol{r}_o, \boldsymbol{r}_t) = \boldsymbol{A}_e \left[\overline{\overline{\boldsymbol{\mathcal{I}}}} q(\boldsymbol{r}) \cdot \boldsymbol{F}(\boldsymbol{r}, \boldsymbol{r}_t) \right] = \boldsymbol{A}_e \left[\overline{\overline{\boldsymbol{\mathcal{I}}}} q(\boldsymbol{r}) \cdot \boldsymbol{E}_i(\boldsymbol{r}, \boldsymbol{r}_t) \right] \tag{2.17}$$

it becomes linear in the unknown $q(\boldsymbol{r})$.

By exploiting the same arguments as in Section 2.3.1, a relationship in the spectral domain between the scattered fields and the auxiliary variable of the linearized model can be found also for the SPFA. In this respect, by referring to incident plane waves and by considering far field measurements, one reaches that $E_s(\boldsymbol{k}_t, \boldsymbol{k}_o) = \widetilde{q}(\boldsymbol{k}_t - \boldsymbol{k}_o)$, $\boldsymbol{k}_t$ and $\boldsymbol{k}_o$ being the vector of incidence and observation direction, respectively, and $\widetilde{q}(\boldsymbol{\mathcal{K}}) = \mathscr{F}[q(\boldsymbol{r})]$.

In fig.2.2, a pictorial representation of the outcome of the Fourier-based analysis which holds for the above described approximations is reported.

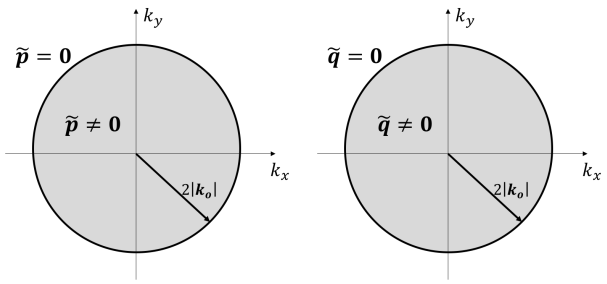

(a) (b)

Fig. 2.2. Pictorial view of the spectral meaning of the approximated inverse scattering problem: (a) CS-EBA (and also EBA) ($\tilde{p} = \mathscr{F}[p]$) and (b) SPFA($\tilde{q} = \mathscr{F}[q]$) .

2.3.3 Some useful remarks for Born, CS-EB and SPF approximations

In all cases of Born, CS-EB and SPF approximation the scattered field can be seen as the restriction to a circle of radius $2|\boldsymbol{k}_o| = 2k_b$ of the Fourier transform of some variables embedding the constitutive relationship of the obstacles. In fact, these latter variables are the contrast function $\chi(\boldsymbol{r})$, the $p(\boldsymbol{r})$ function and the $q(\boldsymbol{r})$ function, respectively. Such a circumstance has (at least) three interesting consequences, i.e.:

i. as $\chi(\boldsymbol{r})$, $p(\boldsymbol{r})$ and $q(\boldsymbol{r})$ have limited support, their Fourier transform is band-limited. If the overall scatterer is contained within a circle of radius a, the proper sampling ratio in the transformed domain is less than or equal to $\frac{1}{2a}$. Then, the number (#) of independent equations one has at his/her disposal for the inversion is given by (in terms of the angular frequency):

$$\#\ indep.\ eqs. = \#\ of\ samples\ following\ within\ the\ circle\ of\ radius\ 2k_b$$

In terms of frequencies rather that the angular frequencies, one has:

$$\#\ indep.\ eqs. = \frac{\pi\left(2k_b/2\pi\right)^2}{\left(1/2a\right)^2} = \frac{\pi\left(2/\lambda\right)^2}{\left(1/2a\right)^2} = 16\pi\left(\frac{a}{\lambda}\right)^2$$

so that, coherently with [18], the # of independent equations one has at his/her disposal is finite and (whatever of the three approximations) the inverse scattering problem is ill-posed.

Also note the average resolution one may achieve is given by:

$$resolution^2 = \frac{\pi a^2}{\#\ indep.\ equations} = \frac{\lambda^2}{16} = \left(\frac{\lambda}{4}\right)^2$$

which is slightly worse than the one in [18] (corresponding to $\Delta x = \Delta y \simeq \lambda/5$, rather than $\lambda/4$, Δx, Δy being the sides length of the sampling cell).

ii. As the scattered fields are related to the unknown function ($\chi(\boldsymbol{r})$, or $p(\boldsymbol{r})$, or $q(\boldsymbol{r})$) by a Fourier transform, the incoherence properties required by the CS theory are fully satisfied. As a consequence, CS can be reliably used provided $\chi(\boldsymbol{r})$, $p(\boldsymbol{r})$ or $q(\boldsymbol{r})$ are sparse (in a pixel sense).

iii. The spectral coverage clearly indicates which kind of profiles can be safely reconstructed, and which of them are instead expected to be "invisible" (see Sect. 4.2 for more details).

2.4 Two new inversion methods: the "DVE" and the "DIVE" approaches

2.4.1 The virtual experiments framework and the "VELI" approximation

The intrinsic non linear nature of the inverse scattering problem has led to develop a number of solution strategies and approximations. It is worth to stress that any possible a priori information about the nature or the features of the problem's unknowns as well as pre-processing methods are helpful and have to be exploited in order to reduce the problem's difficulty.

Notably, some helpful features and/or behaviors of the actual unknown are not necessarily assumed but enforced. Moving from this comment, the *virtual experiments* (VE) based linear field approximation (VELI) has been recently proposed in literature [84] paving the way for a number of publications confirming the effectiveness of the solution strategy [41, 73, 74, 85–94].

The key point of the VELI approximation is to consider that, thanks to the linearity of the Maxwell's equations with respect to the primary sources, a linear combination of the *causes* (i.e., the incident fields E_i) with known coefficients, gives rise to the same linear combination, with the same weighting coefficients, of the *effects* (i.e., the scattered and total fields, E_s and E). In formulas:

$$\mathcal{E}_i(\boldsymbol{r}) = \sum_{t=1}^{N} \alpha_t E_i(\boldsymbol{r}, \boldsymbol{r}_t) \tag{2.18}$$

$$\mathcal{E}(\boldsymbol{r}) = \sum_{t=1}^{N} \alpha_t E(\boldsymbol{r}, \boldsymbol{r}_t) \tag{2.19}$$

$$\mathcal{E}_s(\boldsymbol{r}_o) = \sum_{t=1}^{N} \alpha_t E_s(\boldsymbol{r}_t, \boldsymbol{r}_o) \tag{2.20}$$

Note that a chance arises. In fact, one can try to determine the α_t coefficients in such a way to enforce a specific behavior on the total (or scattered) field. Then, such a characteristics could be usefully exploited for the solution of the inverse problem.

In [95] has been shown that, if properly designed, the weighting parameters α_t allow to obtain a scattered field emerging as a cylindrical wave from a given point (named 'pivot point') inside the scatterer. To accomplish such a goal, the original scattered field can be used as available data and the arising design equation reads:

$$\mathcal{E}_s(\boldsymbol{r}_o, \boldsymbol{r}_p) = \sum_{t=1}^{N} \alpha(\boldsymbol{r}_t, \boldsymbol{r}_p) E_s(\boldsymbol{r}_t, \boldsymbol{r}_o) = g(\boldsymbol{r}_o, \boldsymbol{r}_p) \tag{2.21}$$

where $\boldsymbol{r}_o \in \Gamma$, $\boldsymbol{r}_p \in \Omega$ is the considered pivot point, $\alpha(\boldsymbol{r}_t, \boldsymbol{r}_p)$ are the set of coefficients required to build the VE, while the right-hand side is the field radiated on Γ by an elementary source located in $\boldsymbol{r}_p$, with $p = 1, ..., P$.

Interestingly, eq.(2.21) is nothing but the discretized version of the well-known Far Field Equation (FFE), i.e., the basic (linear) equation underlying the Linear Sampling Method (LSM) [96, 97], with $\boldsymbol{r}_p$ playing the role of the sampling point. Accordingly, the problem cast in (2.21) is ill-conditioned and has to be solved through some regularization strategies. Its regularized solution is commonly exploited to recover the shape of unknown targets by simply plotting (in a logarithmic scale) the energy of the solution over the sampling grid.
Obviously, in order to select the P pivot points, the scatterer's support must be previously estimated. To this end, the LSM can be again exploited.

By performing several (software) rearrangements of the original experiments, a set of new experiments can be organized which do not require new experimental measurements. For this reason, we denote them as 'virtual' experiments. Note that no a priori information on the contrast function is needed to generate VE. Clearly, VE are

just a different way to consider or to re-weight the originally collected information. In fact, the amount of information carried by VE cannot exceed that of the original ones, and some information could be actually lost if they are not properly designed. Naturally, recombining in different way the original experiments acting on the coefficients $\alpha(\boldsymbol{r}_t, \boldsymbol{r}_p)$ gives rise to a different total fields $\mathcal{E}(\boldsymbol{r})$ exhibiting different given behaviors. For more details on the VE physical interpretation as well as to the implementation of the regularized solution of the FFE, please refer to [95, 98, 99].

Provided that a solution of (2.21) can be actually found, we are able to build new experiments in such a way that the arising (virtual) scattered field exhibits a circular symmetric behavior. The same holds for the (virtual) total field. Accordingly, the data equation (1.3) can be recast as follow:

$$\mathcal{E}_s(\boldsymbol{r}_o) = \mathcal{A}_e[\chi(\boldsymbol{r})\mathcal{E}(\boldsymbol{r})] \tag{2.22}$$

where $\mathcal{E}(\boldsymbol{r})$ and $\mathcal{E}_s(\boldsymbol{r}_o)$ are defined in eqs.(2.19)-(2.20).

The new (virtual) data equation (2.22) is still non-linear in terms of the unknowns, as both $\chi(\boldsymbol{r})$ and $\mathcal{E}(\boldsymbol{r})$ are unknown. However, the peculiar nature of the design equation, which enforces the target to behave like a point-like source (observing the scattered field on Γ), allows to perform a simple analytical prolongation of the field from the measurement line to the investigated area, thus providing an alternative approximation of the scattered field inside the target, and hence for the total field $\mathcal{E}(\boldsymbol{r})$ in the whole domain Ω.

Accordingly, for each pivot point $\boldsymbol{r}_p$ the total field in Ω can be conveniently approximated by means of the following expression [84]:

$$\mathcal{E}(\boldsymbol{r}, \boldsymbol{r}_p) \approx \mathcal{E}_i(\boldsymbol{r}, \boldsymbol{r}_p) + LP[g(\boldsymbol{r}, \boldsymbol{r}_p)] \tag{2.23}$$

wherein the first addendum at the right-hand side is the incident field arising in the VE and the second addendum is a low pass version of the internal Green's function, where the low-pass filtering is meant to avoid the field singularity in the pivot point.

As a final comment, it is worth to stress that the VELI approximation results as a scatterer-aware approximation, since the pivot points on which build the new experiments are chosen inside the support of the target and the α_t coefficients depend on the originally scattered fields. For this reason, its range of validity is wider than the BA and it is viable for a large class of non-weak targets. The above statement has been demonstrated with an extended numerical analysis in [86], where some guidelines to foresee the capability of the approximated method in imaging an unknown object are given. In particular, it has been found that the quantity $\sqrt{\varepsilon_r}d = 1.22\lambda$ (d being the

diameter of the scatterer) constitutes an upper bound for the method's applicability, which is more than three times larger than the one in the case of the BA (0.35λ) [53].

2.4.2 The distorted virtual experiments (DVE) method

As a natural evolution of the above linearization strategy (which has been derived in the case of free space or anyway homogeneous background), the basic approach can be extended to the case where the scatterer of interest (i.e., the object of the imaging procedure) is hosted in a known, or partially known, non-homogeneous scenario.
While this class of linearized methods has been originally inspired by the possibility of using, if available, a closed form solution of the fields in the reference scenario, their interest is nowadays motivated by the possibility of modeling complex, non-canonical scenarios via accurate and efficient numerical tools, so to conveniently tackle more and more realistic scenarios.

The basic and cornerstone contribution in such a framework is the well known DBA [45]. In this approach, the problem is formulated as the search of the difference in the permittivity distribution with respect to a nominal ground-truth by processing the anomalous field. In so doing, the DBA approximates the internal field with the background one, thus neglecting the effect of the 'perturbation' on the field. This is, from a conceptual point of view, the same limitation underlying the first order BA, where the effect of the scatterer on the incident field in the investigation domain is completely neglected. As a result, this leads to a linearization of the problem that is seldom fulfilled in practical instances.

By following the same reasoning, in the following the VELI method introduced in the previous section is extended to the case of a partially known, non-homogeneous scenarios and exploited to appraise the properties of non-weak anomalies. To this end, the key step is to extend the concept of virtual experiments from the so far considered canonical case to the case of a non-homogeneous scenarios. In practice, this is done by exploiting the "distorted" version of the LSM [100].

Let Ω be the region of interest (ROI) of the imaging problem, given by the cross section of an infinite cylinder with non homogeneous relative complex permittivity distribution $\tilde{\varepsilon}_r(\boldsymbol{r})$. Assume that the relative permittivity distribution within the ROI is partially known so that the complex permittivity in the whole space can be expressed as:

$$\tilde{\varepsilon}_r(\boldsymbol{r}) = \tilde{\varepsilon}_b(\boldsymbol{r}) + \Delta\tilde{\varepsilon}(\boldsymbol{r}), \tag{2.24}$$

with:

$$\tilde{\varepsilon}_b(\boldsymbol{r}) = \begin{cases} \tilde{\varepsilon}_1(\boldsymbol{r}) & \boldsymbol{r} \in \Omega \\ \tilde{\varepsilon}_{host}(\boldsymbol{r}) & \boldsymbol{r} \notin \Omega \end{cases} \tag{2.25}$$

wherein $\boldsymbol{r} = (x, y)$, $\tilde{\varepsilon}_{host}$ is the complex permittivity of the homogeneous medium which surrounds Ω and $\tilde{\varepsilon}_1$ denotes the 'nominal' relative permittivity distribution in Ω, i.e., when no perturbation is present. Saying it in other words, eq.(2.24) expresses the complex permittivity of the scenario at hand as a "perturbation" with respect to a nominal background permittivity distribution.

Note that, for the sake of simplicity, we are assuming that the medium outside the ROI is homogeneous. However, the following discussion holds true also for the general inhomogeneous case.

By considering transmitting and receiving probes positioned at $\boldsymbol{r}_t$ and $\boldsymbol{r}_o$, respectively, on a curve Γ external to the ROI, the anomalous field $\Delta E_s(\boldsymbol{r}_t, \boldsymbol{r}_o)$ produced by the perturbation $\Delta\tilde{\varepsilon}$ is expressed by the integral *data* equation which follows:

$$\Delta E_s(\boldsymbol{r}_t, \boldsymbol{r}_o) = \int_\Omega g_b(\boldsymbol{r}_o, \boldsymbol{r}')\Delta\tilde{\varepsilon}(\boldsymbol{r}')E(\boldsymbol{r}', \boldsymbol{r}_t)d\boldsymbol{r}' = \mathcal{A}_e\left[\Delta\tilde{\varepsilon}E\right] \tag{2.26}$$

in which, the total field E is given by the following *state* equation:

$$E(\boldsymbol{r}, \boldsymbol{r}_t) = E_b(\boldsymbol{r}, \boldsymbol{r}_t) + \int_\Omega g_b(\boldsymbol{r}', \boldsymbol{r})\Delta\tilde{\varepsilon}(\boldsymbol{r}')E(\boldsymbol{r}', \boldsymbol{r}_t)d\boldsymbol{r}' = E_b(\boldsymbol{r}, \boldsymbol{r}_t) + \mathcal{A}_i\left[\Delta\tilde{\varepsilon}E\right] \tag{2.27}$$

wherein E_b represents the background field (i.e., when no anomalies are present).

In eqs.(2.26) and (2.27) g_b denotes the Green's function for the assumed (non homogeneous) background scenario, $\left[\nabla^2 + k_b^2(\boldsymbol{r})\right] g_b(\boldsymbol{r}', \boldsymbol{r}) = \delta(\boldsymbol{r}' - \boldsymbol{r})$, with k_b being the reference scenario wavenumber. Typically, this function is not known in a closed form and it is computed numerically. $\mathcal{A}_e[\cdot] : L^2(\Omega) \to L^2(\Gamma)$ is the short notation of the radiation operator that relates the contrast source $\Delta\tilde{\varepsilon}E$ to the anomalous field on Γ, while the operator $\mathcal{A}_i[\cdot] : L^2(\Omega) \to L^2(\Omega)$, relates the contrast source to the field it radiates in Ω.

It is worth noting that the knowledge of the reference scenario is also exploited to appraise the scattered field perturbation ΔE_s starting from the quantity actually measured by the receiving probes, say M_t, which is affected by both the perturbation and the reference scenario. Accordingly, it is possible to extract the required field from this latter as:

$$\Delta E_s(\boldsymbol{r}_t, \boldsymbol{r}_o) = M_t(\boldsymbol{r}_t, \boldsymbol{r}_o) - M_b(\boldsymbol{r}_t, \boldsymbol{r}_o) \tag{2.28}$$

in which:

$$M_b(\boldsymbol{r}_t, \boldsymbol{r}_o) = E_i(\boldsymbol{r}_t, \boldsymbol{r}_o) + \int_\Omega g_h(\boldsymbol{r}_o, \boldsymbol{r}')\Delta\tilde{\varepsilon}(\boldsymbol{r}')\left[\tilde{\varepsilon}_1(\boldsymbol{r}') - \tilde{\varepsilon}_{host}\right]E_b(\boldsymbol{r}_t, \boldsymbol{r}')d\boldsymbol{r}' \tag{2.29}$$

with E_i the field radiated by the transmitting antennas in the host medium and g_h denoting the Green's function of the same homogeneous medium. Note that, depending

on the imaging problem at hand, $M_b(\boldsymbol{r}_t, \boldsymbol{r}_o)$ can be actually measured (if the "perturbation" arises in the nominal background) or estimated by properly simulating the reference scenario.

The traditional DBA descends from the above equations by assuming that the variation $\Delta\tilde{\varepsilon}$ is such to induce only a negligible perturbation of the background field E_b. Accordingly, the data equation (2.27) is approximated as:

$$\Delta E_s(\boldsymbol{r}_t, \boldsymbol{r}_o) = \mathcal{A}_e[\Delta\tilde{\varepsilon} E_b], \qquad \boldsymbol{r}_t, \boldsymbol{r}_o \in \Gamma \tag{2.30}$$

and the imaging task is reduced to the solution of a linear ill-posed inverse problem.

Obviously, when the reference scenario corresponds to a homogeneous unbounded medium, this approximation exactly coincides with the classic BA, so that the DBA will be subject to the same restrictions (in terms of applicability). In particular, the approximation is expected to be successful as long as the perturbation is small enough with respect to the background wavelength and its dielectric properties are close to those of the ROI [44, 45].

To overcome the above recalled limitations, the VE framework has been extended to the case at hand. As already introduced in the previous section, a first preprocessing step is needed to solve qualitatively the inverse scattering problem and chose the pivot points. The problem of retrieving the shape of targets hosted in a partially known non canonical scenario has been faced in [100], wherein the necessary steps to generalize the LSM to this case have been defined and tested. The resulting distorted LSM equation becomes the new design equation in the unknowns $\alpha(\boldsymbol{r}_t, \boldsymbol{r}_s)$, with $\boldsymbol{r}_s$ denoting the sampling point, which reads:

$$\sum_{t=1}^{N} \alpha(\boldsymbol{r}_t, \boldsymbol{r}_s) \Delta E_s(\boldsymbol{r}_t, \boldsymbol{r}_o) = g_b(\boldsymbol{r}_o, \boldsymbol{r}_s) \tag{2.31}$$

The virtual experiments designed through (2.31) make use of the available knowledge on the scenario at hand, since they force the unknown perturbation to scatter a wave that matches on Γ the background Green's function for the considered sampling point $\boldsymbol{r}_s$ in the ROI. As a matter of fact, by paralleling the arguments for the homogeneous case, a regularized solution for (2.31) can be found in order to compute and plot the following function:

$$\Upsilon(\boldsymbol{r}_s) = \frac{log_{10} \|\alpha\| - log_{10} \|\alpha\|_{max}}{min \{log_{10} \|\alpha\| - log_{10} \|\alpha\|_{max}\}} \tag{2.32}$$

wherein $\|\cdot\|$ is the ℓ_2-norm, and Υ defines an indicator for the support of $\Delta\tilde{\varepsilon}$ on which we can select evenly spaced P (at most) pivot points. Then, P virtual experiments are built. In each of these experiments, the total field is exactly given by:

$$\mathcal{E}(\boldsymbol{r},\boldsymbol{r}_p)=\mathcal{E}_b(\boldsymbol{r},\boldsymbol{r}_p)+\mathcal{A}_i\left[\Delta\tilde{\varepsilon}\mathcal{E}\right] \tag{2.33}$$

wherein the first addendum $\mathcal{E}_b(\boldsymbol{r},\boldsymbol{r}_p)=\sum_{t=1}^{N}\alpha(\boldsymbol{r}_t,\boldsymbol{r}_p)E_b(\boldsymbol{r},\boldsymbol{r}_p)$ is the background field arising in the reference scenario for the considered virtual experiment. This latter has the remarkable property of depending on the unknown permittivity perturbation $\Delta\tilde{\varepsilon}$ in an implicit fashion through the combination coefficients $\alpha(\boldsymbol{r}_t,\boldsymbol{r}_p)$.

Then, a first order approximation would be immediately achieved by neglecting the second term in (2.33). However, thanks to the features of the designed virtual experiments, a more refined field approximation can be considered. To this end one has to observe that the field scattered on Γ in the generic virtual experiment matches (in the ℓ_2-norm) the Green's function for the reference background medium, g_b. Notably, such a scattered (anomalous) field does not depend on $\Delta\tilde{\varepsilon}$, but only depends on the pivot points. As such, it is known for any $\boldsymbol{r}$. Accordingly, the first order approximation (i.e., $\mathcal{E}\approx\mathcal{E}_b$) can be improved by assuming that the virtual anomalous field matches g_b not only on Γ, but everywhere. Hence, we can introduce the approximated total field:

$$\mathcal{E}(\boldsymbol{r},\boldsymbol{r}_p)\approx\mathcal{E}_b(\boldsymbol{r},\boldsymbol{r}_p)+LP[g_b(\boldsymbol{r},\boldsymbol{r}_p)] \tag{2.34}$$

with $\boldsymbol{r}_p$ denoting the pivot point identifying the virtual experiment at hand and LP being a low-pass circular filter which avoids singularity of the approximated total field for $\boldsymbol{r}=\boldsymbol{r}_p$ [84].

As discussed in [84, 86] for the corresponding free space case, this approximation is superior to the straightforward linearization on which BA and DBA are based, although of course has itself a limited validity due to the fact that near field effects and non-radiating components of the fields are neglected.

Approximation (2.34) relies on the applicability of the design equation (2.31), which is the case in all those situations wherein LSM is successful [84, 97, 101]. According to literature results, the LSM equation and its distorted formulation are successful as long as the anomalies are comparable with the wavelength of the probing field. When the scattering system becomes too large (with respect to the probing wavelength) it is more difficult to induce a contrast source resembling the radiating properties of an elementary source point placed in the pivot point. An accurate study of the validity range of the considered approximation has yet to be done. However, relying on the results in [86] it can be expected that approximation (2.34) starts to fail for increasing values of $\Delta\tilde{\varepsilon}$ (with respect to $\tilde{\varepsilon}_1$). In particular, the larger $\Delta\tilde{\varepsilon}$, the smaller electrical dimension (with respect to the probing wavelength) of the anomaly that can be retrieved.

By means of such an approximation, we finally come to a new linear distorted-wave data equation that reads:

$$\Delta\mathcal{E}_s(\boldsymbol{r}_o, \boldsymbol{r}_p) = \mathcal{A}_e\left[\Delta\tilde{\varepsilon}(\boldsymbol{r})\mathcal{E}(\boldsymbol{r}, \boldsymbol{r}_p)\right] \tag{2.35}$$

It is worth to note that the problem (2.35) is linear but it is still ill-posed, so that a regularization is needed to obtain physically meaningful solutions. In the following, two regularization approaches have been considered.

The first one is the usual 'truncated singular value decomposition' (TSVD) [4], which gives the following solution:

$$\boldsymbol{\Delta\tilde{\varepsilon}} = \sum_{j=1}^{N_T} \frac{1}{\boldsymbol{\sigma_j}} \langle \boldsymbol{\Delta\mathcal{E}_s}, \boldsymbol{w_j} \rangle \boldsymbol{z_j} \tag{2.36}$$

wherein $\boldsymbol{z_j}$ and $\boldsymbol{w_j}$ are the right and left singular vectors of the matrix $\boldsymbol{A}$ relating the unknown vector $\boldsymbol{\Delta\tilde{\varepsilon}}$ to the data vector $\boldsymbol{\Delta\mathcal{E}_s}$ according to the linear relationship (2.35), respectively, $\boldsymbol{\sigma_j}$ are its singular values, while the truncation index N_T enforcing the regularization is appraised by means of the Picard's plot [84, 102, 103]. In fact, this plot exhibits a change of slope when the solution passes from being dominated by regularization error to being dominated by noise: the index corresponding to such a change represents the right choice for N_T.

While the TSVD is a sort of "general purpose" regularization, the second strategy involves a 'sparsity promotion' scheme. In particular, a TV approach has been implemented to assess the inversion procedure for extended objects exhibiting piece-wise constant complex permittivity distributions, which is a rather common circumstance when dealing with man-made objects. Recently, also the adoption of a wavelet-based regularization has demonstrated the effectiveness to achieve multiresolution in case of biomedical imaging [104].

By using one of the typical CS procedure, the linearized inverse problem (2.35) can be solved by means of minimization of the following objective function:

$$\min_{\Delta\tilde{\varepsilon}} \left\{ \|\boldsymbol{D_h}\boldsymbol{\Delta\tilde{\varepsilon}}\|_{\ell_1} + \|\boldsymbol{D_v}\boldsymbol{\Delta\tilde{\varepsilon}}\|_{\ell_1} + \left\|\boldsymbol{D_d}^{+}\boldsymbol{\Delta\tilde{\varepsilon}}\right\|_{\ell_1} + \left\|\boldsymbol{D_d}^{-}\boldsymbol{\Delta\tilde{\varepsilon}}\right\|_{\ell_1} \right\}$$
$$\textit{subject to} \quad \|\boldsymbol{A}\boldsymbol{\Delta\tilde{\varepsilon}} - \boldsymbol{\Delta\mathcal{E}_s}\|_{\ell_2} \leq \delta \tag{2.37}$$

where $\boldsymbol{D_h}$, $\boldsymbol{D_v}$ and $\boldsymbol{D_d}$ are the vectors containing the horizontal, vertical and diagonal (i.e., along direction parallel to the principal (+) and secondary (-) diagonal) forward differences of the considered function $\boldsymbol{\Delta\tilde{\varepsilon}}$, respectively.

A crucial point is the choice of the parameter δ in (2.37), which represents the level of accuracy required in satisfying (2.35). Of course, it has to take into account the noise level as well as the model error introduced by the approximation (2.34). In order

to avoid the trivial solution, that is the null vector, δ must be selected lower than $\|\boldsymbol{\Delta\mathcal{E}_s}\|_{\ell_2}$, since with $\delta \geq \|\boldsymbol{\Delta\mathcal{E}_s}\|_{\ell_2}$ the null vector could satisfy the constraint on the data and simultaneously minimize the objective function. Accordingly, in performing the numerical analysis, it is considered $\delta = \hat{\delta}\,\|\boldsymbol{\Delta\mathcal{E}_s}\|_{\ell_2}$ with $0 < \hat{\delta} < 1$ [105].

Note that the solution approach adopted here is not meant to be a rigorous implementation of the standard CS recovery strategies but it is rather inspired from CS. As a consequence, we will not need to discuss RIP and the like. On the other side, contents of Sect.2.3 give a reasonable basis for a successful application of the CS framework.

As a final comment, let us compare the computational burden and the expected performances of the DVE method with respect to DBA, as well as to the well-known EBA [53, 55] and diagonalized contrast source inversion (DCSI) [56] approaches.
Notably, with respect to DBA, the additional computational burden just resides in the first step of the procedure, namely the solution of the design equation to retrieve the weighting coefficients and define the new linear approximation. In fact, the inversion step has exactly the same computational burden of DBA as, in both cases, one needs the knowledge of the Green's function of the reference scenario for all pairs of points ($\boldsymbol{r}' \in \Omega$, $\boldsymbol{r} \in \Gamma$), which has to be computed numerically (but for special cases). This task can be accomplished by first considering at each measurement position $\boldsymbol{r}_o$ an elementary source and solving the corresponding forward scattering problem $\forall \boldsymbol{r} \in \Omega$. Then, exploiting the reciprocity theorem, $g_b(\boldsymbol{r}, \boldsymbol{r}_o) = g_b(\boldsymbol{r}_o, \boldsymbol{r})$. In eq.(2.34) one also needs the overall Green's functions for all the pivot points (i.e., all functions $g_b(\boldsymbol{r}_p, \boldsymbol{r})$, $p = 1, ..., P, \boldsymbol{r} \in \Omega$). This latter can be numerically computed by solving P forward problems considering for each of them a unitary filamentary current placed in the considered pivot point, and computing the field for $\boldsymbol{r} \in \Omega$. Moreover, the solution of the design equation (2.31) requires a SVD of a matrix whose dimension is related to the number of experiments (and not to the number of pixels), so that such a step has a negligible computational weight even in case of 3D problems. As the solution of the additional forward problems which are needed to compute $g_b(\boldsymbol{r}_p, \boldsymbol{r})$ functions can be performed by taking advantage of parallel computing, the overall computational time can be kept only slightly larger than in DBA.
As far as comparison with EBA is concerned, note that such a method also consists in the sequence of two linear inversion steps. However, it requires the knowledge of the Green's function for all possible couples ($\boldsymbol{r} \in \Omega$, $\boldsymbol{r}' \in \Omega$) so that the computational burden is greatly increased with respect to DBA and to the proposed method as well. Moreover, EBA is based on the assumption that interactions among distant points can

be neglected. As such, it will be possibly accurate only in the presence of a sufficient amount of losses, which is obviously not the more general case.
The DCSI, which can be considered an evolution of EBA, simultaneously looks for the contrast function and an auxiliary function $\eta(\boldsymbol{r})$ representing a proportionality function among the incident field and the contrast source (for all views). As such, it is a fast method. However, one cannot be sure that such a function exists, as one can have a total field different from zero also in points where E_i is zero, so that the auxiliary function cannot be used in these cases. Also note that such a proportionality assumption is deeply different in spirit from our approximation (2.34), where a part of the total field (the second term) is not proportional to E_i at all. Hence, different performances and/or ranges of convenience are expected between DCSI and the proposed method. Moreover, it is worth noting that, to the best of my knowledge, both EBA and DCSI have been applied to the canonical homogeneous space case, and not to the distorted wave problem we are tackling herein.

To give an assessment of the proposed approach, the above described procedure has been applied both to simulated data and experimental data taken from the 2005 Fresnel database [106] and we have compared the performance with those achieved with both DBA and a modified version of EBA adapted to handle "distorted" problems (DEBA).

Results: numerical data

In this section, the proposed approach has been tested against a complex scenario, consisting of a cross-section of a radially stratified structure made of three concentric layers and an inner core, see figs.2.3(a)-2.3(b). This structure can be thought as a rough phantom for different applications such as medical [15] and living tree trunk microwave diagnostics [107]. The dimensions and the dielectric properties of the layers are reported in Table 2.1.

Table 2.1. DVE with numerical data: stratified scenario. Geometrical and dielectric properties (permittivity and conductivity) of the radially layered scatterer from the outermost to the innermost layer

$\boldsymbol{\varepsilon_r}$	$\boldsymbol{\sigma}$ $[mS/m]$	***Thickness*** $[cm]$
6.2	2	1
22	5	4.8
16	1	8.67
9	0.5	10.6

The diameter of the overall structure is 50 cm and it is embedded into an imaging domain of side 52.5 cm. The ROI has been discretized into 79×79 cells according to [108], and it is probed by means of a circular array of antennas placed at 12.5 cm from the outermost layer. The number of antennas is set to 21 at the working frequency of 650 MHz. The total field at the receivers is measured in presence of an elliptic shaped anomaly placed in the core at (4.2,-2) cm, representing a void with axes' dimensions of 8 cm and 12 cm, see figs.2.3(c)-2.3(d). In order to cope with an optimized imaging setup, a lossless matching medium with $\tilde{\varepsilon}_{host} = 4.7$ has been considered by following the transmission line model developed in [36], in order to guarantee a good coupling between the incoming incident wave and the structure.

To take into account the effect of the measurement noise, the useful signal defined in eq.(2.28) has been corrupted by white random Gaussian noise with given Signal-to-Noise Ratio (SNR). In order to show the robustness of the proposed approach against the measurement noise, in the following two different levels of noise, i.e., SNR=20dB and SNR=7dB will be considered. The accuracy of the result is appraised by exploiting the mean square error:

$$err = \frac{||\Delta\tilde{\varepsilon} - \widehat{\Delta\tilde{\varepsilon}}||^2}{||\Delta\tilde{\varepsilon}||^2} \tag{2.38}$$

where $\Delta\tilde{\varepsilon}$ is the actual perturbation profile as shown in figs.2.3(e)-2.3(f), $\widehat{\Delta\tilde{\varepsilon}}$ the estimated one.

The first step of the procedure is the application of the (distorted) LSM in order to identify the presence of the anomalies. Thereafter we take advantage of the energy indicator (2.32) to choose the pivot points and to design the virtual experiments. The LSM energy indicators with superimposed the pivot points are shown in figs.2.4(a)-2.4(d), while the outcome of the inversion procedure by means of the TSVD regularization scheme is shown in figs.2.4(b)-2.4(c) and figs.2.4(e)-2.4(f), respectively for the two considered SNR. As it can be seen, the proposed approach is able to achieve a quite satisfactory reconstruction of the unknown both for SNR=20dB ($err = 38\%$) and SNR=7dB ($err = 62\%$). In particular, as far as the real part of $\Delta\tilde{\varepsilon}$ is concerned, the procedure is able to recover the dielectric constant of the void despite of the distribution of the imaginary part because of its very low value. In figs.2.4(g)-2.4(h) the retrieved electromagnetic properties by means of the DEBA strategy are shown. The adopted inversion procedure deals with the two linear step introduced in [55]. The first step is the inversion of the data equation in which the unknown is an auxiliary function. Thereafter, the Fredholm integral equation of second kind is solved by adopting a least square minimization. In this case, the result is not satis-

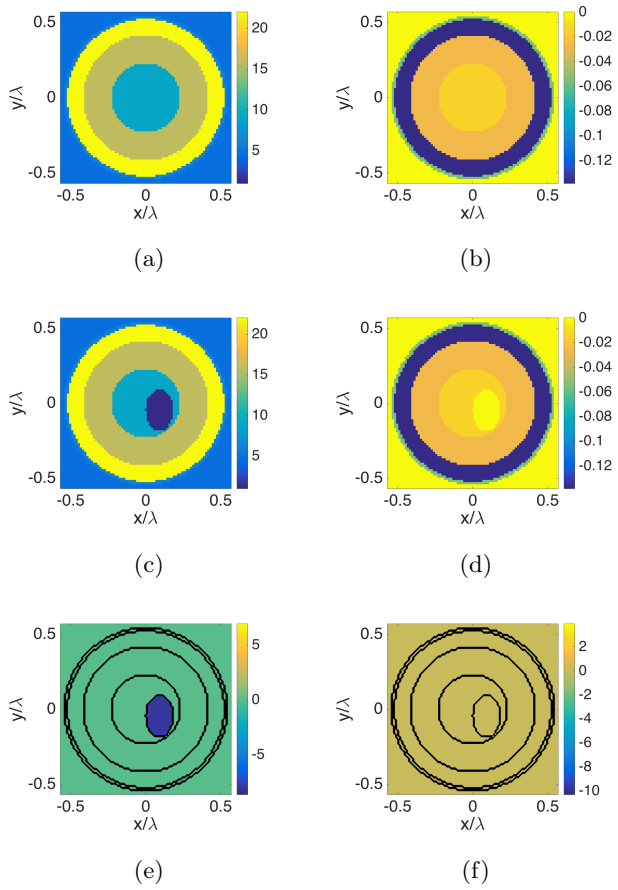

Fig. 2.3. DVE with numerical data: stratified scenario. (a) Real and (b) imaginary part of the permittivity function of the reference scenario. (c) Real and (d) imaginary part of the permittivity function of the perturbed scenario: in the inner layer a 'void' is considered as anomaly. (e) Real and (f) imaginary part of the actual unknown $\Delta\tilde{\varepsilon}$.

factory ($err = 137\%$), even if it outperforms the results obtained with the DBA (see figs.2.4(i)-2.4(j)) in recovering the imaginary part ($err = 146\%$).

As an alternative to the more general TSVD based scheme, a sparsity promoting regularization approach formalized in eq.(2.37) has been also exploited for the inversion step. The achieved result for $\hat{\delta} = 0.3$ is shown in figs.2.5(a)-2.5(b) from which it is possible to note the accuracy deriving from the CS based strategy, also confirmed by the very low synthetic error corresponding to $err = 10\%$. Conversely, the exploitation of the sparsity promoting strategy for the DBA model does not allow to improve the reconstruction which is reported in figs.2.5(c)-2.5(d) ($err = 148\%$, $\hat{\delta} = 0.1$).

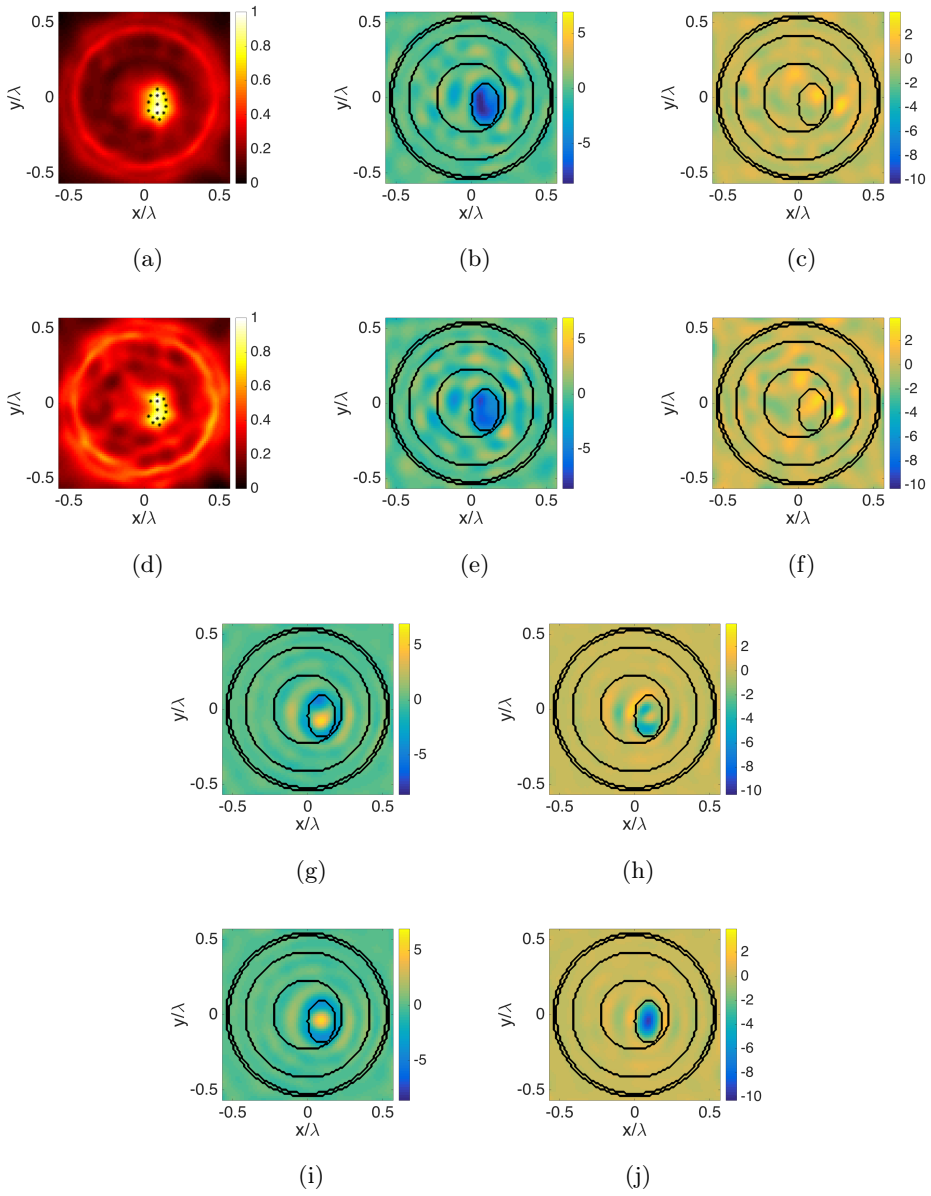

Fig. 2.4. DVE with numerical data: stratified scenario. (a) Logarithmic plot of the LSM map indicator when normalized to its maximum with superimposed the pivot points marked as stars for SNR=20 dB. (b) Real and (c) imaginary part of the retrieved perturbation $\Delta\tilde{\varepsilon}$ by means of DVE-TSVD. (d)-(f) are the same of (a)-(c) but for SNR=7 dB. (g) Real and (h) imaginary part of the retrieved perturbation $\Delta\tilde{\varepsilon}$ by means of DEBA-TSVD. (i)-(j) are the same of (g)-(h) but for DBA-TSVD. The black contour lines represent the geometry of the actual scenario.

Results: experimental data

In this section we test the proposed method against the experimental data of the 2005 Fresnel dataset [106]. This data set deals with non homogeneous scatterers obtained

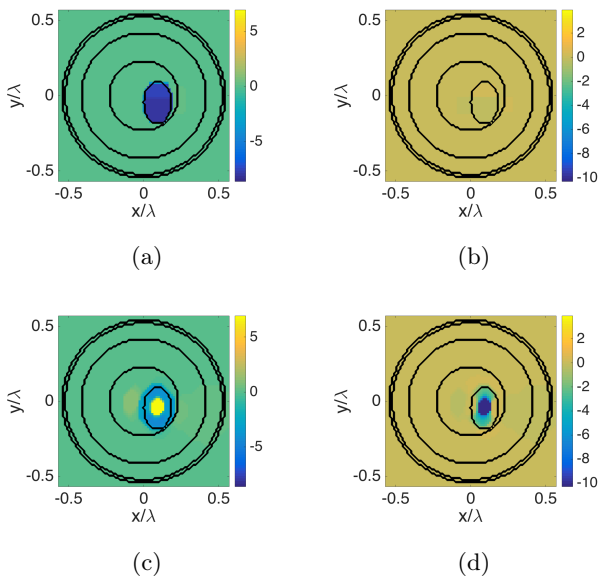

Fig. 2.5. DVE with numerical data: stratified scenario. (a) Real and (b) imaginary part of the retrieved perturbation $\Delta\tilde{\varepsilon}$ in case of DVE with sparsity promoting regularization. (c)-(d) are the same of (a)-(b) but for DBA.

by considering several configurations of nested cylinders with different dimensions and materials. This experimental setup introduces the additional difficulty of dealing with a partially aspect limited configuration, in which however illuminations completely surround the targets. In particular, for each transmitter's position, the measurements are taken only on an arc of 240°, excluding the 120° angular sector centered on the source. To apply the LSM to this kind of measurement configuration, a "zero filling" procedure has been exploited in arranging the matrix $\boldsymbol{\Delta\mathcal{E}_s}$. This procedure consists in adding zero entries for those measurement locations not available in the experimental setup.

The first considered target is the *FoamDielIntTM* in fig.2.6(a), in which a circular cylinder with radius 4 cm, with relative permittivity 1.45, embeds a smaller higher contrast circular cylinder of radius 1.5 cm and relative permittivity 3±0.3. The second target is the *FoamTwinDielIntTM* (fig.2.7(a)), which is made by placing an additional higher contrast circular cylinder in contact with the *FoamDielIntTM* target.

In both cases, to apply the proposed distorted wave method, we have assumed as reference scenario the foam cylinder, that implies to compute the background field for all the considered positions of the transmitters and receivers. Since this information is not supplied by the database, we have computed the reference field with the COMSOL®[1] 2D electromagnetic forward solver. It is worth noting that, in doing so,

[1] Courtesy of Università di Catania.

we have assumed as nominal position and nominal permittivity (of the foam cylinder) those provided by the dataset. However, since in the literature some inaccuracies in the position of the Fresnel scatterers have been experienced, it is worth noting that this could introduce a model error affecting the final result. Similar considerations can been argued for the background field, which has been performed considering an incident field obtained by means of a multipole expansion approach as suggested in [84].

The data for the *FoamDielIntTM* target have been directly supplied by the Institute Fresnel and consists of 72 incident fields and 61 measurements for each view. The ROI is a square region of side 20 cm hosting the foam cylinder and single frequency data have been processed at 3 GHz. Fig.2.6(d) reports the qualitative image of the high contrast cylinder. Such an image has been achieved by adopting a 72×90 multiview-multistatic data matrix in which the data entries not available are replaced with zeros. As it can be seen, the solution of the distorted LSM equation allows to image the support of the anomaly so that a number of evenly spaced pivot points can be chosen within it. Figs.2.6(e)-2.6(f) reports the final result obtained by applying the quantitative imaging step with respect to the selected pivot points. The retrieved permittivity, i.e., the retrieved perturbation $\Delta\tilde{\varepsilon}$, is added to the nominal background scenario. Notably, the approach achieves a satisfactory reconstruction of the target especially when compared with the DBA reconstruction (figs.2.6(b)-2.6(c)).

The outcome of the two steps for the *FoamTwinDielIntTM* target are shown in fig.2.7. In this case, the dataset consists of 18 illuminations and 241 measurements for each view. Also in this case, the foam has been assumed as background scenario. The investigated domain is a square of side 17.5 cm, the working frequency is 4 GHz. The LSM indicator shown in fig.2.7(d) has been obtained by adopting a 18×45 multiview-multistatic data matrix obtained by undersampling the original data and exploiting the "zero filling" procedure. On the basis of the retrieved support of the two cylinders, it is then possible to choose evenly spaced pivot points in order to apply the inversion strategy. Also in this case, the final result shown in figs.2.7(e)-2.7(f) is very satisfactory from a quantitative point of view. As a matter of fact, the estimated permittivity values for both cylinders are in full agreement with the nominal ones, thus confirming the capability of the method to deal with the quantitative imaging task of non-weak target and then to outperform the standard DBA (see figs.2.7(b)-2.7(c)).

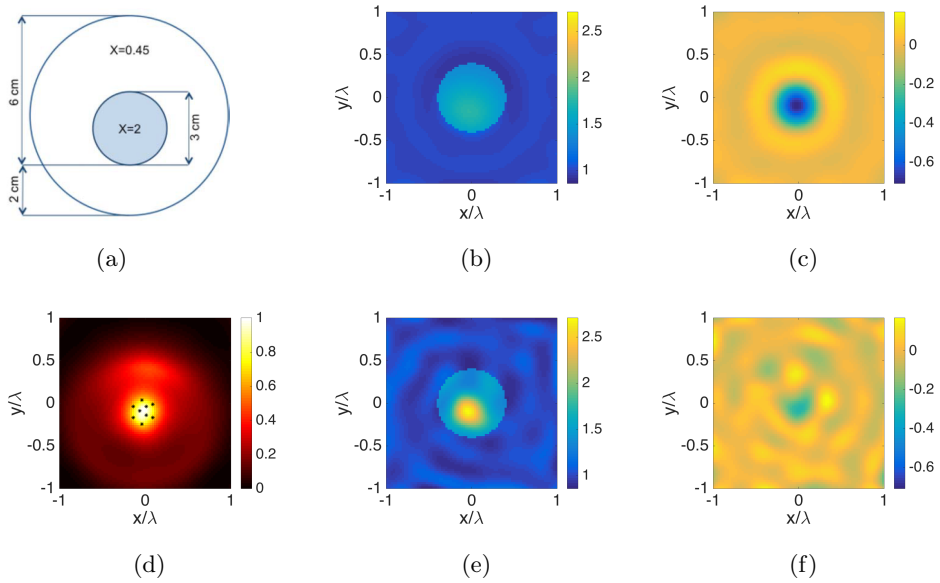

Fig. 2.6. DVE with experimental data: *FoamDielIntTM* target at 3 GHz. (a) Reference profile. (b) Real and (c) imaginary part of the retrieved perturbation $\Delta\tilde{\varepsilon}$ by means of DBA-TSVD, superimposed to the reference permittivity function. (d) Logarithmic plot of the LSM map indicator when normalized to its maximum with superimposed the pivot points marked as stars. (e)-(f) are the same of (b)-(c) but for DVE-TSVD.

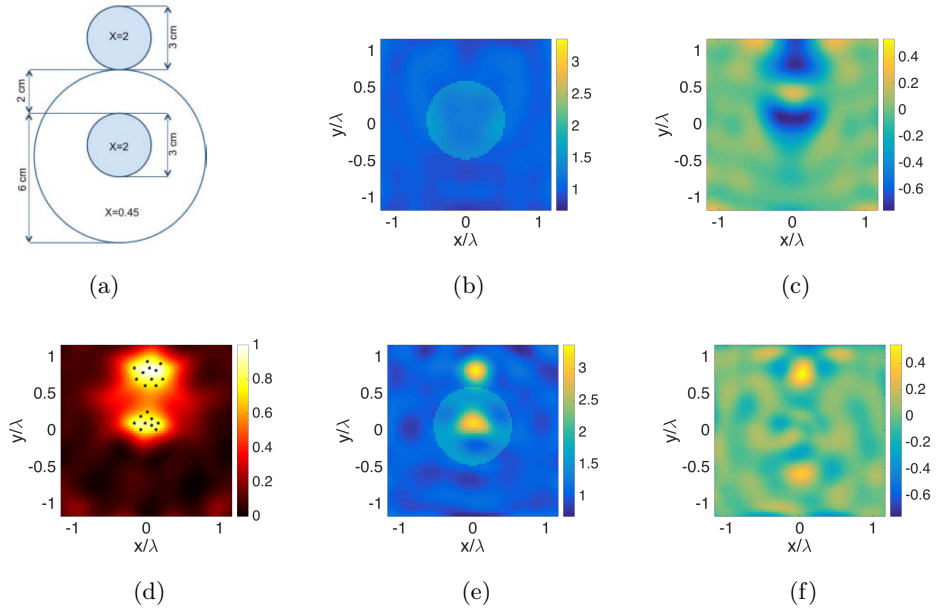

Fig. 2.7. DVE with experimental data: *TwinFoamDielIntTM* target at 4 GHz. (a) Reference profile. (b) Real and (c) imaginary part of the retrieved perturbation $\Delta\tilde{\varepsilon}$ by means of DBA-TSVD, superimposed to the reference permittivity function. (d) Logarithmic plot of the LSM map indicator when normalized to its maximum with superimposed the pivot points marked as stars. (e)-(f) are the same of (b)-(c) but for DVE-TSVD.

2.4.3 The distorted iterated virtual experiments (DIVE) method

A new iterative inversion procedure for microwave imaging based on the VE framework is herein proposed as an effective approach to tackle non-linear inverse scattering problems [91]. The structure and the complexity of the *distorted iterated virtual experiments* (DIVE) approach are comparable with those of the widely adopted DBIM [52], but its performances are remarkably better, thanks to extended validity of the 'basic bricks' (i.e., the different subsequent linear approximations). In particular, each iteration of DIVE is based on properly re-designed VE, which are updated on the basis of intermediate results. This means that, at each step, the information is rearranged (through the VE update) in such a way to take into account the features of the currently estimated background. As it can be easily guessed, each step of DIVE corresponds to the solution of a 'distorted' inverse scattering problem by means of the DVE scheme introduced in the previous section.

The proposed imaging scheme is shown in the flowchart of fig.2.8.
It is articulated in five steps:

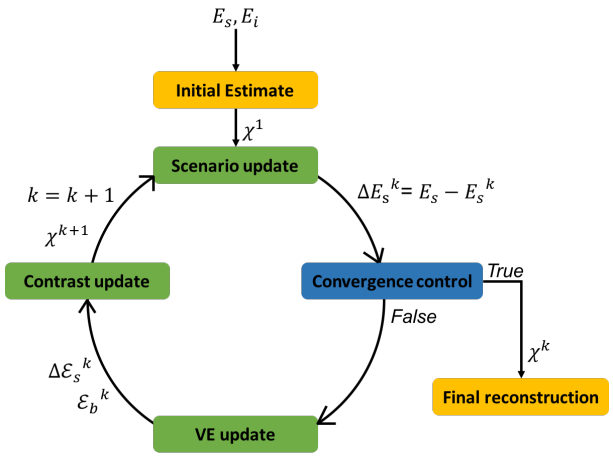

Fig. 2.8. Flowchart of the DIVE scheme.

i) *Initialization*: the initial estimate for the contrast function, χ^1, is obtained by using the VELI approximation [84]. Of course, one can consider other, more favorable, starting guesses, when available.

ii) *Scenario update*: at each iteration the scenario is updated solving the forward scattering problem for the contrast reconstructed at the previous iteration, say χ^k, which represents the background at the current iteration, say k. Such a solution updates the background field $E_b{}^k$ and the anomalous field $\Delta E_s{}^k$. Further-

more, the Green's function ${g_b}^k$ for the updated background is computed exploiting reciprocity.

iii) *Convergence control*: a stopping rule is considered by appraising the relative residual error (RRE) at k-th iteration, $RRE^k = \left\|\Delta {E_s}^k\right\|_2 / \left\|{E_s}^k\right\|_2$. If RRE^k is less than a pre-set threshold or larger than the RRE^{k-1} , the procedure is stopped and χ^k is taken as the solution of the overall problem. Otherwise, the iterative procedure continues.

iv) *VE update*: at each iteration, we build a new set of VE with respect to the current background, χ^k. This step and the following one are the main and most important differences between DBIM and DIVE. The updated VE are designed using the distorted version of the LSM [96, 100], so that they are adaptive to χ^k. In fact, from the physical interpretation of the LSM [98,109], the so-designed virtual total fields will be focused on the perturbation $\Delta\chi^k$ resembling the field radiated by a filamentary current in the reference background χ^k (see Section 2.4.2).

The design equation, for each couple of $\boldsymbol{r}_s$ and $\boldsymbol{r}_o$, reads:

$$\sum_{t=1}^{N} \alpha^k(\boldsymbol{r}_t, \boldsymbol{r}_s) \Delta {E_s}^k(\boldsymbol{r}_t, \boldsymbol{r}_o) = {g_b}^k(\boldsymbol{r}_o, \boldsymbol{r}_s) \tag{2.39}$$

where $\boldsymbol{r}_s$ is the generic point of an arbitrary grid that samples the imaging region and $\alpha^k(\boldsymbol{r}_t, \boldsymbol{r}_s)$ are the unknown coefficients. For points wherein (2.39) can be solved (in the least square sense), the coefficients provide the VE excitations, which enforce a (virtual) scattered field that matches that of an elementary source in the current background, i.e., ${g_b}^k(\boldsymbol{r}_o, \boldsymbol{r}_s)$.

To preserve diversity in the data, we create a set of VE by selecting several pivot points $\boldsymbol{r}_p$ among the sampling sets where the virtual fields are focused. To this end, the regularized solution of (2.39) is found in order to compute the function:

$$\Upsilon^k(\boldsymbol{r}_s) = \frac{log_{10}\left\|\alpha^k\right\| - log_{10}\left\|\alpha^k\right\|_{max}}{min\left\{log_{10}\left\|\alpha^k\right\| - log_{10}\left\|\alpha^k\right\|_{max}\right\}} \tag{2.40}$$

wherein $\|\cdot\|$ is the ℓ_2-norm, while Υ^k is an indicator for the support of $\Delta\chi^k$ on which we can select evenly spaced P (at most) pivot points.

v) *Contrast update via linear inversion*: the coefficients $\alpha^k(\boldsymbol{r}_t, \boldsymbol{r}_p)$ corresponding to the selected pivot points are used to compute the updated virtual background field as:

$$\mathcal{E}_b{}^k(\boldsymbol{r}, \boldsymbol{r}_p) = \sum_{t=1}^{N} {E_b}^k(\boldsymbol{r}, \boldsymbol{r}_t) \alpha^k(\boldsymbol{r}_t, \boldsymbol{r}_p) \tag{2.41}$$

Then, exploiting the properties of the designed VE [98,100], the virtual total field $\mathcal{E}^k$ is approximated as:

$$\mathcal{E}^k(\boldsymbol{r},\boldsymbol{r}_p) \approx \mathcal{E}_b{}^k(\boldsymbol{r},\boldsymbol{r}_p) + LP[g_b{}^k(\boldsymbol{r},\boldsymbol{r}_p)] \tag{2.42}$$

i.e., the sum of the virtual background field $\mathcal{E}_b{}^k$ and a low pass filtered version of $g_b{}^k$, as numerically computed by means of a forward solver [84,87]. This represents the *distorted virtual experiment* (DVE) approximation [87]. By using (2.42), we can cast the linear equation for the contrast update:

$$\Delta\mathcal{E}_s{}^k(\boldsymbol{r}_o,\boldsymbol{r}_p) = \int_\Omega \mathcal{G}_b{}^k(\boldsymbol{r}_o,\boldsymbol{r}')\Delta\chi^k(\boldsymbol{r}')\mathcal{E}^k(\boldsymbol{r}',\boldsymbol{r}_p)d\boldsymbol{r}' = \mathcal{A}_e{}^k[\Delta\chi^k\mathcal{E}^k] \tag{2.43}$$

where $\Delta\mathcal{E}_s{}^k$ is the virtual anomalous field and $\mathcal{A}_e{}^k$ is the external radiation operator at k-th iteration, as computed in step ii).

After solving (2.43), a new reference profile is generated as $\chi^{k+1} = \chi^k + \Delta\chi^k$.

vi) *Return to step* ii). The iteration continues until the stopping criterion is fulfilled.

In step v), the updated solution χ^{k+1} can be evaluated after that the eq.(2.43) is solved. Notably, one still has to face an ill-posed (linear) inverse problem, which requires a regularization to obtain physically meaningful solutions. Inside the DIVE scheme, the TSVD regularization approach as well as the sparsity promoting scheme defined in eq.(2.44) have been considered. In particular, the k-th iteration of the CS based inversion scheme reads:

$$\min_{\Delta\chi^k}\left\{\left\|\boldsymbol{D_h}\boldsymbol{\chi^{k+1}}\right\|_{\ell_1} + \left\|\boldsymbol{D_v}\boldsymbol{\chi^{k+1}}\right\|_{\ell_1} + \left\|\boldsymbol{D_d}^{+}\boldsymbol{\chi^{k+1}}\right\|_{\ell_1} + \left\|\boldsymbol{D_d}^{-}\boldsymbol{\chi^{k+1}}\right\|_{\ell_1}\right\}$$
$$subject\ to \quad \left\|\boldsymbol{A^k}\boldsymbol{\Delta\chi^k} - \boldsymbol{\Delta\mathcal{E}_s{}^k}\right\|_{\ell_2} \leq \delta \tag{2.44}$$

wherein all the involved quantities are defined as in eq.(2.37).

Note that, at each DIVE iteration, the TSVD regularization only acts on the perturbation $\boldsymbol{\Delta\chi^k}$ as in eq.(2.36), whereas the sparsity promoting regularization in eq.(2.44) enforces sparsity on the whole contrast profile. This is expected to further improve the accuracy in the unknown profile reconstructions.

Results: numerical data

To get a better understanding of the DIVE scheme and performances, let us report a numerical example dealing with a 'kite' target shown in fig.2.9, whose leading dimension is 1λ (λ being the wavelength of the homogeneous background, assumed air). We refer to such an object since in [86] has been shown the incapability of the VELI approximation to effectively retrieve its electromagnetic properties, i.e., $\varepsilon_r = 2.2$ and $\sigma_r = 0.1$ S/m at 5 GHz. The target is positioned inside a square domain of side about 2λ and discretized into 42×42 cells, according to the Richmond's rule [108]. In order to collect in a non-redundant way as much information as possible [18], the synthetic

data are collected by assuming a multiview-multistatic illumination setup with 24 filamentary currents acting as primary sources and receivers. The antennas are evenly spaced on a circumference Γ surrounding the region Ω at a distance $r_o = 1.6\lambda$ from the origin of the reference system. The scattered field data are simulated by means of a full-wave forward solver based on the Method of Moments and a CG-FFT procedure, and it is corrupted with a random Gaussian noise with SNR=25dB to simulate measurement uncertainties.

To evaluate the accuracy of the retrieved contrast function, we use the normalized mean square error defined by $err = \|\chi - \tilde{\chi}\|^2 / \|\chi\|^2$, where χ is the actual contrast profile and $\tilde{\chi}$ the estimated one.

Initially, a TSVD based regularization is adopted. In fig.2.10(a), the support indicator (2.40) obtained in the *Initialization* step is shown. As it can be seen, the LSM is able to fairly identify the support of the target, thus allowing the selection of the pivot points and the design of the initial set of VE ($k = 1$). As expected, the VELI approximation, whose outcome is given in fig.2.10(b) and 2.10(c), fails in reconstructing the targets. Nevertheless, this partial unsatisfactory reconstruction is assumed as the new reference scenario and the pertaining forward scattering problem is solved. The VE are updated on the basis of the new indicator shown in fig.2.10(d), which allows to identify the support of the (geometrical and physical) variation $\Delta\chi^1$; then, the contrast profile in fig.2.10(e) and 2.10(e) can be achieved by adding $\Delta\chi^1$ to the previous reconstruction. As it can be seen, such a reconstruction is far from the ground truth and hence the iterative procedure continues since the stopping criterion is not fulfilled. By iterating the design of VE, DIVE progressively turns the initial reconstruction χ^1 into a reliable quantitative estimate as shown in fig.2.10(h) and 2.10(i), corresponding to a reconstruction error as low as 18%. This result requires eight iterations (with $N_T = 76, 91, 118, 126, 69, 108, 88$, respectively, chosen on the base of the guidelines given above).

For the sake of comparison, we have tried to reconstruct the electromagnetic properties of the 'kite' target by using the DBIM in conjunction with a TSVD regularization (see figs.2.10(j)-2.10(k)). In this case, the iterative scheme diverges, with a reconstruction error of 199%. Due to the large model error associated with the DBA, the Picard's plot cannot be exploited. Hence, we have heuristically set the truncation index N_T at the cutoff value of -15 dB below the relevant maximum singular value of the operator. Notably, this is in the order of the noise on the data.

The same analysis has been performed by using the CS inspired approach to carry out the inversion at each iteration of DIVE. From figs.2.11(a)-2.11(i) the evolution of

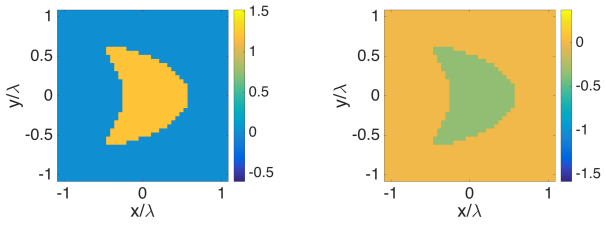

(a) (b)

Fig. 2.9. DIVE with numerical data: the 'kite' target. (a) Real and (b) imaginary part of the actual contrast profile.

the iterative reconstruction can be appreciated. In fig.2.11(h) and 2.11(i) the outcome of the DIVE scheme is shown; as it can be seen, the joint use of DIVE and the sparsity promoting approach provides a nearly optimal reconstruction, with a final reconstruction error as low as 3%. In this case, we have considered $\hat{\delta} = 0.75$ for the *Initialization* step, and $\hat{\delta} = 0.55$ for the following iterations. The power of the sparsity-promoting approach in giving multi-resolution images can be also observed in the retrieved contrast profile by means of the DBIM equipped with sparsity enhancement ($\hat{\delta} = 0.3$ for the *Initialization* step, while $\hat{\delta} = 0.6$ for the following iterations). As it can be seen from fig.2.11(j) and 2.11(k), the reconstruction is improved but the DIVE scheme is still outperforming the DBIM one, which achieves a final synthetic error as large as 76%.

More details on the number of iterations, *err* and *RRE* for each method are reported in Table 2.2.

Table 2.2. DIVE for 'kite' target: details of the inversion procedure for different analyzed approaches.

	err (k=0)	***err***	***RRE***	***# iterations***
DIVE-TSVD	0.89	0.18	0.005	8
DIVE-CS	0.76	0.03	0.003	7
DBIM-TSVD	1.00	1.99	0.194	3
DBIM-CS	0.94	0.76	0.109	4

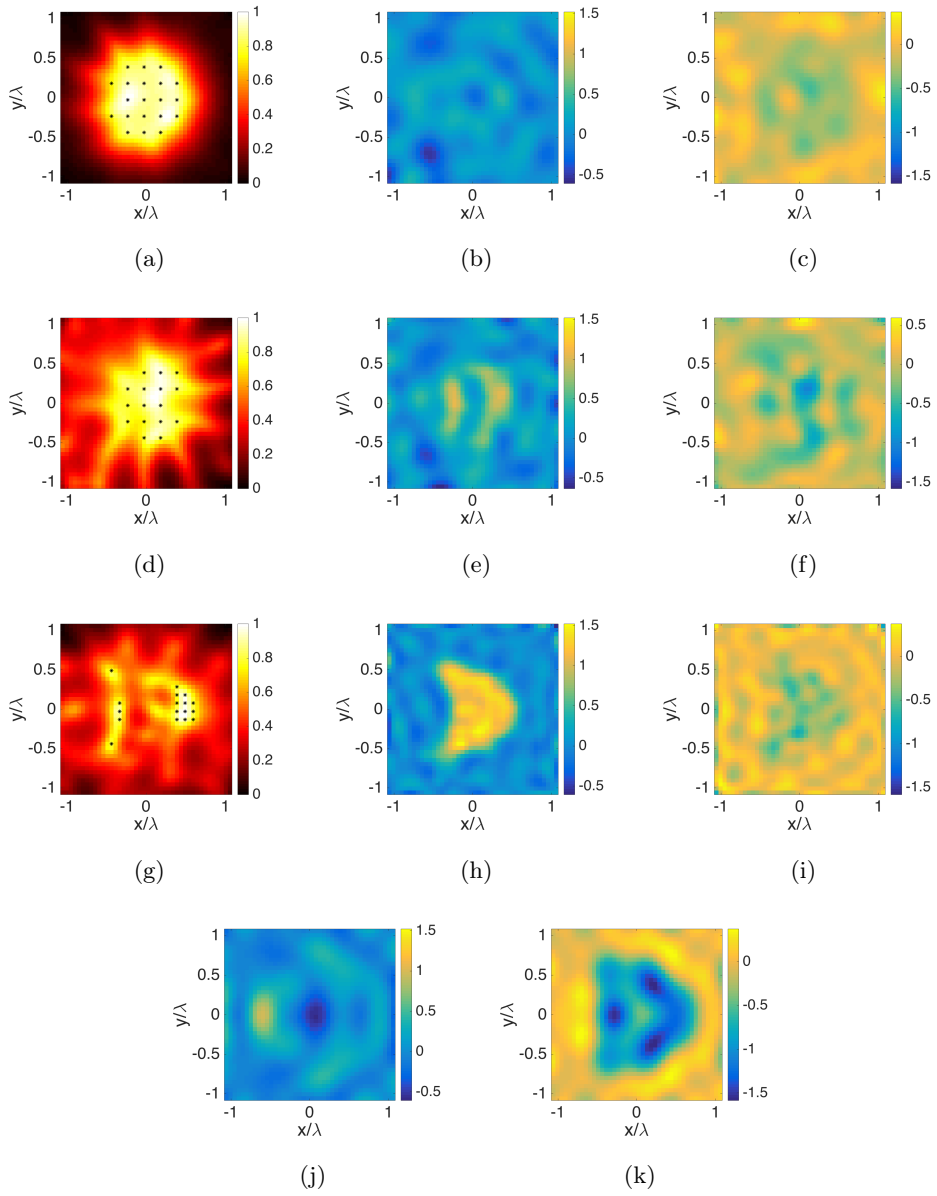

Fig. 2.10. DIVE with numerical data: TSVD regularization. (a) Normalized LSM indicator for the *Initialization* step with superimposed the pivot points marked as stars. (b) Real and (c) imaginary part of the obtained starting guess. (d) Normalized LSM indicator and pivot points for the first step of the iterative procedure ($k = 1$); (e) real and (f) imaginary part of the corresponding retrieved contrast profile at $k = 1$. (g) Normalized LSM indicator and pivot points for the last step of DIVE-TSVD scheme ($k = 8$); (h) real and (i) imaginary part of the final retrieved contrast function. (j) Real and (k) imaginary part of the final retrieved contrast profile by means of DBIM-TSVD after $k = 3$ iterations.

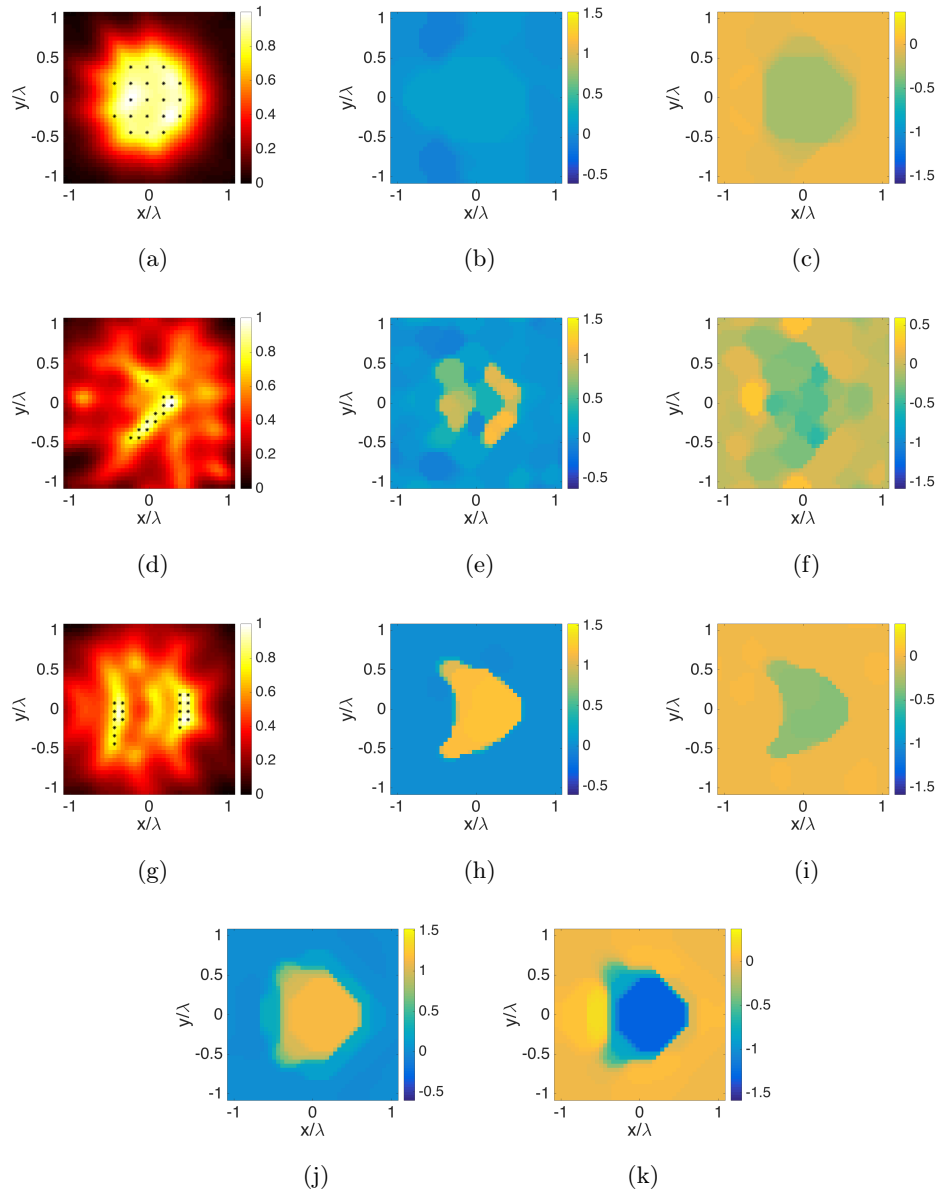

Fig. 2.11. DIVE with numerical data: sparsity promoting regularization. (a) Normalized LSM indicator for the *Initialization* step with superimposed the pivot points marked as stars. (b) Real and (c) imaginary part of the obtained starting guess but with a sparsity promoting scheme. (d) Normalized LSM indicator and pivot points for the first step of the iterative procedure ($k = 1$); (e) real and (f) imaginary part of the corresponding retrieved contrast profile at $k = 1$. (g) Normalized LSM indicator and pivot points for the last step of DIVE-CS scheme ($k = 7$); (h) real and (i) imaginary part of the final retrieved contrast function. (j) Real and (k) imaginary part of the final retrieved contrast profile by means of DBIM with a sparsity promoting scheme and after $k = 4$ iterations.

Results: experimental data

In this section, we have considered three targets from the Fresnel database: the *FoamDielIntTM* and the *FoamTwinDielIntTM* [106] described in Sec.2.4.2, and the *TwinDielTM* which consists of two identical dielectric cylinders of radius 1.5 cm and relative permittivity 3 ± 0.3 [110].

It is worth noting that all the reconstructions have been obtained using single frequency data. Besides being different from what is usually done in the literature (see [54, 57, 111]), it is important to remark that the chosen frequency is such that the targets cannot be assumed to be "weak". In addition, no a priori information on the admissible values of permittivity and conductivity is enforced through regularization, neither explicit support information provided by eq.(2.40). Finally, to appraise the robustness of DIVE equipped with the sparsity promoting scheme, we have also carried out an analysis when decreasing the number of data exploited in the quantitative inversion procedure. In particular, the reduction affects both the number of transmitting and receiving antennas. The dimension of the processed data matrix is referred to as Z in Tables 2.3-2.5.

For the *TwinDielTM* target, the working frequency is 6 GHz, and the investigated area (0.15×0.15 m^2 large) is discretized into 64×64 cells. The results reported in fig.2.12 have been achieved with $Z = 72 \times 36$. The outcome of the DIVE-TSVD approach is shown in fig.2.12(b) and 2.12(c). As it can be seen, the method is able to retrieve the two cylinders. Nevertheless, the reconstruction with DIVE-CS (see fig. 2.12(d) and 2.12(e)) is remarkably better, in terms of both electromagnetic properties and scatterers' shapes. Even when reducing experiments and data, using a 36×18 multiview-multistatic data matrix, the results are fully satisfactory, see fig.2.12(f) and 2.12(g). For more details on the number of iterations and RRE relative to each method, please see Table 2.3.

Table 2.3. DIVE for Fresnel *TwinDielTM* target: details of the inversion procedure

	RRE	***# iterations***
DIVE-TSVD, $\boldsymbol{Z = 72 \times 36}$	0.06753	12
DIVE-CS, $\boldsymbol{Z = 72 \times 36}$	0.06826	5
DIVE-CS, $\boldsymbol{Z = 36 \times 18}$	0.05374	7

For the *FoamTwinDielIntTM* target, the results are reported in fig. 2.13 and Table 2.4, respectively. The working frequency is 4 GHz and the side of the investigated area is 0.175×0.175 m^2, while the discretization grid is 78×78. The sizes of the exploited

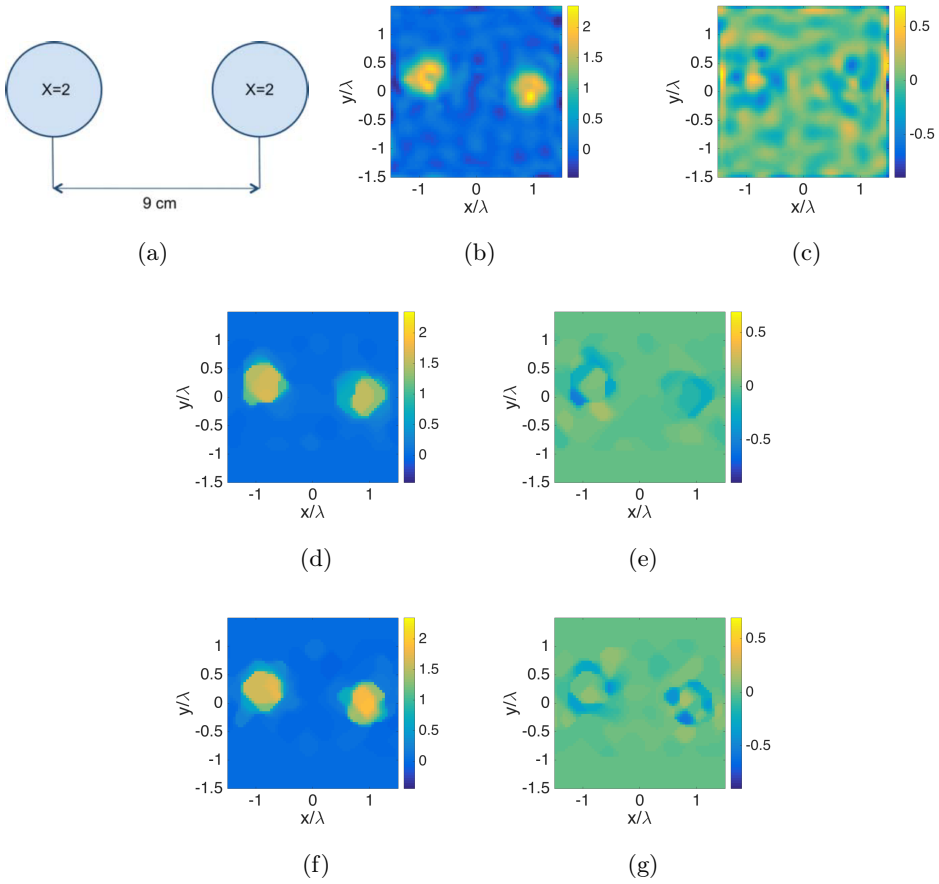

Fig. 2.12. DIVE with experimental data: Fresnel *TwinDielTM* target at 6 GHz. (a) Reference profile. (b) Real and (c) imaginary part of the retrieved contrast function with DIVE-TSVD (during the iterative procedure $N_T = [117, 90, 148, 106, 91, 126, 115, 154, 122, 131, 142]$, for the initial guess $N_T = 140$); (d)-(e) are the same of (b)-(c) but for DIVE with sparsity promoting regularization; (f)-(g) are the same of (d)-(e) but for a reduced number of processed data (see Table 2.3).

multiview-multistatic data matrices are 45×18 and 23×18, respectively. Again, DIVE-CS gives back a more accurate reconstruction in terms of both shape and electromagnetic properties of the target (figs.2.13(d)-2.13(g)) with respect to DIVE-TSVD (fig.2.13(b) and 2.13(c)).

It is worth noting that, at the considered frequency of 4 GHz, the separation between the two higher permittivity cylinders is 2 cm, that is, 0.267 in terms of the wavelength in the background medium. Hence, DIVE is able to resolve targets well below the half-wavelength Rayleigh limit. Actually, the separation is just slighlty larger than a quarter of the wavelength, i.e., the resolution limit for BA, when using full aperture (multiview multistatic) data.

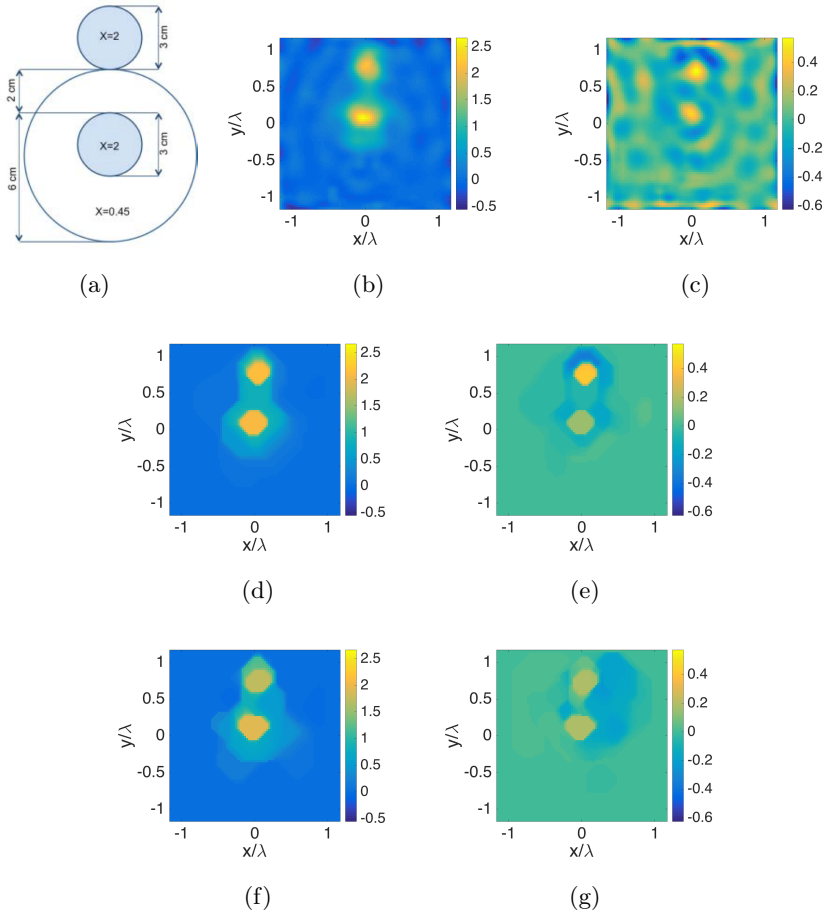

Fig. 2.13. DIVE with experimental data: Fresnel *FoamTwinDielIntTM* target at 4 GHz. (a) Reference profile. (b) Real and (c) imaginary part of the retrieved contrast function with DIVE-TSVD (during the iterative procedure $N_T = [86, 73, 96, 72, 50, 74, 34, 67, 68, 83, 69, 48, 68, 91, 79, 89]$, for the initial guess $N_T = 86$); (d)-(e) are the same of (b)-(c) but for DIVE with sparsity promoting regularization; (f)-(g) are the same of (d)-(e) but for a reduced number of processed data (see Table 2.4).

Table 2.4. DIVE for Fresnel *FoamTwinDielIntTM* target: details of the inversion procedure

	RRE	***# iterations***
DIVE-TSVD, $Z = 45 \times 18$	0.01669	17
DIVE-CS, $Z = 45 \times 18$	0.01419	7
DIVE-CS, $Z = 23 \times 18$	0.09123	6

Finally, for the *FoamDielIntTM* target, we have considered the data at 4 GHz and an investigated domain of 0.125×0.125 m^2 discretized into 78×78 cells. The results are reported in fig.2.14 and have been achieved with 23×18 and 9×9 multiview-multistatic data matrices. DIVE-TSVD results are shown in fig.2.14(b) and 2.14(c), while DIVE-CS ones in figs.2.14(d)-2.14(g). As it can be seen, even in this case, the

improvements provided by the CS tool are clear, as indeed DIVE-CS is able to provide a nearly optimal reconstruction of the nominal electromagnetic properties of both the two nested cylinders. More details on the number of iterations, and the final value of RRE, are given in Table 2.5.

Note that in processing these data, we have used the same values of the regularization parameter of the simulated data, except for the cases of unsampled data matrices for witch we have used $\hat{\delta} = 0.40$, since a higher level of accuracy can be required.

Finally, in all the cases, the iterative procedure stops because of the fulfillment of the convergence criterion in terms of RRE. For the sake of brevity, the *unsuccessful* inversions obtained with DBIM in the same conditions have not been reported.

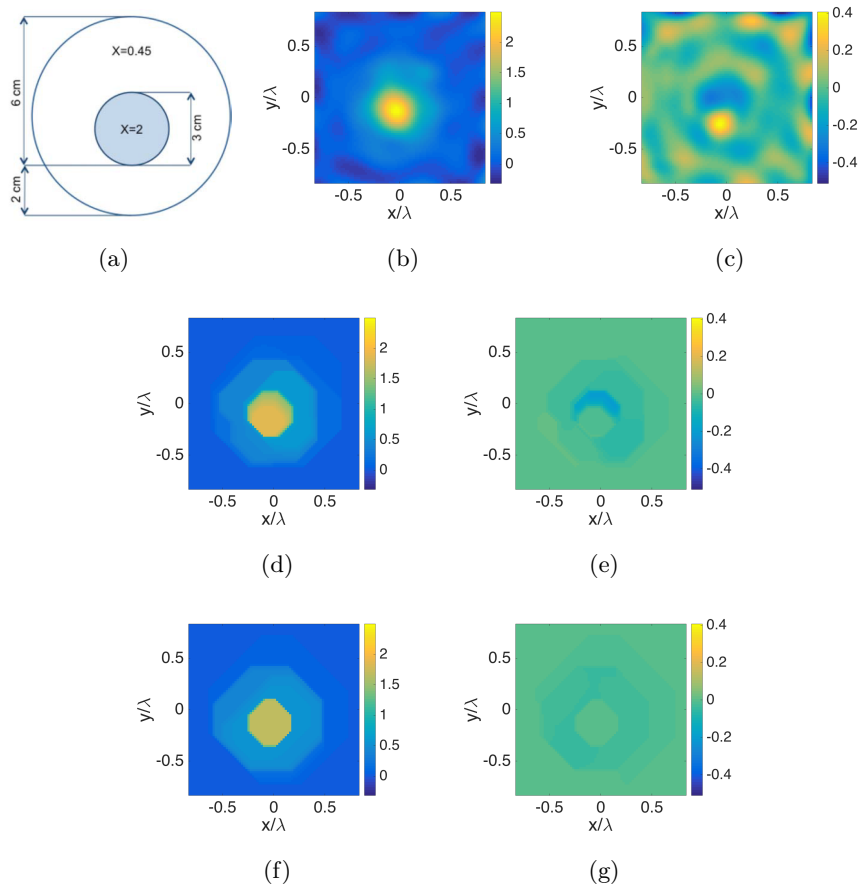

Fig. 2.14. DIVE with experimental data: Fresnel *FoamDielIntTM* target at 4 GHz. (a) Reference profile. (b) Real and (c) imaginary part of the retrieved contrast function with DIVE-TSVD (during the iterative procedure $N_T = [55, 36, 51, 40, 47, 35, 46, 51, 55]$, for the initial guess $N_T = 47$); (d)-(e) are the same of (b)-(c) but for DIVE with sparsity promoting regularization; (f)-(g) are the same of (d)-(e) but for a reduced number of processed data (see Table 2.5).

Table 2.5. DIVE for Fresnel *FoamDielIntTM* target: details of the inversion procedure

	RRE	***# iterations***
DIVE-TSVD, $\boldsymbol{Z = 23 \times 18}$	0.0182	10
DIVE-CS, $\boldsymbol{Z = 23 \times 18}$	0.0188	5
DIVE-CS, $\boldsymbol{Z = 9 \times 9}$	0.0354	6

2.5 A representation for non-radiating sources

As is well known, the so-called *non radiating* (NR) *source* are non trivial sources compactly supported in a given domain and that have the interesting (and surprising) property that they generate fields that vanish identically outside the source region [24,82]. In an inverse scattering problem, such an amazing property of the NR sources is closely related to questions concerning the uniqueness and ill-posedness.

The subject of NR sources distribution has been studied for many years and particular interest has been devoted to define the field that they generate within the region they occupy [24, 112]. In design problems, non radiating sources are of interest for at least three different reasons. In fact, in antenna synthesis the addition of a NR source to an already synthesized distribution may considerably simplify the realization of the actual antenna. Also, the synthesis of invisibility devices could be interestingly dealt with by looking (for each situation of interest) for contrast sources such to be non radiating [113–117]. Last, but not least, note that in any inverse scattering problem the NR part of the contrast source is the actual unknown part, as the radiating part can be eventually determined[2] from the data equation. Hence, a general representation of NR sources is of interest.

As demonstrated by Devaney and Wolf [24], a NR source can be easily constructed by solving the following relation:

$$W_{NR}(\boldsymbol{r}, \omega) = [\nabla^2 + k_b^2] f(\boldsymbol{r}, \omega) \tag{2.45}$$

namely, by applying the Helmholtz operator (i.e., the term in square brackets) to a function $f(\boldsymbol{r}, \omega)$ that is compactly supported in the spatial volume Ω bounded by a closed surface Σ at any given frequency ω and possesses continuous partial spatial derivatives throughout this volume but is otherwise arbitrary.
The above assumptions of f imply that:

[2] but for the "poorly radiating" part corresponding to the smaller singular values of $\mathcal{A}_e$.

$$\begin{cases} f(\boldsymbol{r},\omega)\big|_{\boldsymbol{r}\in\Sigma} = 0 \\ \frac{\partial f(\boldsymbol{r},\omega)}{\partial n}\Big|_{\boldsymbol{r}\in\Sigma} = 0 \end{cases} \tag{2.46}$$

where $\partial/\partial n$ denote differentiation along outward normal to Ω.

Then, the simple idea pursued in the following is to exploit the definition (2.45) to get a representation and eventually design NR currents. To this aim, let consider the 2D scenario depicted in fig.2.15 in which the spatial volume is a square domain $2a \times 2b$ large, with $a = b$.

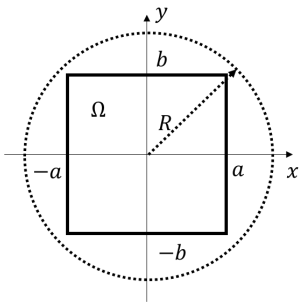

Fig. 2.15. 2D scenario for non-radiating currents.

A possible definition for the function $f[(\boldsymbol{r} = x, y)]$ could read:

$$f(x,y) = \sum_{n=-\infty}^{+\infty} \sum_{m=-\infty}^{+\infty} a_{nm}\, e^{j\left(\frac{n\pi}{a}x + \frac{m\pi}{b}y\right)} \tag{2.47}$$

so that it possesses continuous partial spatial derivatives. Accordingly, constraints (2.46) particularize as:

$$\begin{cases} f(x=a,y) = f(x=-a,y) = 0 \\ f(x,y=b) = f(x,y=-b) = 0 \\ f'(x=a,y) = f'(x=-a,y) = 0 \\ f'(x,y=b) = f'(x,y=-b) = 0 \end{cases} \tag{2.48}$$

in which the superscript $'$ indicates the first derivative.

By substituting the function f as defined in (2.47) into the equation (2.45) and by applying the Helmholtz operator (see Appendix B for the extended calculations), the following expression for W_{NR} is achieved:

$$\begin{aligned} W_{NR}(x,y) = \sum_{n=-\infty}^{+\infty} \sum_{m=-\infty}^{+\infty} \left[k_b^2 - \pi^2\left(\frac{n^2}{a^2} + \frac{m^2}{b^2}\right)\right] a_{nm}\, e^{j\left(n\frac{\pi}{a}x + m\frac{\pi}{b}y\right)} \\ = \sum_{n=-\infty}^{+\infty} \sum_{m=-\infty}^{+\infty} c_{nm}\, e^{j\left(n\frac{\pi}{a}x + m\frac{\pi}{b}y\right)} \end{aligned} \tag{2.49}$$

where:

$$c_{nm} = a_{nm}\left[k_b^2 - \pi^2\left(\frac{n^2}{a^2} + \frac{m^2}{b^2}\right)\right] \tag{2.50}$$

By following the math in Appendix B, constraints (2.48) turn as follow:

$$\begin{cases} \sum_{n=-\infty}^{+\infty} \frac{c_{nm}(-1)^n}{k_b^2 - \pi^2\left(\frac{n^2}{a^2}+\frac{m^2}{b^2}\right)} = 0 & \forall m \\ \sum_{m=-\infty}^{+\infty} \frac{c_{nm}(-1)^m}{k_b^2 - \pi^2\left(\frac{n^2}{a^2}+\frac{m^2}{b^2}\right)} = 0 & \forall n \\ \sum_{n=-\infty}^{+\infty} \frac{n\ c_{nm}(-1)^n}{k_b^2 - \pi^2\left(\frac{n^2}{a^2}+\frac{m^2}{b^2}\right)} = 0 & \forall m \\ \sum_{m=-\infty}^{+\infty} \frac{m\ c_{nm}(-1)^m}{k_b^2 - \pi^2\left(\frac{n^2}{a^2}+\frac{m^2}{b^2}\right)} = 0 & \forall n \end{cases} \tag{2.51}$$

Then, expression (2.49) subject to constraints (2.51) is a possible representation for (a class of) NR sources. Notably, any current obeying to (2.49) and (2.51) is NR, but the reverse is not true, so that some NR sources could exist which cannot be represented in such a way [118].

As an example of usefulness, and a test of numerical effectiveness (i.e., robustness to numerical approximations) we have considered a region Ω $2.6\lambda \times 2.6\lambda$ large and discretized into 52×52 square cells. Moreover, the involved summations have been truncated by setting the total number of coefficients equal to 2601, so that they are of a similar order of the number of cells.

In fig.2.16(a) some coefficients c_{nm} obeying (2.51) are depicted. They have been obtained as the outcome of the Matlab® optimization toolbox by considering equations (2.51) as constraints of an "optimization" problem without any objective function. The effectiveness of the representation is proved by plotting the field radiated by the synthesized W_{NR} current on 24 points located all around Ω at distance of about 2λ. In particular, in fig. 2.16(b) it is shown a comparison with the field radiated by the purely radiating current defined by a properly weighted Bessel function $J_0(k_b\boldsymbol{r})$[3]. As it can be seen, the field radiated from W_{NR} is five orders of magnitude smaller than the field radiated from J_0, and smaller and smaller fields can be obtained by using a denser grid.

2.5.1 A possible physical interpretation

In the 2D TM scalar problem dealt with in this thesis, the z-component of the total electric field fulfills the following equation:

$$\nabla^2 E_z + k_b^2 E_z = j\omega\mu W_z \tag{2.52}$$

[3] Note that the sources are scaled in such a way that they have the same energy.

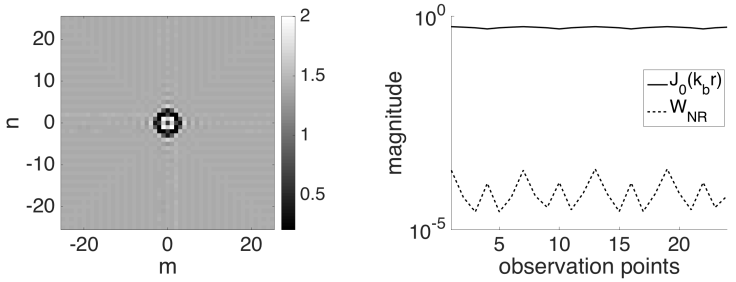

(a) (b)

Fig. 2.16. Design of non radiating sources. (a) Synthesized coefficients and (b) comparison of the radiated field by the purely radiating Bessel function (continuous line) and the synthesized NR source (dashed line).

since $E_z = -j\omega A_z$ in the scalar case, A_z being the z-component of the vector potential associated to the source.
By comparing eq.(2.52) with eq.(2.45), the auxiliary function f we have used can be interpreted as the total electric field E_z (but for an unessential constant).

Therefore, one can apply the equivalence theorem on a surface Σ embedding Ω and the equivalent magnetic and electric sources can be respectively defined as:

$$\underline{W}_{ms} = -i_n \times \underline{E} \tag{2.53}$$

$$\underline{W}_{s} = i_n \times \underline{H} \tag{2.54}$$

wherein i_n is the normal vector to Σ, while $\underline{E}$ and $\underline{H}$ are the vector electric and magnetic field, respectively.

One of the possibility to have null field outside Ω is that both $\underline{W}_{ms}$ and $\underline{W}_{s}$ are equal to zero. Let us consider for the sake of simplicity the edge of Σ at $x = a$ (the same arguments will hold for the others edges). Accordingly:

$$\underline{W}_{ms} = -i_x \times E_z i_z = E_z i_y \tag{2.55}$$

$$\underline{W}_{s} = i_x \times (H_x i_x + H_y i_y) = H_y i_z = -\frac{\partial E_z}{\partial x} = -\frac{\partial E_z}{\partial n} \tag{2.56}$$

so that, the conditions $\underline{W}_{ms} = 0$ and $\underline{W}_{s} = 0$ imply:

$$\begin{cases} E_z(\boldsymbol{r})|_{\boldsymbol{r}\in\Sigma} = 0 \\ \left.\frac{\partial E_z(\boldsymbol{r})}{\partial n}\right|_{\boldsymbol{r}\in\Sigma} = 0 \end{cases} \tag{2.57}$$

that are exactly the same conditions in eq.(2.46).

Unfortunately, as pointed out in [118], conditions $\underline{W}_{ms} = 0$ and $\underline{W}_{s} = 0$ are not the unique conditions for defining non radiating equivalent currents, so that representation (2.49) subject to conditions (2.51) does not cover the representation of all

possible non radiating sources. A more general (complete) representation would be obtained by using representation (2.47) for $f = E_z$ and using condition (10b) of [118]. Unfortunately, this latter appears to be difficult to be practically implemented/applied.

2.6 Concluding remarks

The content of this Chapter deals with contributions to both electromagnetic theory and the solution of inverse scattering problems. As far as the theoretical part is concerned, a spectral analysis of the information content of the data (i.e., the scattered field) in an inverse scattering problem has been proposed for different approximated models. As a matter of fact, the spectral content of such a scattered field is bounded and a relation for the unknown object of the problem to be detected (or 'undetected', see the remainder of the thesis) has been derived for the CS-EB and the SPF approximations. As a further theoretical contribution, a novel representation for non radiating sources has been given, which is useful for a simpler realization of antennas, or for imaging problems, or for invisibility problems.

Regarding the solution of the inverse scattering problems, two novel strategies have been proposed that derive from the new framework of the 'virtual experiments' (VE) and the pertaining linear approximation. In particular, the *distorted virtual experiment* (DVE) strategy is devoted to retrieve the electromagnetic properties of anomalies embedded in a non-homogeneous scenario, while the *distorted iterated virtual experiment* (DIVE) approach aims at enlarging the range of validity of the VE-based linear approximation by iteratively solving a differential problem by means of DVE. The two inversion schemes have been validated with both numerical and experimental data provided by the Institute Fresnel of Marseille.

The developed theories and procedures, as well as all more traditional results and tools in inverse scattering, can be effectively exploited in the synthesis and design of innovative devices, which is the subject of the remainder of the thesis.

3

SYNTHESIS OF VARIABLE MULTI-PURPOSE DIELECTRIC PROFILE ANTENNAS

3.1 Introduction

A class of dielectric lenses qualify as GRadient refractive INdex (GRIN) devices. As is well known, GRIN media allow to control the electromagnetic field path, so the design of this kind of devices is of interest in very many practical instances.

Classical well known GRIN devices are the Luneburg lens [119, 120] and the Maxwell fish-eye lens [121]. The Luneburg lens allows to transform the point source radiation into a plane wave; vice versa, each point on the surface of an ideal Luneburg lens is the focal point for parallel radiation incident on the opposite side. Differently, in the Maxwell fish-eye lens if a point is located at the rim of the spherical surface, the lens will focus the ray to the opposite point on the same surface.

From a practical point of view, the realization of a GRIN lens with a generic gradient index profile poses difficult fabrication challenges. Hence, the above described lenses are normally layered structures of discrete concentric shells, each of them having a different refractive index, thus leading to a stepped-index lenses [122–124]. As it can be easily guessed, such a strategy results in a tradeoff between the number of shells and the achieved performances. As a matter of fact, a huge amount of work has been done in literature in the synthesis of GRIN devices by exploiting several methodologies and theoretical arguments, ranging from metamaterials (MTM) and metasurfaces (MTS), by exploiting Transformation Optics (TO) [125].

The Luneburg lens and the Maxwell fish-eye lens are elegant solutions of the Maxwell equations, but they are of course unable to realize a different given behavior of the electromagnetic field. To overcome this limit, MTS and TO have been exploited to develop non-canonical solutions, leading to conductors and dielectrics based solutions, respectively [126–133].

Unfortunately, the bi-anisotropic materials generally obtained by TO are so complicated that cannot be easily realized. So, in order to use the potential of TO for

practical design of devices, it is important to relax the exact required parameters of the material leading to an unavoidable deterioration of the performances of the device.

As already argued, an effective alternative is represented by inverse scattering, which provides an interesting framework for the synthesis of dielectric profile antennas [104, 134, 135], as well as of other devices [136, 137]. In fact, it represents a general methodology which allows to control the electromagnetic waves behavior in order to obtain generic far field specifications. In fact, in an inverse scattering problem the aim is to retrieve location, shape and electromagnetic properties of an unknown object starting from the knowledge of the incident field and the measurements of the arising scattered or total field. Then, if a specific behavior of the total field is considered as available data of the problem (rather than the measured total field), the diagnosis problem can be turned into a synthesis one [104, 134, 135].

On the other side, a number of issues have to be fixed in order to exploit inverse scattering as a design tool. As a first question, it is readily noted that for a target total field the resulting dielectric profile will be a function of the amplitude of the primary source. Second, the actual feasibility of the resulting profile will depend on questions such as symmetry, number of different materials involved, and actual physical feasibility[1] of this latter. These issues and possible way to conveniently tackle them (as well as demonstration of the usefulness of the developed tools) will be the subject of the remainder of this Chapter.

3.2 A new formulation of the Contrast Source Inversion (CSI) method: determining the amplitude of the primary sources

Let us recall the compact formulation of the data and state equations governing the inverse scattering phenomenon:

$$E_s(\boldsymbol{r}_o, \boldsymbol{r}_t) = \mathcal{A}_e[W(\boldsymbol{r}, \boldsymbol{r}_t)], \quad \boldsymbol{r} \in \Omega, \boldsymbol{r}_o \in \Gamma_o, \boldsymbol{r}_t \in \Gamma_t \tag{3.1}$$

$$W(\boldsymbol{r}, \boldsymbol{r}_t) = \chi(\boldsymbol{r}) E_i(\boldsymbol{r}, \boldsymbol{r}_t) + \chi(\boldsymbol{r}) \mathcal{A}_i[W(\boldsymbol{r}, \boldsymbol{r}_t)], \quad \boldsymbol{r} \in \Omega, \boldsymbol{r}_t \in \Gamma_t \tag{3.2}$$

in which $\mathcal{A}_e$ and $\mathcal{A}_i$ are a short notation for the radiation operators, whose explicit expressions are given in (1.3) and (1.2). Note that, differently from (1.3) and (1.2), two distinct surfaces are considered for the transmitting (Γ_t) and detecting (Γ_o) antennas, in order to have an increased flexibility for the tools which follow.

[1] By "physically feasible" statement, permittivity values larger than 1 and conductivity values larger than 0 are meant.

As is well known, the inverse scattering problem is non linear since both the contrast function $\chi(\boldsymbol{r})$ and the contrast source $W(\boldsymbol{r}, \boldsymbol{r}_t)$ are unknowns [1–3]. In order to face with such a difficulty, several efforts have been carried out in the literature to develop effective solution methods [19, 20, 34, 138, 139]. The *contrast source inversion* (CSI) method [20, 138] is one of the most popular and effective inversion schemes which allows to face the inverse scattering problem in its full non-linearity, while dealing with a mathematical problem involving just linear and quadratic equations. In particular, it simultaneously looks for both the contrast χ and the contrast source W, and the solution is iteratively built by minimizing a cost functional which takes into account the data-to-unknown relationship and the state equation [19, 20, 34, 138]. The mathematical formulation of the CSI method is reported in Appendix C.

When a synthesis problem is considered instead of a diagnosis one, the aim of the inverse scattering problem becomes the design of a device able to realize given fields. In particular, one wants to determine $\chi(\boldsymbol{r})$ (i.e., the electromagnetic properties of the Ω region) starting from the knowledge of the incident field and obeying given specifications on the total field on Γ_o. Let us note explicitly that design constraints are in terms of the total fields, which is slightly different from more usual inverse scattering problems (where equations are usually written in terms of the scattered field). Obviously, one can easily go from one formulation to another by simply subtracting or adding the incident fields.

It is also worth to note that for a given total field on the observation domain Γ_o, different amplitudes of the incident fields give rise to different requirements on the scattered fields (and hence to different profiles). For this reason, it proves convenient to modify the standard CSI algorithm by considering one more set of complex unknowns $\tau^{(v)}$ modulating the amplitudes of the primary sources. In fact, the exploitation of these additional degrees of freedom will allow for a better matching of the desired fields, and/or to simpler contrast profiles. Then, it is convenient to distinguish among a 'basic' incident field $\widehat{E}_i^{(v)}$ (corresponding to unitary excitation) and an 'actual' incident field $E_i^{(v)}$ (corresponding to the synthesized excitations of the primary sources times the corresponding $\widehat{E}_i^{(v)}$).

From the above, we recast the CSI functional as follow:

$$\begin{aligned}\Phi(W,\chi,\tau) = &\sum_{v=1}^{T} \frac{\left\| \mathcal{A}_e\left[W^{(v)}\right] - E^{(v)} + \tau^{(v)}\widehat{E}_i^{(v)} \right\|_2^2}{\left\| E^{(v)} \right\|_2^2} \\ &+ \sum_{v=1}^{T} \frac{\left\| \chi\mathcal{A}_i\left[W^{(v)}\right] + \chi\tau^{(v)}\widehat{E}_i^{(v)} - W^{(v)} \right\|_2^2}{\left\| \widehat{E}_i^{(v)} \right\|_2^2}\end{aligned} \tag{3.3}$$

where $\|\cdot\|_2$ is the ℓ_2-norm and T is the number of different incident fields. Note that we have written the scattered field as $E_s(\boldsymbol{r}_o, \boldsymbol{r}_t) = E(\boldsymbol{r}_o, \boldsymbol{r}_t) - \tau \widehat{E}_i(\boldsymbol{r}_o, \boldsymbol{r}_t)$, $E(\boldsymbol{r}_o, \boldsymbol{r}_t)$ being in this case the assigned total field on Γ_o, i.e., our design constraint.
As it can be seen, the normalization herein considered for the first addendum is not the same as in functional (C.1). In fact, the total field is considered rather than the scattered field, since this latter would change its value at each iteration due to the rescaling of the incident field by $\tau^{(v)}$.

The solution of the inverse scattering design problem can still be solved by minimizing the cost functional (3.3) and by adopting the procedure developed in [34]. In particular, the minimization is pursued by means of a conjugate gradient algorithm in which, at each step, the values of χ, $W^{(v)}$ and $\tau^{(v)}$ are updated according to a procedure of the kind:

$$\begin{bmatrix} \chi_{k+1} \\ W_{k+1} \\ \tau_{k+1} \end{bmatrix} = \begin{bmatrix} \chi_k \\ W_k \\ \tau_k \end{bmatrix} + \lambda_k \mathcal{H}_k \begin{bmatrix} \nabla\chi_k \\ \nabla W_k \\ \nabla\tau_k \end{bmatrix} \tag{3.4}$$

in which, k and $(k+1)$ indicate the k-th and $(k+1)$-th iteration, respectively, $\nabla\chi$, ∇W and $\nabla\tau$ are the gradients of the functional Φ with respect to χ, W and τ, while λ_k is a scalar parameter that has to be evaluated at each iteration in order to guarantee the maximum decrease of the functional along the direction given by $\mathcal{H}\nabla\Phi$ ($\mathcal{H}$ being a dyadic obeying the Polak-Ribiere scheme) [34].

Obviously, the gradient of the functional and the coefficients of the fourth order polynomial in the variable λ_k involved in the line minimization step are properly modified with respect to [34]. Their expression can be found in Appendix D.

3.3 Further modifications: enforcing desired properties on the unknown profile

As previously discussed, the intrinsic non linearity of the inverse scattering problem makes it difficult to develop reliable algorithms. Since (3.3) is a non quadratic functional of the unknowns and may depend on thousands of variables, the problem arises on how to find its global minimum avoiding globally minimization schemes or approximations. In fact, a gradient-based minimization scheme could be trapped into local minima, which are false solutions of the problem.

In [34] has been shown that the functional (C.1) involved into the standard CSI has a polynomial nature and such a circumstance led in [19] to infer some general rules affecting occurrence of local minima. As gathered by Isernia and co-workers [19], *a*

priori information can play a crucial role in reducing the number of unknowns and simplify the solution of the problem. In particular, such a priori knowledge can be exploited as deterministic constraints by adding a suitable penalty term Φ_p to the cost functional, in such a way that all local minima of (3.3) not satisfying Φ_p disappear in the penalized functional:

$$\Phi' = \Phi + w_p \Phi_p \tag{3.5}$$

where w_p is a positive weighting coefficient that (provided it is sufficiently large) enforces the minimization to evolve inside or close to the set implicitly defined from the meant constraints. Hence, Φ_p is a regularization function and w_p is the regularization parameter. Notably, the choice of the parameter w_p plays a key role, since it determines the relative weight of the regularization term with respect to the other terms of the cost functional. As usual, if it is too small, the enforced behavior does not come to light, whereas a too large value entails that less importance is given to the fitting of the data with respect to the behavior enforcement.

The interest of these arguments and tools for the present design problem is readily understood: if the penalizing term is a functional of the unknown χ, it allows to enforce some desired behavior on the contrast profile.

A first useful requirement could be enforcing lossless and physical feasibility properties of the contrast function. To this aim, the pertaining additional term can be given as:

$$\Phi_p = \Phi_f(\chi) = \|\chi - f(\chi)\|_2^2 \tag{3.6}$$

where $f(\chi)$ is the projection of χ into the set of admissible functions (for example, the set of real and positive functions). Note that this latter condition could allow to avoid metamaterials in the design of microwave devices since the adoption of natural (or better, bulk) materials can allow an easier manufacturing of the device.

A second possible requirement on χ could be enforcing a circular symmetry. In this case, the additive penalty term would read:

$$\Phi_p = \Phi_s(\chi) = \left\| \frac{\partial \chi}{\partial \theta} \right\|_2^2 \tag{3.7}$$

in which θ is the angular coordinate of the polar reference system. Notably, minimization of Φ_s allows to minimize the angular variation of the contrast function around the center of the coordinate system.

Additionally, in some circumstances a gently varying profile can be useful, so that a suitable penalty term is:

$$\Phi_p = \Phi_{\rho_2}(\chi) = \left\| \frac{\partial \chi}{\partial \rho} \right\|_2^2 \tag{3.8}$$

wherein ρ is the radial coordinate of the polar reference system and such a ℓ_2-minimization enforces a smooth variation of χ along the radial coordinate.

It is worth to note that the optimization of (3.5) within a conjugate gradient scheme requires the computation of the gradients of the different addenda. Their expressions as well as the coefficients occurring in the line minimizations are reported in Appendix D.

3.3.1 Exploiting inverse scattering and Compressive Sensing for design problems

The CS theory provides many useful tools for solving, in an accurate fashion, linear problems when the unknown signal is known to be S-sparse (i.e., it has S non-zeros coefficients, whose location is unknown, of a proper basis). Also, CS is of the outmost interest in design problems, as "sparsest" solution may correspond to the most effective (or cheapest) solution to a given problem. However, as already stressed, the inverse scattering problem is non linear and hence the exploitation of CS methodologies is not straightforward. This notwithstanding, in [77] some smart strategies have been proposed to extend the applicability of CS to CSI scheme.

By paralleling the previous Section, it is possible to refer to the ℓ_1-norm penalized CSI developed in [77] in order to enforce some other desired behavior on the contrast function. For instance, in case of circularly symmetric profiles, an interesting chance for simplified manufacturing is the use of a reduced number of different materials. From a mathematical point of view, such a circumstance leads to define a proper basis in which the unknown χ is expected to be *sparse*. As a matter of fact, by considering the ℓ_1-minimization of the radial derivative of χ (with respect to the center of the region of interest), the arising function will be *sparse* in the space of radial step functions. Hence, the penalty term reads [77, 135]:

$$\Phi_p = \Phi_{\rho_1}(\chi) = \left\| \frac{\partial \chi}{\partial \rho} \right\|_1 \tag{3.9}$$

in which $\|\cdot\|_1$ is the ℓ_1-norm, ρ is the radial coordinate of the polar reference system, while the minimization of the ℓ_1-norm of the radial derivative of χ both enforces a piece-wise constant behavior on the contrast profile and guarantees the minimal number of hops. Therefore, a stepped-index profile is (in principle) achieved.

As far as the modification of the gradient of the functional for the pertaining penalty term is concerned, it is worth to note that due to the presence of the ℓ_1-norm, the functional (3.9) is non-differentiable when its argument is equal to zero. This drawback has been overcome in [77] by considering the sub-gradients technique [140, 141]. The arising expressions can be found in Appendix D as well.

3.3.2 On the choice of the weighting parameters

Some consideration on the choice of the weighting parameters is needed. As a matter of fact, in a synthesis problem, location and shape of the device are fixed design parameters (only the electromagnetic properties are unknown) and hence one can take advantage from these a priori information to define w_p. In particular, by taking into account that the functional is dimensionless, a possible choice for the physical feasibility constraint enforced by Φ_f is $w_p \equiv w_f = 1/A_{\lambda^2}$ (A_λ^2 being the area of the device normalized to the square amplitude of the considered wavelength). In the same manner, for the circular symmetry constraint one could indeed consider $w_p \equiv w_s = A_n$ (A_n being the area of the pixel). As far as the penalty terms Φ_{ρ_2} and Φ_{ρ_1} is concerned, in order to enforce the sparsity requirement in the best possible way (and without prevailing on data fitting) the weighting coefficient is set according to [142], in which an iterative algorithm for reweighted ℓ_1-minimization is proposed. In particular, $w_p \equiv w_\rho$ is updated at each step of CSI on the basis of the intermediate result as $w_{\rho_{(k+1)}} = 1/[|\chi_k| + \xi]$, while fixing $w_{\rho_{(0)}} = 1$. The parameter $\xi > 0$ has been introduced in [142] in order to provide stability and to ensure that a zero-valued component in $|\chi_k|$ does not strictly prohibit a nonzero estimate at the next step; however, robustness on the choice of ξ has been experienced in [142].

3.4 Assessment of the synthesis procedure

In this Section, the effectiveness of the above proposed design procedure by means of inverse scattering methodologies is proved. For all the examples, the main steps can be summarized as follows:

i. the design constraints are enforced in terms of the total field on the observation surface. In order to deal with non super-directive antennas, caution has to be exercised in order to fix specifications compatible with the DoF of the field radiated by given dimensions antennas (see [17] for more details);
ii. the CSI method is applied to obtain the electromagnetic properties of a lens antenna (whose dimensions are previously fixed) as well as the amplitudes of the considered primary sources . In this step, suitable penalty terms are exploited as "design facilitators";
iii. a forward scattering problem is solved on the synthesized lens in order to compare the arising actual radiated field with the target one (as well as with initial specifications).

In the following, a 'controlled' assessment is firstly carried out with canonical lenses. Then, antennas generating generic given patterns are dealt with.

3.4.1 Validating the proposed tool: (re)designing canonical lenses and beyond

The first example deals with the synthesis of a dielectric profile which emulates the well-known Luneburg lens [119, 120]. As said, the Luneburg lens antenna transforms the point source radiation into the plane wave and vice versa. Ideally, it consists of a spherically symmetric (lossless) dielectric sphere with continuous varying permittivity from two at the center of the inner core to the one at the outer surface, i.e., $\varepsilon_r = 2 - (r/R)^2$, where R is the radius of the sphere. The dielectric profile of the Luneburg lens is shown in fig.3.1(a), while from fig.3.1(b) and fig.3.1(c) it is possible to observe the field it generates on the domain and in the far field, respectively.

The aim of the design procedure is then to determine a GRIN profile which is able to convert a cylindrical wave from a point source to a plane wave. To this end, a lens with radius $R = 1.5\lambda$ is considered and a mask with the same dimensions is defined to force the CSI's algorithm to evolve inside that region of the space. Note that this (available) a priori information allows to further regularize the inverse scattering problem. The lens is embedded in a square domain Ω with side 3.1λ that has been discretized into 86×86 square cells, according to the Richmond's rule [108]. The primary source, located at -1.5λ from the origin of the reference system (that is, centered on the lens rim), is defined as $E_i(\boldsymbol{r}) = H_0^{(2)}(k_b \boldsymbol{r})$. The design constraint is a field with constant phase assigned on 13 equally spaced points belonging to a linear fictitious array 3.1λ long and located at $r_o = 1.7\lambda$. Note that such a constraint represents an aperture field.

Since the angular symmetry of the Luneburg lens' profile naturally allows to accommodate multibeam and scanning capabilities without any degradation, in the synthesis procedure the CSI scheme is constrained by adding the penalty term $\Phi_s(\chi)$ defined as in (3.7). The synthesized dielectric profile is shown in fig.3.1(d). In order to prove the success of the design, the forward scattering problem is solved and the phase of the arising total field is shown in fig.3.1(e) in which a larger domain has been considered. As it can be seen, the cylindrical wave which originates on the left side of the lens is converted on a plane wave on the right hand side, despite the achieved permittivity distribution is different with respect to the canonical lens. Moreover, also the far field power pattern in fig.3.1(f) is in agreement with the design constraints.

Interestingly, the proposed framework is however able to easily produce something more. For example, if a smoother radial variation is desired on the GRIN lens, the penalty term Φ_{ρ_2} can be added so that the functional $\Phi' = \Phi + \Phi_s + \Phi_{\rho_2}$ can be minimized. By so doing, the lens profile of fig.3.1(g) (as well as the phase front of fig.3.1(h) and the far field pattern of fig.3.1(i)) are obtained. As it can be seen, a second satisfactory solution to the problem at hand has been easily obtained, which is more similar to Luneburg lens in fig.3.1(a).

A third interesting solution is also easily found when looking for "easily manufacturable" lens. To this end, the penalty term Φ_{ρ_1} as in (3.9) can be considered in conjunction with Φ_s. The arising lens is reported in fig.3.1(j) while in figs.3.1(k)-3.1(l) the phase of the total field and the pertaining far field are depicted; from these latter (and from all the above cases) it is possible to state that the design procedure is able to furnish GRIN lens carrying out the required waves transformation.

Although the minimization of the ℓ_1-norm involved in the functional $\Phi_{\rho_1}(\chi)$ aims at retrieving a 'sparse' unknown, the arising solution of fig.3.1(j) does not exhibit a step-wise behavior and this is due to the joint minimization with $\Phi_s(\chi)$. In this respect, an a posteriori discretization of the synthesized permittivity profiles has been performed. The so obtained step-wise constant profiles are shown in fig.3.2, in which the permittivity functions of figs.3.2(a),3.2(b),3.2(c) are the discretized version of the profiles in figs.3.1(d),3.1(g) and 3.1(j), respectively. In figs.3.2(d),3.2(e),3.2(f) is depicted a comparison between the far fields radiated by the continuous lens and the respective disctretized lens for the three achieved solutions. As it can be seen, the performances keep almost unchanged, thus showing the actual possibility of manufacturing this kind of devices.

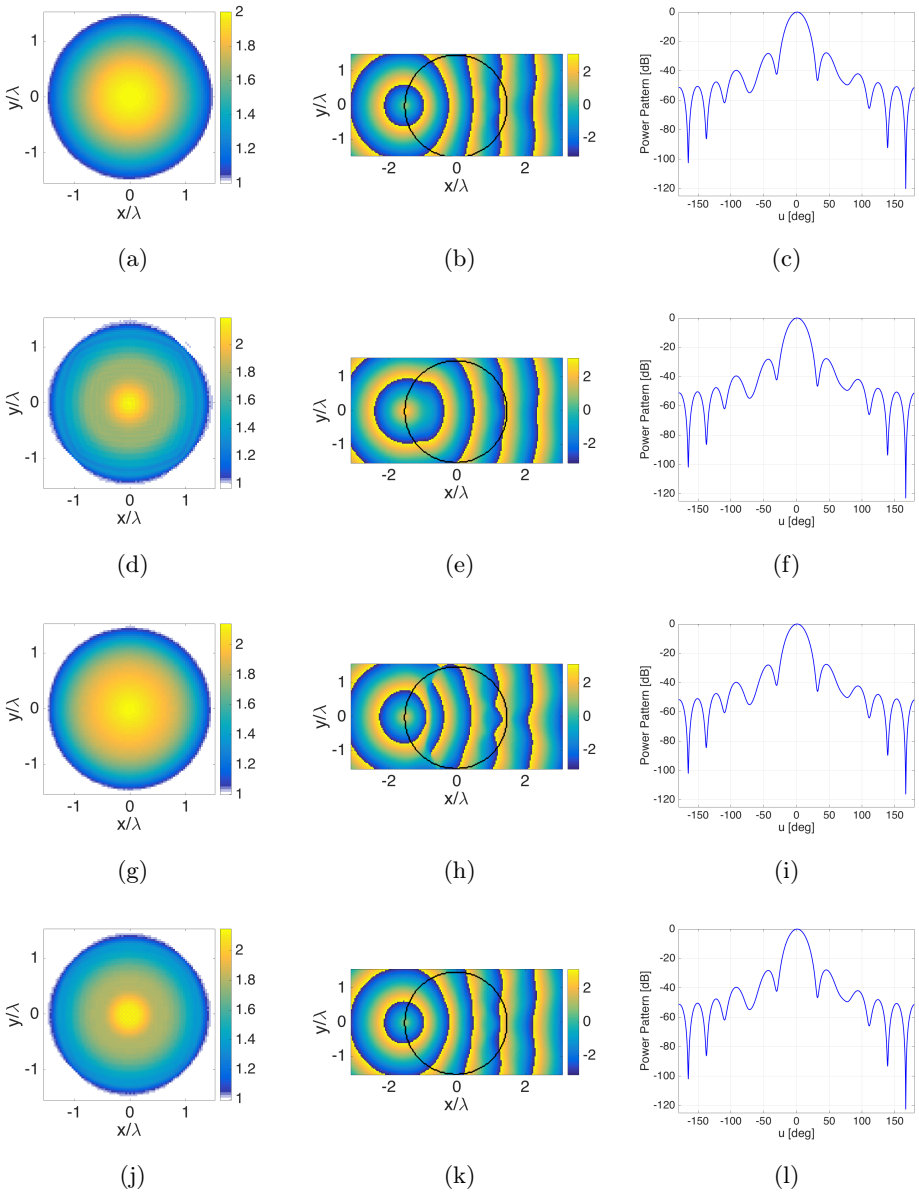

Fig. 3.1. Design of a dielectric antenna emulating the Luneburg lens. On the left: permittivity distribution of the (a) canonical Luneburg lens and of the synthesized lens by exploiting (d) symmetry penalty term Φ_s ($w_s = 1.148 \cdot 10^{-4}$, $\tau = 1$), (g) symmetry Φ_s and smooth $\Phi_{\rho 2}$ ($\xi = 8.7 \cdot 10^3$, $\tau = 0.6188 + j0.7146$) penalty terms, (j) symmetry Φ_s and smooth $\Phi_{\rho 1}$ ($\xi = 10^{-8}$, $\tau = 1$) penalty terms. In the central column: phase of the corresponding total field on a larger domain, in which the black line depicts the contour of the synthesized lens on the left. On the right: the radiated far fields from the lenses evaluated starting from the aperture field.

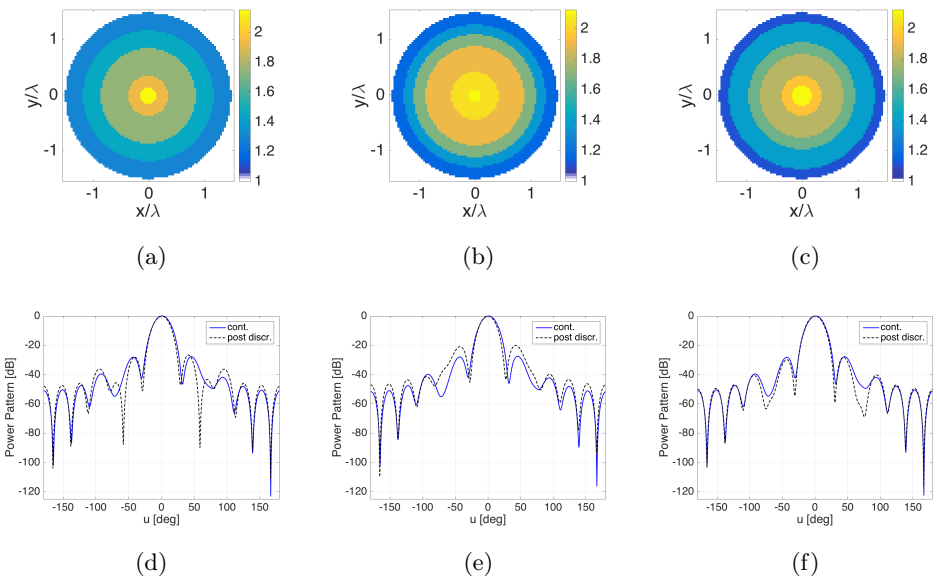

Fig. 3.2. Design of a dielectric antenna emulating the Luneburg lens. On the top: discretized permittivity distribution of the synthesized one by exploiting (a) symmetry penalty term Φ_s (see Fig.3.1(d)), (b) symmetry Φ_s and smooth Φ_{ρ_2} penalty terms (see Fig.3.1(g)) and (c) symmetry Φ_s and smooth Φ_{ρ_1} penalty terms (see Fig.3.1(j)). On the bottom: comparison of the radiated far fields between the continuous and the discretized lens for the three cases above.

In a second set of examples, the design of an antenna emulating the Half Maxwell Fish Eye (HMFE) lens [121] is carried out. Through a Maxwell fish-eye lens, the energy of a point source, placed at one side of the lens, converges into a focus point on the diametrically opposite side of the lens. Due to the symmetry of the structure, a spherical wave at the surface of the lens is converted into a local plane wave at the center of the lens and reemerges as a spherical wave at the surface on the opposite side. Such a behavior is due to the GRIN profile which follows the rule $\varepsilon_r = 4/\left[1+(r/R)^2\right]^2$, R being the radius of the lens. Thus, the HMFE lens transforms a point source into a plane wave and, by reciprocity, a beam of parallel rays incident upon the flat side of the HMFE lens is focused on a point. The permittivity distribution of the canonical HMFE lens is shown in fig.3.3(a), while in figs.3.3(b) and 3.3(c) the generating field on the domain and in the far field are reported, respectively.

The goal is to synthesize a lens with radius $R = \lambda$ which behaves as a HMFE lens. To this aim, a rectangular domain $1.1\lambda \times 2.2\lambda$ large and discretized into 22×44 square cells has been considered. Also in this case, the design constraint is a constant phase aperture field assigned in 9 equally spaced points on a segment 2.2λ long and located just in front of the lens at $r_o = 0.7\lambda$. The same primary source of the previous example, located at $r_t = 0.5\lambda$ is considered. Also in this case, for the synthesis procedure different design facilitators have been adopted and a comparison of the achieved results is reported in fig.3.3. In particular, the dielectric profiles shown in figs.3.3(d),3.3(g) and 3.3(j) have been obtained by exploiting the penalty terms Φ_s, Φ_{ρ_2} and Φ_{ρ_1} as for the previous case. By computing a forward problem on the synthesized lens, the total field inside the ROI is retrieved. As it can be observed from the phase of such a field on a larger domain (see the central column in fig.3.3), the designed lenses fulfill the assigned constraints even although the permittivity distribution is quite different with respect to the canonical case (see fig.3.3(a)). The successful of the design is also confirmed from the radiated far field (evaluated starting from the aperture field) depicted on the right side of fig.3.3.

In order to deal with step-wise constant profiles, which are more easily manufacturable, an a posteriori discretization has been performed on the synthesized continuous lenses of figs.3.3(d),3.3(g) and 3.3(j). The arising devices are shown in figs.3.4(a),3.4(b) and 3.4(c), respectively. As it can be observed, the radiating performances of these latter are almost comparable with the case of continuous lenses, even if a small degradation is present (see figs.3.4(d),3.4(e),3.4(f))

Such results (and all the above ones) show the actual capability of the inverse scattering based design in pursuing assigned field specifications and radiating behaviors by going beyond the canonical solutions.

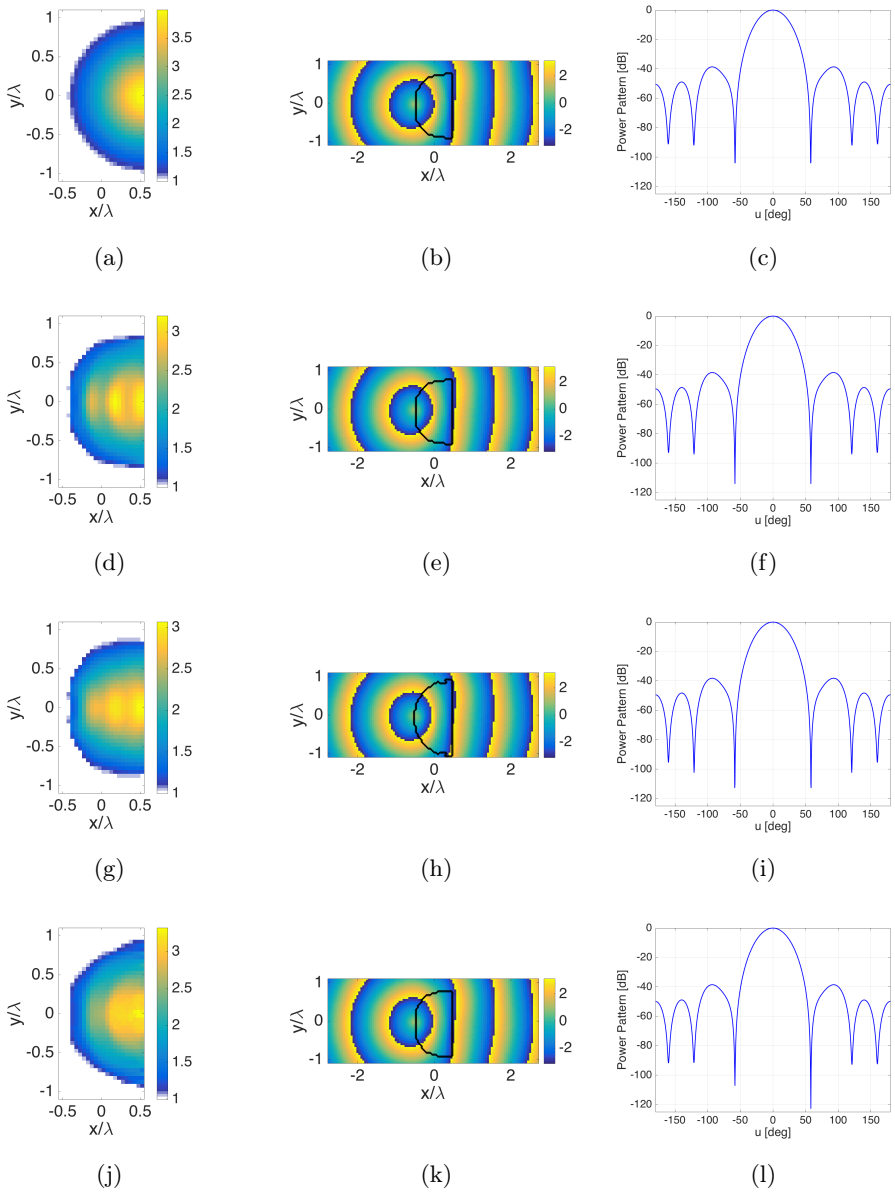

Fig. 3.3. Design of a dielectric antenna emulating the half Maxwell fish eye (HMFE) lens. On the left: permittivity distribution of the synthesized lens by exploiting (a) symmetry penalty term Φ_s ($w_s = 10^{-6}$, $\tau = 1$), (c) symmetry Φ_s and smooth Φ_{ρ_2} ($\xi = 10^8$,$\tau = 0.9135+j0.0842$) penalty terms, (e) symmetry Φ_s and smooth Φ_{ρ_1} ($\xi = 10^{-7}$, $\tau = 1$) penalty terms. On the right: phase of the corresponding total field on a larger domain; the black line depicts the contour of the synthesized lens on the left.

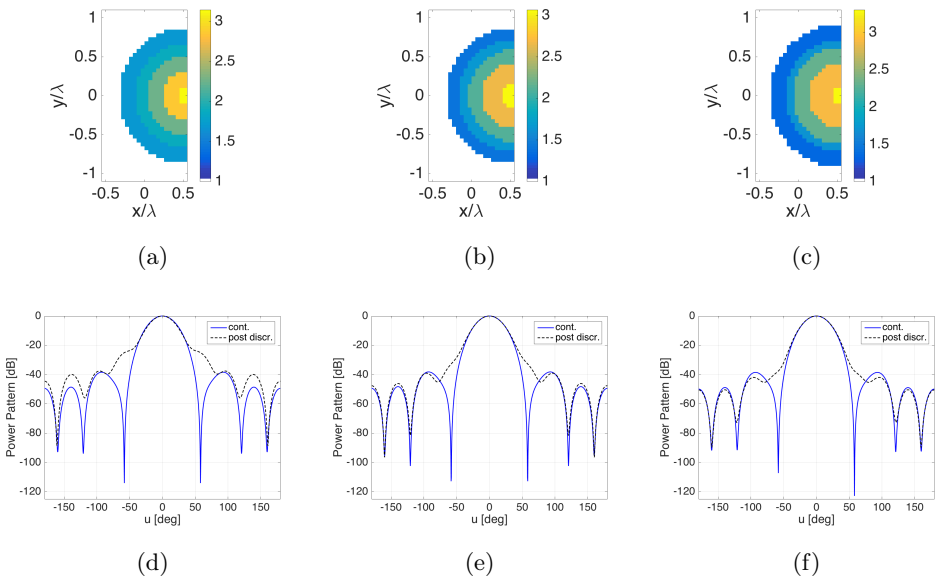

Fig. 3.4. Design of a dielectric antenna emulating the half Maxwell fish eye (HMFE) lens. On the top: discretized permittivity distribution of the synthesized one by exploiting (a) symmetry penalty term Φ_s (see Fig.3.3(d)), (b) symmetry Φ_s and smooth Φ_{ρ_2} penalty terms (see Fig.3.3(g)) and (c) symmetry Φ_s and smooth Φ_{ρ_1} penalty terms (see Fig.3.3(j)). On the bottom: comparison of the radiated far fields between the continuous and the discretized lens for the three cases above.

3.4.2 Design of antennas generating generic reconfigurable given patterns

The proposed inverse scattering based design tool is quite general and hence viable for different kinds of devices. Notably, if a "multi-view" inverse scattering problem is considered, the above devised procedure immediately leads itself to the synthesis of (easily) reconfigurable antenna, which is the case we deal in the remainder of the Chapter. In this Section, the proposed strategy is assessed with the design of a lens antenna generating a Σ/Δ reconfigurable pattern. This is useful for monopulse radar applications in which the target's position is calculated by comparing two signals, the so-called sum and difference signals. To this aim, monopulse antennas are required to provide both sum (Σ) and difference (Δ) patterns, the former having one main lobe along the target direction and the latter exhibiting a null in the same direction [143]. In the literature, a lot of methods are available for the synthesis of monopulse antennas, usually relying on either arrays or reflectors [144–147]. With respect to common architectures, circularly symmetric dielectric lenses achievable by means of inverse scattering methodologies represent an interesting alternative, since they allow to overcome beam degradation or mechanical scanning problems.

The synthesis of the above mentioned lens antenna is pursued by adopting the proposed design method. In particular, the overall procedure can be summarized as follows:

i. *Definition of the far field target fields*: by exploiting the approach in [146], and taking into account the available DoF [18], a circular harmonics expansion is considered for the fields and two convenient far field patterns are synthesized which obey to given mask constraints. Notably, by exploiting the framework of "optimal synthesis" developed during the years at Università Mediterranea, "optimal" patterns are looked for in such a step. In particular (see Appendix E) we look for profiles maximizing the slope in the Δ mode, and subject to some minimal guaranteed performance in the Σ mode, as well as to upper bounds on sidelobes in both modalities.

ii. *Determination of the equivalent near field target fields*: in order to avoid possible numerical drawbacks which could arise when reasoning in terms of far fields, the observation domain Γ_o is positioned in the near field region and a backpropagation (from the synthesized far fields) is used in order to evaluate the target fields E on Γ_o. As just harmonics having an index $n : |n| \leq k_b R$ are used (R being the radius of the lens), the step is stable with respect to a small variations of the far field.

iii. *Solution of the inverse scattering problem*: once the total field E on Γ_o has been defined, the optimization problem involved in the modified CSI method is solved.

More details about points i. and ii. are given in Appendix E.

In order to solve the inverse scattering problem, let us set the radius of the antenna equal to $R = 2\lambda$ and consider $\widehat{E}_i^{(v)}(\mathbf{r}) = H_0^{(2)}(\beta_0 r)\, cos^4\vartheta$ as primary source, $\mathbf{r} = (r, \vartheta)$ being the coordinate of the generic point belonging to a reference system centered on the phase center of the feed. In particular, the design constraints imply that $T = 2$ primary incident fields have to be used. By referring to Fig. 3.5, if the one placed at ($r_t = 3.1\lambda$, $\theta_t = 0$) is active, the Σ-pattern is provided, while when the two feeds located at ($r_t = 3.1\lambda$, $\theta_t > 0$, $\theta_t = 20°$) are simultaneously active and excited with an opposite phase, the corresponding total field will provide the Δ-pattern. In particular, the design constraints are imposed on an arc of circumference Γ_o located at $r_o = 4.5\lambda$ (which is in the near field) and $\theta_o \in [-120° \div 120°]$. Fitting the actual field to the reference field (as determined in the first step) requires of course a sampling of (both) the reference and the actual field. Adopting a number of sampling points as discussed in [18] allows to enforce such a fitting in an accurate while non redundant fashion.

Finally, the region of interest Ω which is $4.5\lambda \times 4.5\lambda$ large has been discretized into 80×80 square cells, according to [108].

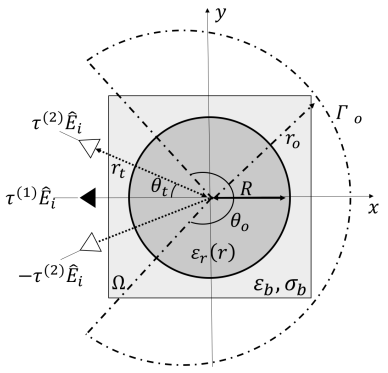

Fig. 3.5. Synthesis of a Σ/Δ reconfigurable pattern antenna: the reference scenario. Two sets of excitations are depicted: if the "black triangle" antenna is active, then a sum (Σ) pattern is radiated; if the "white triangle" antennas are active and excited with an opposite phase, then a difference (Δ) pattern is radiated.

The synthesized continuous GRIN lens is shown in fig.3.6(a). In using the modified CSI method, we added the penalty terms Φ_s and Φ_f to the cost functional (3.3), in order to enforce on the permittivity profile a circularly symmetric behavior and real values larger than 1. Moreover, we enforced conductivity values $\sigma_r(\mathbf{r}) = 0$ in order to avoid power losses due to the propagation of the field inside the lens.
In order to keep under control the overall process, we computed the total field corresponding to the synthesized continuous profile and to the synthesized value of τ ($\tau = [-2.6084 - j7.8221, 1.7136 + j8.1632]$). The resulting far field patterns are reported in fig.3.6(b) and 3.6(c) (see dot-dashed blue lines). As it can be seen, the synthesized GRIN lens well satisfies the far field mask constraints keeping almost unchanged the beamwidth (BW) of the main lobes and the sidelobes level (SLL) [148] (see Table 3.1 for a quantitative comparison).

For completeness, the solution of the inverse scattering problem by exploiting the penalty term ϕ_{ρ_2} in conjunction with Φ_s and Φ_f has also been carried out. The outcome is shown in fig.3.7(a) and the corresponding far field patterns in fig.3.7(b) and 3.7(c), relative to the pertaining synthesized τ ($\tau = [-4.5029 - j7.0872, 4.1795 + j6.8097]$), still shown the effectiveness of the approach, as also demonstrated by parameters in Table 3.1.

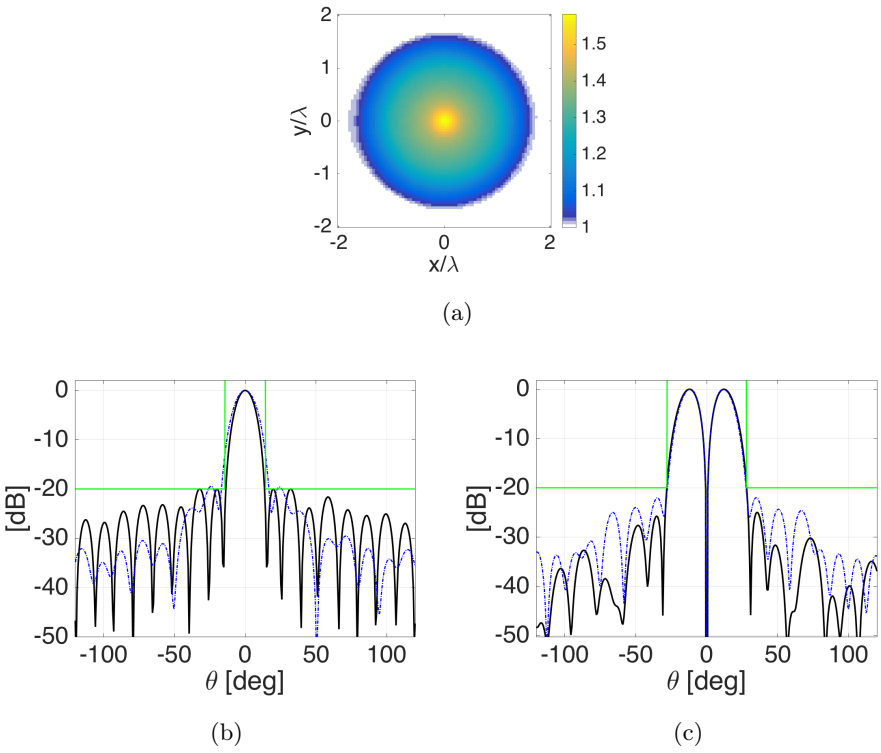

(a)

(b) (c)

Fig. 3.6. Synthesis of a Σ/Δ reconfigurable pattern antenna. (a) Real part of the permittivity function of the synthesized GRIN lens by inverse scattering and penalty terms Φ_s and Φ_f ($w_s = 2.5 \cdot 10^{-3}$, $w_f = 0.1$, $N_c = 80 \times 80$). Far field (c) sum and (d) difference power patterns radiated by the synthesized lens (dot-dashed blue lines). Continuous black and green lines represent the specified far field power patterns and the mask constraints, respectively.

Table 3.1. Synthesis of a Σ/Δ reconfigurable pattern antenna: comparison of the synthetic parameters for the far field patterns.

	BW @ -20dB [deg]		**SLL [dB]**	
	Σ	Δ	Σ	Δ
mask constraints	28	56	-20	-20
GRIN lens by $\Phi' = \Phi + \Phi_s + \Phi_f$	38	58	-17.9	-25.27
GRIN lens by $\Phi' = \Phi + \Phi_s + \Phi_f + \Phi_{\rho_2}$	38	58	-17.9	-25.27

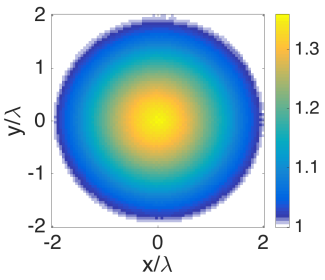

(a)

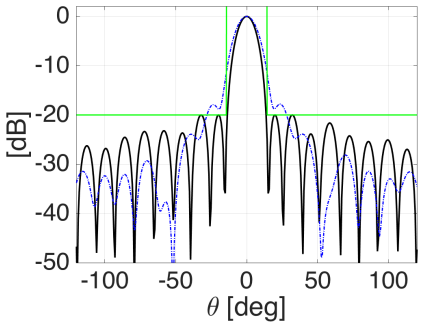

(b)

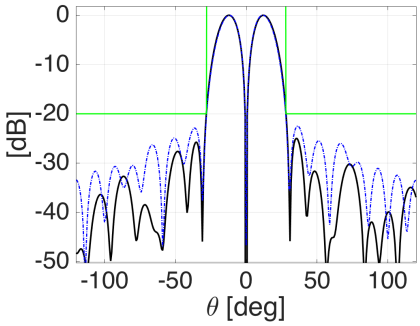

(c)

Fig. 3.7. Synthesis of a Σ/Δ reconfigurable pattern antenna. (a) Real part of the permittivity function of the synthesized GRIN lens by inverse scattering and penalty terms Φ_s, Φ_f and Φ_{ρ_2} ($w_s = 2.5 \cdot 10^{-3}$, $w_f = 0.1$, $\epsilon =$, $N_c = 80 \times 80$). Far field (c) sum and (d) difference power patterns radiated by the synthesized lens (dot-dashed blue lines). Continuous black and green lines represent the specified far field power patterns and the mask constraints, respectively.

3.5 An Artificial Materials based solution

Up to now, the solutions resulting from the modified CSI have shown a far from trivial GRIN profile also in presence of penalty terms, since the involved unknowns are implicitly expressed in the common pixel representation basis which is meant to mimic a generic continuous profile. As already stressed, the actual manufacturing realization of a GRIN device with a generic gradient index profile is not however a trivial task.

In the last decades, a great interest was devoted to realize GRIN structures by means of conveniently designed Photonic Crystals (PCs) [149]. PCs are periodic dielectric or metallic structures that are artificially designed to control and manipulate the propagation of light. A photonic crystal can be made either by arranging a lattice of air holes on a dielectric background ("hole-type" crystal) or by forming a lattice of high refractive index material embedded in a transparent medium with a lower refractive index ("rod-type" crystal). Applications of PCs depend on either their photonic band gaps or tunable dispersion achieved by suitable engineering of the basic structure, e.g., the filling factor, the lattice period, and/or material index. In particular, the lattice period (i.e., the distance between two adjacent unit cells) defines the feature of a photonic crystal. Usually, it is set to be comparable to the wavelength in the background medium, especially when the photonic bandgap is exploited to ensure proper functioning of PCs. However, when the gradient of the basic structure is considered to guide the electromagnetic wave, such a constraint can be relaxed. This condition is referred in literature as "PCs in metamaterials regime" [150] and it is widely used and successfully applied for the realization of canonical lenses [151–155]. As a matter of fact, in these papers the canonical GRIN lens is linked to the graded PCs by means of the homogenization theory, which instead holds in case of smaller and smaller lattice period.

In the following, the above mentioned graded PCs based structures in the metamaterials regime will be dealt. However, to avoid any kind of terminology misunderstanding, we will refer to *graded Artificial Materials* (GAMs). In particular, 2D circular GAMs structures made by cylindrical dielectric rods will be considered and their design by means of either a gradient of the refractive index or a gradient of the filling factor will be proposed.

3.5.1 Engineering the inclusions values: a new expansion for the contrast function

Let us consider that the arrangement of the rods in the basic structure of the GAMs as well as their radius (which is assumed the same) are known a priori. In order to directly look for a synthesis of a GAMs device exhibiting a gradient of the refractive index (GAM_R), one can expand the unknown contrast function by means of a proper basis function which projects it into the 'space of rods' and adopt it into the modified CSI functional (3.3). Such an expansion can be given as:

$$\chi(\boldsymbol{r}) = \sum_{k=1}^{K} \chi_k \Pi_k(\boldsymbol{r}_k), \quad \boldsymbol{r} \in \Omega \tag{3.10}$$

in which $\Pi_k(\boldsymbol{r}_k)$ are suitable circular (on-off) windows centered in $\boldsymbol{r}_k$, χ_k are the actual unknowns of the problem and K is the total number of these unknowns.
By modifying the representation basis, it is possible to design different kinds of devices exhibiting different permittivity's spatial variation.

A first possibility amounts of course to allow for K different permittivity values, K being in this case the total number of rods which made up the structure. As a consequence, each rod will be made by a different material.

A second possibility, which is the one of interest in what follows, amount to consider *circularly symmetric distributions*. In fact, such a property is useful when the functionality of the device should keep unchanged when changing the illumination direction. In this case, the permittivity value to synthesize must be the same for the rods belonging to the same ring. From a mathematical point of view, in such a case the expansion (3.10) can be written as:

$$\chi(\boldsymbol{r}) = \sum_{k=1}^{K} \chi_k \sum_{h=1}^{H_k} \Pi_{kh}\left(\frac{\boldsymbol{r} - \boldsymbol{r}_{kh}}{a_k}\right), \quad \boldsymbol{r} \in \Omega \tag{3.11}$$

in which χ_k is the contrast value associated to the k-th ring of rods, K is in this case the total number of the rings for the arrangement of the rods, H_k is the number of inclusions along the k-th ring, $\boldsymbol{r}_{kh}$ is the position of the center of the h-th rod belonging to the k-th ring, and $|\boldsymbol{r}_{kh}| = r_k$. Moreover, each $\Pi_{kh}\left(\frac{\boldsymbol{r}-\boldsymbol{r}_{kh}}{a_k}\right)$ function (which is associated to a single rod) is a circular window of radius a_k centered in $\boldsymbol{r}_{kh}$. As a consequence, the internal summation defines a composite window which is different from zero in each rod belonging to the k-th ring, and zero elsewhere. A graphic representation of the $\Pi_{kh}(\boldsymbol{r})$ functions for this circumstance is shown in fig.3.8.

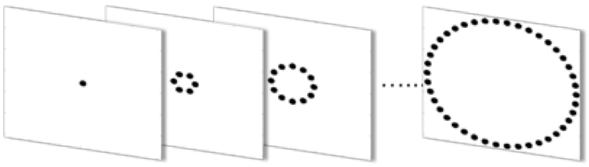

Fig. 3.8. Graphic representation of the expansion's basis in case of circularly symmetric distribution.

A third possibility which is also of interest, is enforcing that different rings exhibit rods having exactly the same permittivity, which would further simplify realization of the device at hand. Notably, in case this property is required on adjacent rings, and if clustering is not fixed a priori, enforcement of such a property could be effectively performed by CS tool (where finite difference $\Delta_k \chi_k = \chi_k - \chi_{k+1}$ would be the sparse unknown). In fig.3.9 is shown the graphical representation of this circumstance in conjunction with the previous symmetry property.

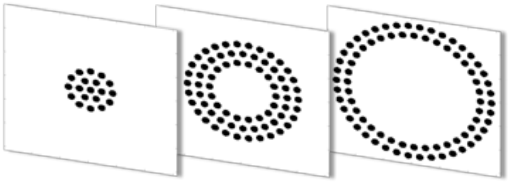

Fig. 3.9. Graphic representation of the expansion's basis in case of circularly symmetric and sparse distribution.

3.5.2 Engineering the filling factor: a smart analytical tool

A more interesting design solution is to determine GAMs with a gradient of the filling factor (GAM_F), namely a structure in which the contrast value of the rods is always the same in all rings, and the radii (in each ring) are instead the actual degrees of freedom of the problem. In fact, just a single material is required in such a case. However, the direct search for the radii is a very difficult task because of the indirect way the actual unknowns a_k enter into the inverse scattering problem, thus increasing its non linearity.

Very interestingly, by using classical analytical tools one can exploit the outcomes of the (partial) result in Section 3.5.1 to synthesize GAM_F in a simple fashion. To be specific, let us take advantage from the fact that the scattering behavior of each inclusion can be conveniently analyzed in terms of a so-called scattering matrix [156], thus allowing some smart determination of the radii. In particular, by adopting a

cylindrical coordinate system centered on the axis of a dielectric[2] circular cylinder of radius a, we can write an expansion in cylindrical harmonics for the incident ($\widetilde{E}_i$), total ($\widetilde{E}$) and scattered ($\widetilde{E}_s$) field, respectively, pertaining to the single inclusion [156]:

$$\widetilde{E}_i(\rho,\theta) = \sum_{n=-\infty}^{+\infty} a_n J_n\left(k_b\rho\right) e^{jn\theta} \tag{3.12}$$

$$\widetilde{E}(\rho,\theta) = \sum_{n=-\infty}^{+\infty} b_n J_n\left(k_r\rho\right) e^{jn\theta} \tag{3.13}$$

$$\widetilde{E}_s(\rho,\theta) = \sum_{n=-\infty}^{+\infty} c_n H_n^{(2)}\left(k_b\rho\right) e^{jn\theta} \tag{3.14}$$

where a_n, b_n and c_n are the expansion's coefficients, J_n and $H_n^{(2)}$ being the n-th order Bessel function and Hankel function of second kind, respectively, while k_r is the wave number of the dielectric medium filling the cylinder. Hence, the "response" of a homogeneous cylindrical scatterer can be conveniently analyzed in terms of the scattering coefficients $s_n = c_n/a_n$. By considering the expansion (3.12)-(3.14) and by applying the boundary conditions on the cylinder interface (i.e., for $r = a$), one easily achieves [156]:

$$s_n = \frac{c_n}{a_n} = \frac{k_r J_n'\left(k_r a\right) J_n\left(k_b a\right) - k_b J_n\left(k_r a\right) J_n'\left(k_b a\right)}{k_b J_n\left(k_r a\right) H_n^{(2)'}\left(k_b a\right) - k_r J_n'\left(k_r a\right) H_n^{(2)}\left(k_b a\right)} \tag{3.15}$$

By applying the recurrence formulas for derivatives of the Bessel and Hankel functions [157], eq.(3.15) can also be turned into:

$$s_n = \frac{\left(k_r a\right) J_{n-1}\left(k_r a\right) J_n\left(k_b a\right) - \left(k_b a\right) J_n\left(k_r a\right) J_{n-1}\left(k_b a\right)}{\left(k_b a\right) J_n\left(k_r a\right) H_{n-1}^{(2)}\left(k_b a\right) - \left(k_r a\right) J_{n-1}\left(k_r a\right) H_n^{(2)}\left(k_b a\right)}. \tag{3.16}$$

Note that, besides the dependence on the radius a, s_n intrinsically depends also on the contrast function χ through k_b and k_r. Both analytical and numerical studies indicate that in case of electrically small cylinders $|s_0| \gg |s_i|, i \neq 0$, which is the circumstance that we will exploit in the following.

A numerical study of the s_n coefficients' values is summarized in fig.3.10, in which the amplitude of the first three terms (i.e., s_0, s_1 and s_2, also being $|s_{-1}| = |s_1|$ and $|s_{-2}| = |s_2|$) is depicted. In particular, the curve's behavior has been evaluated varying the contrast function and fixing the radius of the cylinder in fig.3.10(a), and varying instead the radius and fixing the contrast value in fig.3.10(b). Notably, three possibilities have been considered for each case.

The numerical study shows that, as long as the dielectric cylinder is sufficiently small with respect to the wavelength, the term s_0 is much larger than all the other, and

[2] Same arguments can be exploited for metallic inclusions.

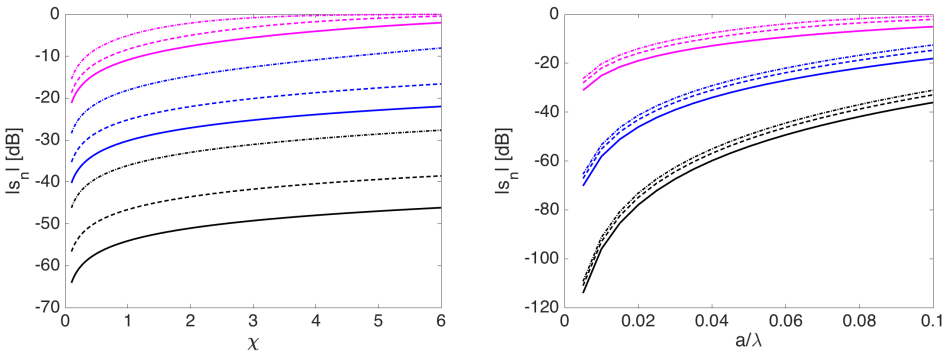

(a) (b)

Fig. 3.10. Magnitude of the scattering coefficient s_0 (magenta lines), s_1 (blue lines) and s_2 (black lines) for: (a) varying the contrast function at fixed $a = \lambda/20$ (continuous line), $a = \lambda/15$ (dashed line) and $a = \lambda/10$ (dash-dotted line), (b) varying the radius of the cylinder at fixed $\chi = 1$ (continuous line), $\chi = 2$ (dashed line) and $\chi = 3$ (dash-dotted line).

the scattering phenomenon is essentially determined from the $n = 0$ term. Then, one can keep unaltered the behavior of s_0 (and in a first instance of the overall scattering phenomena) by performing an interchange between the local contrast value χ_k of the k-th rod and the radius a_k.

Such an interchange can be performed as follow:

i. solve the inverse scattering problem by minimizing functional (3.3) using the representation (3.11) for the contrast (with a_k equal to a fixed value of a);
ii. for each k-th ring, namely for each χ_k, evaluate $s_0(\chi_k, a)$ from eq. (3.16) which becomes the $s^k_{0_{target}}$;
iii. fix a value for χ meant to realize the GAM_F and solve, for each k-th ring, the following fitting problem:

$$Find\ a_k\ such\ that\ |s_0(\chi, a_k) - s^k_{0_{target}}|^2\ is\ minimum. \tag{3.17}$$

3.5.3 Validating the developed tools

The assessment of the proposed methodologies for GAM_R and GAM_F is performed by considering the same example of Section 3.4.2, namely by looking at synthesizing a GAMs lens radiating a reconfigurable Σ/Δ pattern. Therefore, the design procedure keeps the same, as well as all the involved parameters, except for the numerical discretization which is herein considered very dense in order to correctly model the small circular windows involved in representation (3.11) (and also in the interchanging tool). The penalty term $\Phi_f(\chi)$ is also considered in the cost functional (3.3) in order to deal with bulk materials.

In order to achieve a circularly symmetric radiating behavior, the expansion (3.11) for the contrast function is adopted in the cost functional (3.3), wherein a number of rings equal to $K = 11$ and a radius for each inclusion equal to $a = \lambda/15$ have been fixed. As far as the arrangement of the rods is concerned, by taking inspiration from [152] a six-fold rotational symmetry is considered (see fig.3.11); in particular, the rods positions on the xy plane (except for the center one) are given by:

$$x_{k,h} = dk\ cos\left(\frac{2h\pi}{6k}\right) \qquad y_{k,h} = dk\ sin\left(\frac{2h\pi}{6k}\right) \tag{3.18}$$

wherein $k = 1, .., K-1$ is the radial index scanning the rings, $h = 1, ..., 6H_k$ is the angular index, while $d = (R - \lambda/10)/K$ is the periodicity of the adopted triangular unit cell reported in fig.3.11.

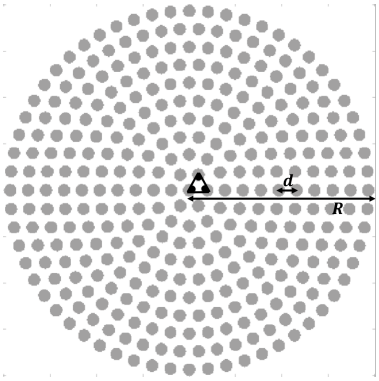

Fig. 3.11. AM-based structure with a six-fold rotational symmetry. The triangular unit cell is marked with solid black lines.

The permittivity profile of the obtained GAM_R-based lens is shown in fig.3.12(a). Note that the synthesis procedure leads to a permittivity value for the external ring equal to 1, so that the overall device results smaller (and actually composed by 10 rings). By using the synthesized value of τ ($\tau = [0.8348 - j8.5656, -1.7077 + j8.7196]$), one achieves the corresponding Σ and Δ far field patterns, which are depicted in fig. 3.12(c) and 3.12(d) (dot-dashed blue lines). As it can be seen, the new strategy that allows to directly synthesize GAM_R works well, since the design constraints as well as the far fields masks are fulfilled.

Although the achieved device is of interest *by per se* (as several fabrication strategy can be exploited for manufacturing), a GAM_F solution is even more interesting. Therefore, the analytic interchanging tool detailed in Sec.3.5.2 has been applied on the GAM_R by adopting a dielectric material with $\varepsilon_r = 4.5$ (SiO_2) for the inclusions. The so-obtained GAM_F profile is given in fig.3.12(b), and the corresponding fields is depicted in fig.3.12(c) and 3.12(d) with red dotted lines. As it can be observed,

the resulting gradient of the filling factor allows to control the electromagnetic field path and to fully satisfy the initial specifications, thus keeping almost unchanged the GAM_R's performances. Such a result proves that the analytic interchanging allows to preserve the scattering behavior of the lens.

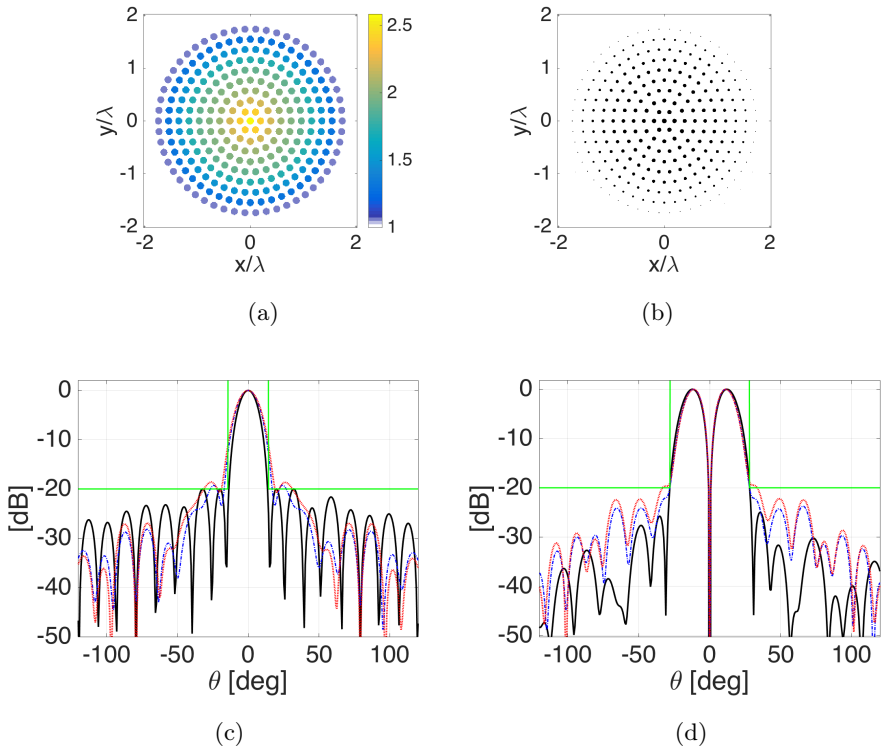

Fig. 3.12. Synthesis of a Σ/Δ reconfigurable pattern GAMs antenna, $K = 11$. (a) Real part of the permittivity function of the synthesized GAM_R lens by inverse scattering, expansion (3.11) and penalty term Φ_s (w_f =, $N_c = 408 \times 408$) and (b) equivalent GAM_F lens by interchanging procedure ($\varepsilon_r = 4.5$, $N_c = 1224 \times 1224$). Far field (c) sum and (d) difference power patterns radiated by the synthesized lens (dot-dashed blue lines). Continuous black and green lines represent the specified far field power patterns and the mask constraints, respectively.

With the aim to further reduce the complexity of the synthesized devices, the same procedure has been applied by reducing the number of rings; in particular, the minimization of (3.3) is pursued by using $K = 9$ and $a = \lambda/10$ for the inclusions. In fig.3.13(a) the corresponding GAM_R lens is reported. Note that also in this case the rods in the outer ring have unitary permittivity and hence the lens is actually composed by 8 rings. As it can be seen from the corresponding patterns in fig.3.13(c) and 3.13(d) (dot-dashed blue lines), it still allows to perform at best the patterns reconfiguration ($\tau = [0.2553 - j8.4487, -1.2238 + j8.7385]$). Interestingly, also the

analytical interchanging is successful, so that an effective GAM_F antenna is finally achieved (see fig.3.13(b) and the dotted red lines in fig.3.13(c) and 3.13(d)).

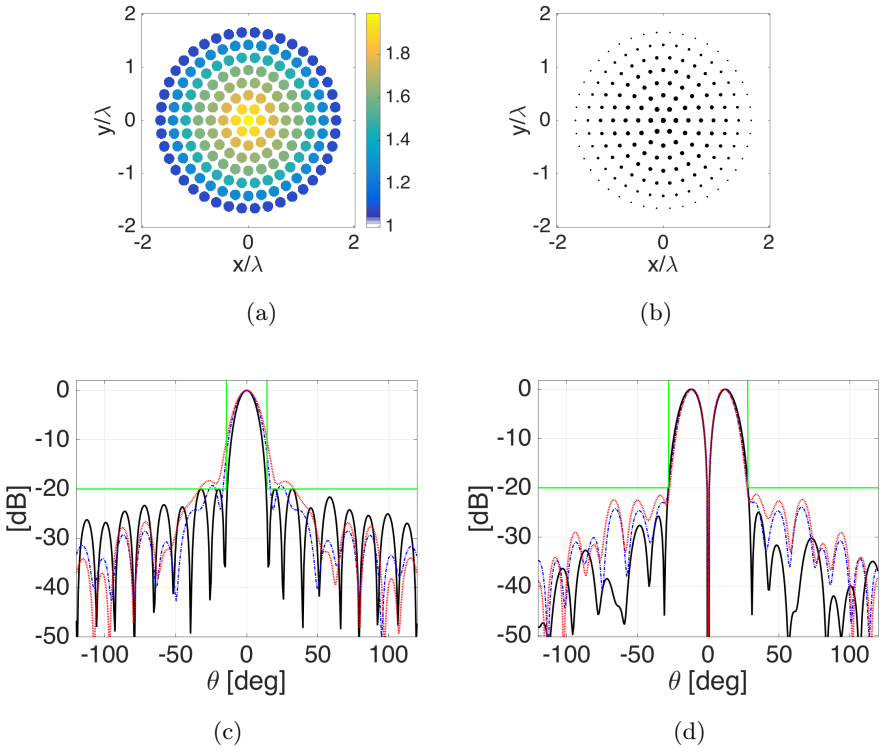

Fig. 3.13. Synthesis of a Σ/Δ reconfigurable pattern GAMs antenna, $K = 9$. (a) Real part of the permittivity function of the synthesized GAM_R lens by inverse scattering, expansion (3.11) and penalty term Φ_s (w_f =, $N_c = 408 \times 408$) and (b) equivalent GAM_F lens by interchanging procedure ($\varepsilon_r = 4.5$, $N_c = 1224 \times 1224$). Far field (c) sum and (d) difference power patterns radiated by the synthesized lens (dot-dashed blue lines). Continuous black and green lines represent the specified far field power patterns and the mask constraints, respectively.

3.5.4 A comparison with an alternative and more straightforward strategy

In order to better emphasize the usefulness and the effectiveness of the proposed strategy, a comparison with an alternative strategy is now given. In particular, by starting from the GRIN profile obtained in Sect.3.4.2, the mixing formulas [158] arising from the Maxwell-Garnett effective medium theory can be applied to obtain an equivalent GAM_F device. Note that, to the best of my knowledge, such an approach is a novelty as well when considering non canonical patterns and profiles. As a matter of fact, up

to now the mixing formulas have just been applied to canonical devices and, in particular, to the realization of the Luneburg lens [151–155]. Conversely, they are herein exploited for generic GRIN distribution as follows:

- the synthesized GRIN profile $\varepsilon_r(\boldsymbol{r}) \equiv \varepsilon_r(\boldsymbol{r}_s)$, $s = 1, .., N_p$ pixels, by means of the modified CSI, is re-sampled in a very dense grid, i.e., $\varepsilon_r(\boldsymbol{r}) \equiv \varepsilon_r(\boldsymbol{r}_{\tilde{s}})$, $\tilde{s} = 1, .., \tilde{N}_p$, with $\tilde{N}_p \gg N_p$;
- by referring to representation (3.11), K, H_k and Π_{kh} are set at will;
- $\forall$ k-th ring, the permittivity value $\varepsilon_{r_{kh}} = \varepsilon_r(\boldsymbol{r}_{kh})$ is considered to estimate the pertaining radius for each h-th rod by [152]:

$$a_{kh} = \sqrt{\frac{S}{\pi N} \frac{(\varepsilon_b - \varepsilon_{r_{kh}})(\varepsilon_b + \varepsilon_F)}{(\varepsilon_b + \varepsilon_{r_{kh}})(\varepsilon_b - \varepsilon_F)}} \tag{3.19}$$

  wherein ε_F is the chosen value for the GAM_F, S is the area of the adopted unit cell and N is the number of rods in the unit cell.

Note that the GRIN profile dealt herein are circularly symmetric, and hence the radius will be the same for all the rods belonging to the k-th ring, i.e., $a_{kh} \equiv a_k$.

In fig.3.14(a) the GAM_F arising from the GRIN profile in fig.3.6(a) (from here on out referred to as #1), by adopting $K = 11$ and $\varepsilon_F = \varepsilon_r = 4.5$ is shown. The forward problem is solved on this profile by using the synthesized τ pertaining to the profile in fig.3.6(a) in order to evaluate the far field power patterns reported in fig.3.14(b) and 3.14(c). As it can be seen, the antenna does not fulfill expectations, since its patterns do not match the given ones and the mask constraints are also violated. Such a circumstance can be attributed to the homogenization itself, which may get into troubles in case of a (relatively) rapidly varying refractive index. In fact, when applying the formula (3.19) on the smooth profile synthesized in Sect.3.4.2 and reported in fig.3.7(a) (referred to as #2), the same strategy comes out to be effective, as the homogenization procedure leads now to a much better solution (see the patterns in fig.3.15(b) and 3.15(c), which are relative to the GAM_F in fig.3.15(a)). However, even starting from a smooth profile, the homogenization based procedure fails when using a reduced number of rings, as pointed out from the synthetic parameters in Table 3.2. Finally, it has also been observed that if the material of the rods is set to a lower permittivity value as, for instance, $\varepsilon_r = 1.8$, the homogenization gives better performances, but this corresponds to uncommon materials.
All the above statements are proved by a comparison of the SLL and BW of the radiated patterns reported in Table 3.2.

As a consequence of the above numerical examples (and many others) it can be concluded that the strategy proposed in Sections 3.5.1-3.5.2 outperforms the more

straightforward homogenization procedure. This can be attributed to the circumstance of avoiding in the first case the intermediate synthesis of a continuous profile, whose characteristics may be difficult to emulate by means of a GAMs.

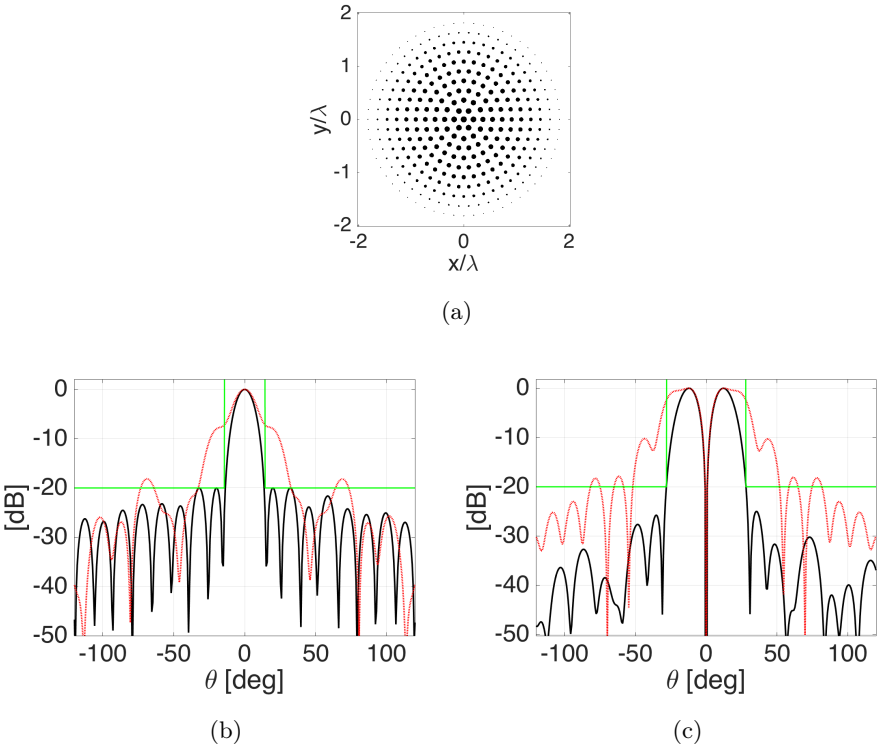

Fig. 3.14. Synthesis of a Σ/Δ reconfigurable pattern GAM_F antenna by homogenization: case #1. (a) GAM_F device derived from circularly symmetric profile in Fig. 3.6(a) ($\varepsilon_r = 4.5$, $N_c = 1224 \times 1224$) and the corresponding far field (b) sum and (c) difference power patterns (dot red lines). Continuous black and green lines represent the specified far field power patterns and the mask constraints, respectively.

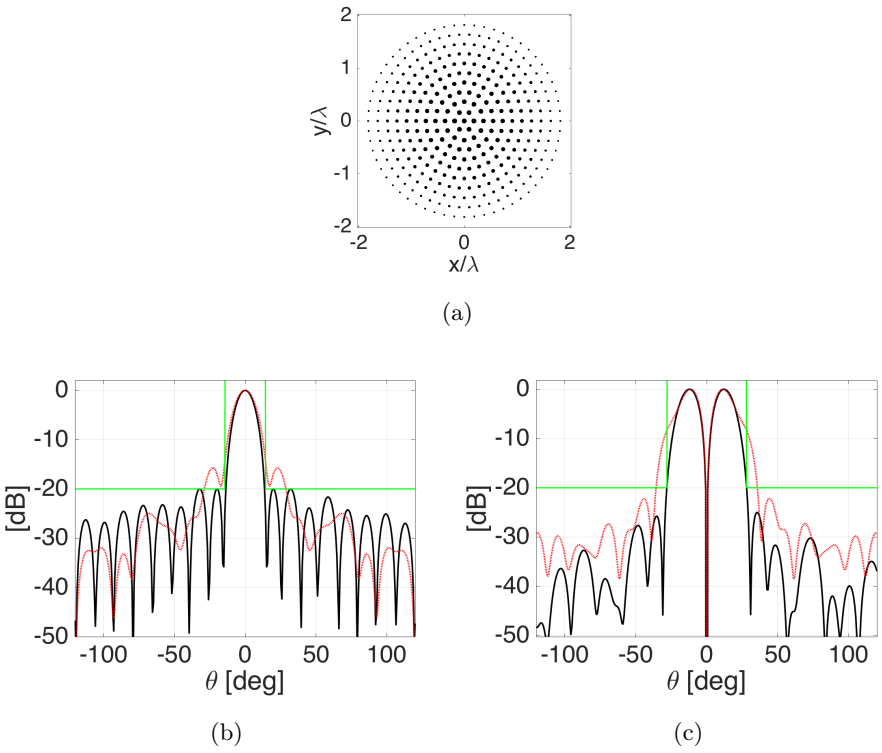

(a)

(b)

(c)

Fig. 3.15. Synthesis of a Σ/Δ reconfigurable pattern GAM_F antenna by homogenization: case #2. (a) GAM_F device derived from circularly symmetric profile in Fig. 3.7(a) ($\varepsilon_r = 4.5$, $N_c = 1224 \times 1224$) and the corresponding far field (b) sum and (c) difference power patterns (dot red lines). Continuous black and green lines represent the specified far field power patterns and the mask constraints, respectively.

Table 3.2. Synthesis of a Σ/Δ reconfigurable pattern GAMs antenna: comparison of the synthetic parameters for the far field patterns.

	BW @ -20dB [deg]		**SLL [dB]**	
	Σ	Δ	Σ	Δ
mask constraints	28	56	-20	-20
Case 1: GAMs from inverse scattering				
GAM_R lens with $K = 11$	34	56	-19.3	-23.7
equivalent GAM_F by analyt. tool ($\varepsilon = 4.5$)	37.5	66	-18.65	-22.45
GAM_R lens with $K = 9$	34	56	-19.3	-23.9
equivalent GAM_F by analyt. tool ($\varepsilon = 4.5$)	45	55	-18.45	-21.3
Case 2: GAM_F from MG				
GAM_F from #1 with $K = 11$ and $\varepsilon = 4.5$	66	103.6	-18.2	-18
GAM_F from #1 with $K = 9$ and $\varepsilon = 4.5$	66	97	-18.5	-17.8
GAM_F from #2 with $K = 11$ and $\varepsilon = 4.5$	34.5	70	-15.75	-22.15
GAM_F from #2 with $K = 9$ and $\varepsilon = 4.5$	56	72	-15.1	-19.6

3.6 Concluding remarks

In this Chapter the design of new GRIN antennas has been pursued by exploiting the well-known CSI scheme. In particular, novel synthesis strategies have been proposed which are based on a proper extension and modification of the CSI algorithm. As a first contribution, the synthesis of the excitations of otherwise fixed primary sources has been proposed as a further useful possibility. Then, further modifications have been proposed which allow to enforce desired properties on the unknown antenna's permittivity distribution. Finally, a new representation for the contrast function has been proposed in order to deal with the synthesis of GAMs devices. In this respect, two strategies have been discussed allowing the design of the inclusions values and dimensions, respectively.

The developed tools have been firstly validated with the design of canonical lenses, thus showing the capability of the approach to realize antennas other than canonical solutions. Then, the design of an antenna generating an optimal Σ/Δ reconfigurable pattern has been carried. The achieved results confirm the effectiveness of the proposed GAMs synthesis strategy, which outperforms the more straightforward and intuitive homogenization procedure.

In it worth to stress that all the above inverse scattering-based tools are not restricted to the realization of 'canonical' fields, and that they can be applied to generic (physically feasible, see [17]) field specifications.

4

SYNTHESIS OF CLOAKING DEVICES

4.1 Motivation and state of the art

The concept of invisibility always had great interest. From mythology it is said about heroic deeds accomplished thanks to special objects making the hero *disappeared*, thus allowing him to mislead the enemy and launch the winning attack.

The current idea of making objects (and not people!) invisible is pursued by several research groups around the world, since it has been observed that is is possible to achieve anomalous transparency effects, or "hide" a given object, making it effectively invisible to the electromagnetic radiation, by means of ad-hoc materials [159]. In military scenarios such a reduction of 'observability' has been performed through camouflage techniques inspired by nature observing (e.g., chameleons and squids). However, they often create undesired shadows that can reveal the presence of the object to hide or do not allow the signals to pass through (or around) the object, revealing, thus, its presence. In addition to radar detection, defense and military applications, invisibility concept has been proposed to improve near-field sensors, detectors and communication technologies requiring low levels of interference and noise [159, 160].

In this respect, the new concept of *invisibility cloaking* has been recently proposed. A *cloak* is a device capable of minimizing the field scattered and absorbed by an illuminated object.

A first experimental verification of the phenomenon occurred in 2003. Only two years later, Alù and Engheta developed the well-known "scattering cancellation" (SC) or Plasmonic Cloaking theory [161]. As qualitatively shown in fig.4.1, the SC explains how the invisibility of a dielectric object can be achieved by covering it with a volumetric material (*cloak*), such that the positive polarization of the dielectric and the negative polarization of the cloak are balanced and a cancellation effect is induced on

the scattered field [161]. Starting from this new concept, a number of papers concerning invisibility by means of plasmonic cloaks have been published [162–166].

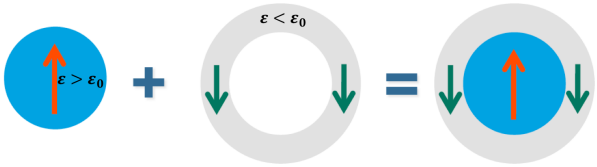

Fig. 4.1. Scattering Cancellation: a schematic interpretation of the transparency phenomenon.

A number of comments can be derived from the above discussions. First of all, it is worth to note that, by paying the price of becoming object-dependent, the plasmonic approach simplifies cloaking and allows to achieve some bandwidth for the devised cloak [161, 167]. Second, according to the degrees of freedom of scattered fields, the number of relevant scattering harmonics grows up with the size of the objects, so that the cancellation of low order harmonics is paid by the arising of higher order harmonics. As a consequence, the applicability of the method in case of objects that are large compared to the wavelength is quite cumbersome and for this reason practical implementations have been proposed under a quasi-static limit approximation [161, 167]. Last, but not least, the cancellation effect induced on the scattered field entails a null average value for the contrast function [116,161,163], so that artificial materials exhibiting properties which do not exist in nature (i.e., having contrast values lower than zero at the frequencies of interest) have to be involved as cloaks.

Beyond the plasmonic theory, in 2006 a new architecture scheme for design invisibility devices (based on the invariance of the Maxwell equations) has been introduced by Pendry and co-workers under the name of "coordinate transformation" or "transformation optics" (TO) theory [125, 168]. The TO is able to exclude fields from the interior of an invisible system while bending the radiation just outside. Interestingly, the invisibility device is object independent, as any object located in the excluded region of the space will be invisible. Unfortunately, the price to pay is that the constitutive parameters of coats should change continuously point by point and require the cloaking material to be inhomogeneous and strongly anisotropic. The schematic representation of such a behavior is shown in fig.4.2. Note that the effect yielded by TO is similar to the 'mirage', where a region of the space becomes invisible to the observer, due to the gradient of the refractive index of the atmosphere. Similarly, a suitable gradient on the cloak can bend the rays path such that they do not cross

the center region. By referring to fig.4.2, it is possible to guess that in order to preserve the phase, waves must travel faster than light within the cloak material, i.e., a superluminal propagation is required. Applicability of such a concept for invisibility purposes can be found in [169–172].

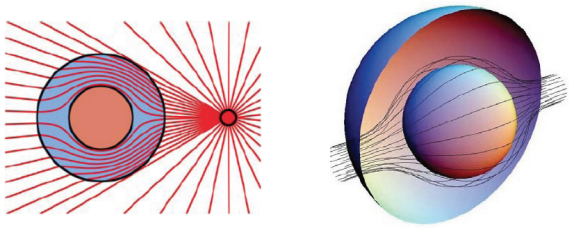

Fig. 4.2. Transformation Optics: a schematic interpretation of the transparency phenomenon.

In this thesis, the design of invisibility devices is pursued by exploiting inverse scattering methodologies. The idea has been recently explored in [136, 137] and very few contributions can be found in literature [173–175]. Note that it is either simpler with respect to TO, and more performing in some sense with respect to SC. In particular, inverse scattering is a more flexible tool since it allows to assign invisibility constraints of different kinds (by admitting, for instance, field delays) and/or on arbitrary surfaces (see the following); moreover, the approach could be easily extended to the case of objects embedded in media different from vacuum.

As a first contribution, theoretical arguments on invisibility, as well as possible procedures, are proposed starting from the spectral analysis introduced and discussed in Section 2.3. Then, in Section 4.3 the inverse scattering formulation is turned into a design problem by enforcing null scatterd field and cloaking system made up of bulk materials. Moreover, the synthesis of dielectric inclusions realizing invisibility is pursued in Section 4.4 as an innovative way to obtain artificial materials needed to actually realize the devices at hand. Finally, the flexibility of the inverse scattering based design tool is exploited in the last Section to achieve a '*quasi-invisibility*' behavior.

4.2 Invisibility within approximated models: spectral solutions

As already stressed, one of the main difficulty when dealing with the solution of an inverse scattering problem is the non linearity, so that approximation strategies can

be eventually adopted to overcome such a drawback (but paying the price of a limited range of validity).

By referring to the above mentioned strategies, a deepening into the spectral interpretation of some common approach has been proposed in Section 2.3 by paralleling the results derived for the well-known BA. Just to recall the key points, the analysis has been performed to extend the Ewald's sphere concept concerning the BA to other types of approximated approach, such as EBA, CS-EBA and SPFA.
By referring to fig.2.2, it was found that for any scattering experiment, the scattered field is related to the spatial Fourier transform of the auxiliary unknown function, involved in the approximation at hand, over the surface of a single Ewald sphere.

Interestingly, such a circumstance can be conveniently used in case of invisibility problems. As a matter of fact, when an invisibility condition is looked for, the aim is to cancel out the scattered field from an object by cloaking it with a properly designed cloak. Therefore, the pictorial representation in fig.2.2 can be renewed as in the following fig.4.3; namely, if the spectral content of the auxiliary unknown is null inside the Ewald sphere, the arising scattering field will be null as well.

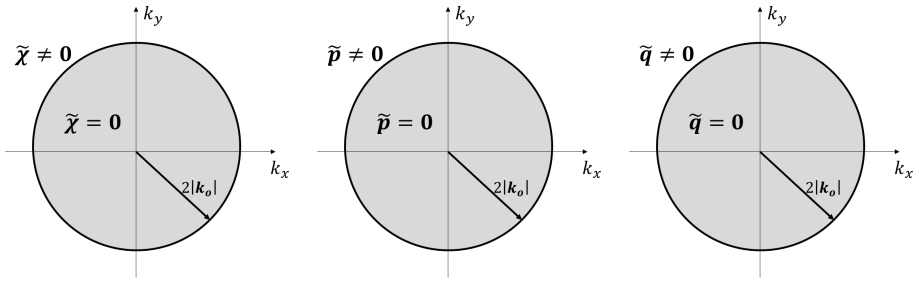

Fig. 4.3. Pictorial view of the spectral meaning of the approximated inverse scattering problem for invisibility conditions: (a) BA ($\tilde{\chi} = \mathscr{F}[\chi]$), (b) CS-EBA (and also EBA) ($\tilde{p} = \mathscr{F}[p]$) and (c) SPFA ($\tilde{q} = \mathscr{F}[q]$).

Consequently, by following these simple arguments it could be possible, at least in principle, to reach invisibility conditions for each scattering experiment.

Quite interestingly, the condition depicted in fig.4.3(a) includes the result [116] by Labate and co-workers (which includes in turn the SC formula (10) in [161], particularized for the TM case) as special cases. As a second interesting consideration, let us note that conditions depicted in figs.4.3(a), or 4.3(b), or 4.3(c), can be eventually implemented in a simple fashion. In fact, by considering by the sake of simplicity the

case in fig.4.3(a), the design of an invisibility cloak can be developed by following at least two different procedures.

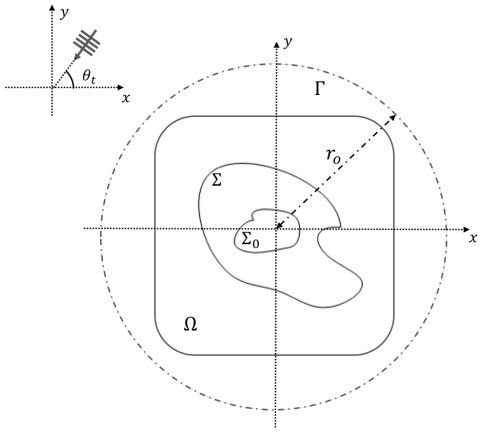

Fig. 4.4. Geometry of the problem for the synthesis of dielectric cloaking: Ω is the computational domain which includes an arbitrarily shaped scattering system made by the object to hidden ($\chi_0 \in \Sigma_0$) and the cloaking region ($\Delta\chi \in \Sigma$), while Γ is the observation region.

Let χ_0 be the contrast function of the (lossless) object to be hidden, and $\Delta\chi$ the contrast function pertaining to the (unknown) cloak, see fig.4.4. Obviously, the two functions have distinct supports (say Σ_0 and Σ), and the total scattering system is characterized by $\chi = \chi_0 + \Delta\chi$. Then, if $\tilde{\chi} = \mathscr{F}[\chi]$, a first straightforward approach for invisibility, leading to the minimization of a quadratic function, would be:

Find $\Delta\chi$ *such that* :

$$\int\int_{k_x^2+k_y^2 \leq 4k_b^2} |\tilde{\chi}(k_x, k_y)|^2 dk_x dk_y \qquad \textit{is minimum} \quad (4.1)$$

A second simple possibility deals with the exploitation of the 'alternate projections' method [176], that relies on the iterative projection of the unknown function $\chi_0 + \Delta\chi \in \mathcal{R}^2$ into the Fourier domain in which all the components belonging to the circle of radius $2k_b$ are forced to be zero. A schematic representation of the method is shown in fig.4.5.

A first proof of concept has been performed by exploiting the 'alternate projections' approach and considering the small circular object depicted in fig.4.6(a) with a varying permittivity profile from 1.3 to 1 and radius $0.12\lambda_b$. The investigation domain is $1.5\lambda \times 1.5\lambda$ large, with λ the wavelength in the free space at $f = 300$ MHz, and it has been discretized into 64×64 square cells. The radius of the circular cloaking region Σ has been set equal to 0.6λ and $\Delta\chi = 0.1$ for the starting point of the

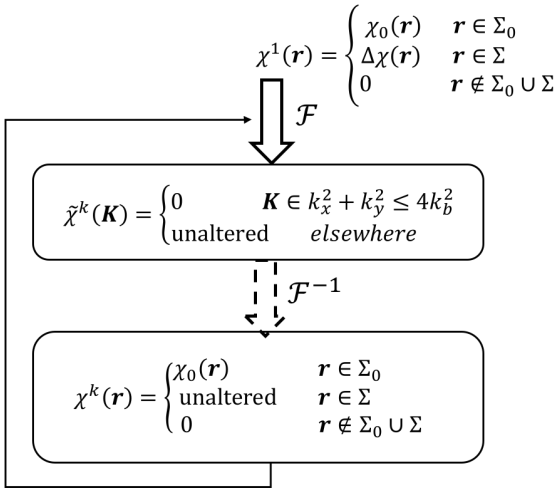

Fig. 4.5. Schematic representation of the 'alternate projections' synthesis approach.

iterative procedure. The synthesized profile achieved after 20 iterations is shown in fig.4.6(b). As it can be seen, the Fourier transform of this latter satisfies the expected properties, namely the alternate projections iteratively get out the dominant Fourier harmonics of the circle of radius $2k_b$, see figs.4.6(c)-4.6(d). Accordingly, the field scattered from the so-obtained cloaking system is reduced with respect to the bare case, see fig.4.6(e)-4.6(f).

The second and more complex example deals with the system of three circular objects depicted in fig.4.7(a). The radius of the cylinders and their permittivity values are the same and equal to 0.12λ and 1.3, respectively, while the parameters for the cloaking region Σ have been considered as for the previous example. The synthesized profile is shown in fig.4.7(b). From the scattered field in a larger investigation domain depicted in fig.4.7(f) it is possible to appraise the effectiveness of the procedure, since a strong reduction of the field with respect of the bare case (fig.4.7(e)) has been achieved $\forall \boldsymbol{r} \notin \Sigma \cup \Sigma_0$. Accordingly, differently from the bare case, the spectral content of the synthesized cloaking system is mainly outside of the so-called Ewald sphere, see figs.4.7(c) and 4.7(d).

The above results as well as the preliminary results achieved with the other procedure confirm the effectiveness of both methods, even if further numerical examples and checks are still needed at the time this thesis is being written.

Note that similar approaches can be developed under the CS-EB or SPF approximations and that further properties can be eventually enforced on $\Delta\chi$ (and the like) in both approaches. Obviously, in each case one has to also check/enforce the validity of the corresponding approximation.

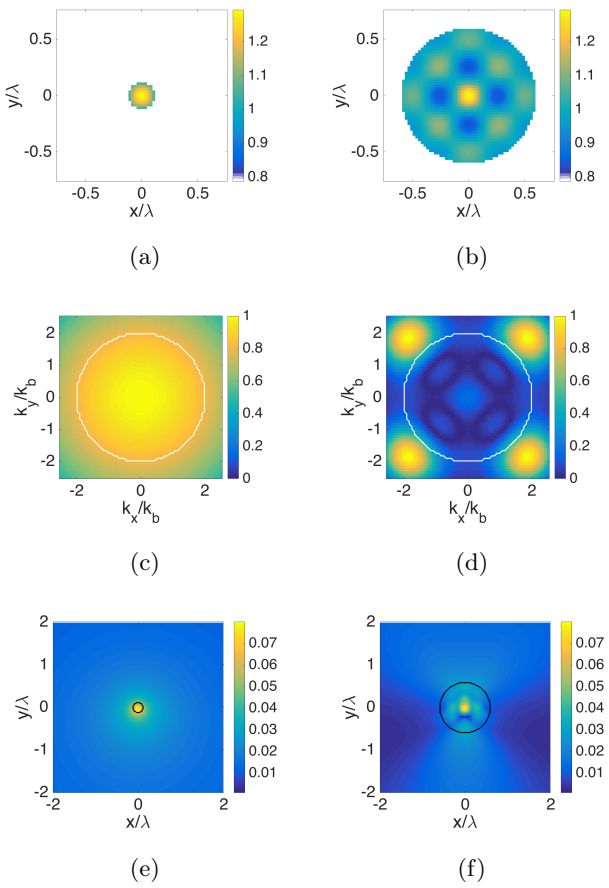

Fig. 4.6. Spectral invisibility via 'alternate projections' approach: a circular object. Permittivity function of the (a) bare and (b) synthesized profile. Fourier transform of the (c) bare object ($\tilde{\chi_0}$) and of the (d) synthesized cloaking system ($\tilde{\chi}$); the white contour line represents the Ewald sphere with radius $2k_b$. Scattered field from the (e) bare and (f) cloaking system on a larger domain with superimposed the contour line of the object.

As a final comment, let note that, as in the corresponding retrieval problems, the Compressive Sensing (CS) tools can be useful for the design problem at hand. As a matter of fact, the Fourier relationship between the scattered fields and the auxiliary unknown function entails that some peculiar properties of CS such as RIP, incoherence and the like are automatically satisfied (see [43, 65]), so that the design of 'sparse' invisibility devices by exploiting the above discussed spectral analysis can be pursued. Such a topic will be object of future developments as well.

4.3 'Full invisibility' via inverse scattering methodologies

The determination of the constitutive parameters of a coat by means of inverse scattering methodologies deals with the problem sketched in fig.4.4. By referring to such

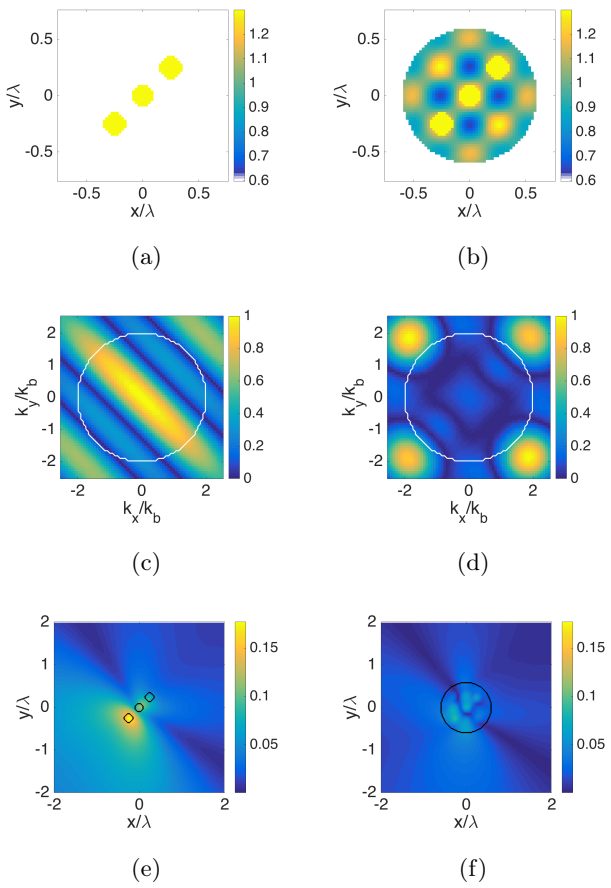

Fig. 4.7. Spectral invisibility via 'alternate projections' approach: three circular objects. Permittivity function of the (a) bare and (b) synthesized profile. Fourier transform of the (c) bare object ($\tilde{\chi_0}$) and of the (d) synthesized cloaking system ($\tilde{\chi}$); the white contour line represents the Ewald sphere with radius $2k_b$. Scattered field from the (e) bare and (f) cloaking system on a larger domain with superimposed the contour line of the object.

a scenario, the basic state equation of the inverse scattering problem introduced in eq.(1.4) is recast as:

$$W(\boldsymbol{r},\boldsymbol{r}_t) = \chi_0(\boldsymbol{r})E_i(\boldsymbol{r},\boldsymbol{r}_t) + \chi_0(\boldsymbol{r})\mathcal{A}_i[W(\boldsymbol{r},\boldsymbol{r}_t)] + \Delta\chi(\boldsymbol{r})E_i(\boldsymbol{r},\boldsymbol{r}_t) + \Delta\chi(\boldsymbol{r})\mathcal{A}_i[W(\boldsymbol{r},\boldsymbol{r}_t)], \qquad \boldsymbol{r}\in\Omega, \boldsymbol{r}_t\in\Gamma \tag{4.2}$$

while the data equation keeps the same:

$$E_s(\boldsymbol{r}_o,\boldsymbol{r}_t) = \mathcal{A}_e[W(\boldsymbol{r},\boldsymbol{r}_t)], \quad \boldsymbol{r}\in\Omega, \boldsymbol{r}_o,\boldsymbol{r}_t\in\Gamma \tag{4.3}$$

The invisibility constraints can be imposed on Γ in the same way as for the radiation problem dealt in the previous chapter. Therefore, the solution of eqs.(4.2)-(4.3) can be still faced with the CSI method. Accordingly, the cost functional involved in the CSI is turned as follows:

$$\begin{aligned}\Phi(W,\Delta\chi) &= \sum_{v=1}^{T}\frac{\left\|\mathcal{A}_e\left[W^{(v)}\right]-E_s^{(v)}\right\|_2^2}{\left\|E_i^{(v)}\right\|_2^2}\\ &+\sum_{v=1}^{T}\frac{\left\|\chi_0\mathcal{A}_i\left[W^{(v)}\right]+\chi_0E_i^{(v)}+\Delta\chi\mathcal{A}_i\left[W^{(v)}\right]+\Delta\chi E_i^{(v)}-W^{(v)}\right\|_2^2}{\left\|E_i^{(v)}\right\|_2^2}\end{aligned} \tag{4.4}$$

wherein the explicit definition for the operators $\mathcal{A}_i$ and $\mathcal{A}_e$ can be found in eqs.(1.4)-(1.5). Notably, since in an invisibility problem the goal is to reach null scattered field from the system under investigation, the first addendum is normalized with respect to the incident field E_i.

In order to generalize the approaches in [136, 137], it is possible to take advantage of the skills and facilities developed in Chapter 3, as well as to consider additive penalty terms to the cost functional $\Phi(W,\Delta\chi)$. In particular, by supposing to look for circularly symmetric cloaks[1], the optimization problem employed in the following reads:

$$\min_{W,\Delta\chi}\Phi'(W,\Delta\chi)=\Phi+w_f\left\|\Delta\chi-f(\Delta\chi)\right\|_2^2+w_s\left\|\frac{\partial\Delta\chi}{\partial\theta}\right\|_2^2 \tag{4.5}$$

in which the second term at the right hand side can be eventually removed, $f(\Delta\chi)$ is the projection of $\Delta\chi$ into the set of real and positive functions, θ is the angular coordinate of the polar reference system, while the positive w_f and w_s coefficients allow to properly weigh the regularization terms with respect to the original ones.
Note that the novel set of unknowns τ introduced in Section 3.2 are not considered in this case, since we do not have any degree of freedom about impinging waves. Hereinafter, plane waves $E_i(\boldsymbol{r})=e^{-j\boldsymbol{k_b}\cdot\boldsymbol{r}}$ are supposed as incident fields.

It is worth to explicitly note that formulating the invisibility problem as in (4.4) allows to understand since from beginning the actual limitations of cloaking devices when excluding non superdirective contrast sources. In fact, scattered fields are nothing else than the fields radiated by the contrast sources, and, as such, are subject to given properties in terms of spatial bandlimitedness as long as the contrast sources are not superdirective [18, 134]. Notably, non superdirective contrast sources are required as soon as some bandwidth is required to the device looked for.

In this section, a *full-invisibility* condition is pursued, namely the design constraint results into canceling the scattered field, in such a way that the impinging plane wave can be detected unperturbed beyond the object whatever the impinging direction. In formulas:

[1] which is of interest for circularly symmetric object to be hidden

full-invisibility condition

$$E(\boldsymbol{r}_t, \boldsymbol{r}_o) = E_i(\boldsymbol{r}_t, \boldsymbol{r}_o) \qquad \Longrightarrow \qquad E_s(\boldsymbol{r}_t, \boldsymbol{r}_o) = 0 \tag{4.6}$$

The numerical simulations have been performed by considering the same target in [137], in which the inverse scattering problem has been solved by applying the CSI method to the standard cost functional (4.4). Moreover, by referring to the weighted cost functional (4.5), w_s has been chosen roughly equal to the side of the discretization pixel, while w_f has been set equal to the area of the cloaking region.

By referring to a free space background, the object to cover is a circular scatterer made up of lossless allumina ($\varepsilon_r = 10$) whose radius is 0.42 cm ($\simeq 0.35\lambda$ at $f = 25$ GHz), while the radius of the cloak is set equal to $b = 1.2$ cm (i.e., 1λ). According to [108], when a GRIN coat is looked for, the step size of the unit cell for the discretization of Ω has been set to 0.5 mm. As a consequence, 48×48 pixels have been considered in this case. Since the cloaking effects is required all around the cloak (full-aspect invisibility) the scattered field has been forced to be zero in 24 equispaced observation points located on a circumference Γ placed in the close proximity of the cloaking system with radius $r_o \simeq 1.45b$. Note that the number of these points is linked to the number of DoF of the scattered field [17]. The initial guess of the dielectric cover has been set as homogeneous in the whole Σ with relative permittivity equal to 4.5. The permittivity function of the bare object, as well as the total field it generates on the domain are depicted in fig.4.8.

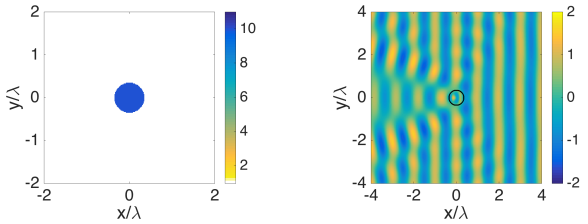

(a) (b)

Fig. 4.8. *Full-aspect invisibility* for cylindrical object. (a) Permittivity function of the bare object and (b) real part of the total field for $\theta_t = 0°$ on a larger domain with superimposed the contour of the bare object as a black line.

The cloaking system resulting from minimization of $\Phi'(W, \Delta\chi)$ is shown in fig.4.9(a), while in fig.4.9(b) the real part of the total field on a larger domain Ω is depicted for the direction of arrival of the plane wave $\theta_t = 0°$ (i.e., from the right side). As is can be observed, the synthesized plasmonic cover is in cloaking opera-

tion with the flat phase fronts well recognizable behind the object and, thanks to the circular symmetry of the dielectric profile, this holds for any arrival direction.

In order to further reduce the complexity of the electromagnetic parameters for the coat, one more penalty term has been added to $\Phi'(W, \Delta\chi)$ that allows to attain a radially smoother dielectric profile; this reads as $\Phi_{\rho_2}(\Delta\chi) = w_\rho \left\| \frac{\partial \Delta\chi}{\partial r} \right\|_2^2$, wherein it has been set $w_\rho = 10^{-12}$ to make Φ_{ρ_2} not overwhelming with respect to the other terms. The resulting dielectric coat is shown in fig.4.9(c) and it still allows to attain invisibility, as demonstrated by the constant phase fronts of the total field in fig.4.9(d).

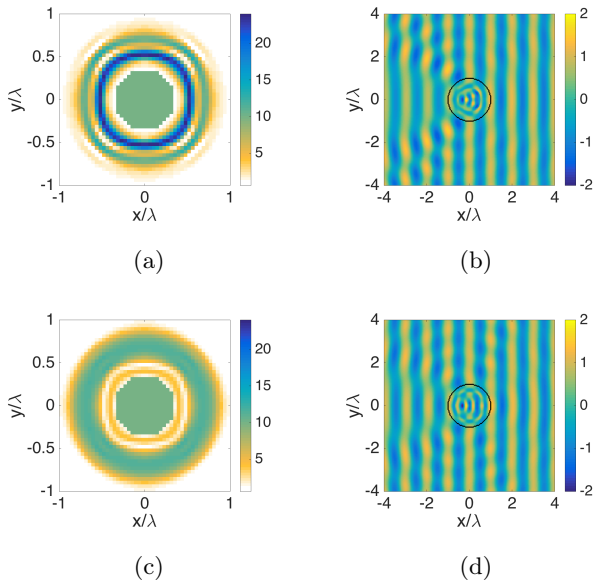

Fig. 4.9. *Full-aspect invisibility* for cylindrical object. From top to bottom: features of the GRIN cloaking system in case of circular symmetry ($w_s = 10^{-4}, w_f = 4 \cdot 10^{-4}$) and circular symmetry in conjunction with smoothness ($w_\rho = 10^{-12}$) penalty terms. (a)-(c) Synthesized permittivity function and (b)-(d) real part of the total field on a larger domain, on which the contour of the cloaking system is superimposed as a black line.

As a final comment, it is worth to note that the achieved cloaking systems employ all 'natural' materials and hence the invisibility condition can be reached without resort to metamaterials. Moreover, let us also note that even if we limited ourselves to objects having a circular symmetry, the developed approach and tools have a general validity, and no symmetric objects (and cloaks) could be easily dealt with (see the following).

4.4 Graded Artificial Material invisibility devices

In the previous Section, it has been demonstrated how the exploitation of inverse scattering methodologies and the extension of the approaches developed in Sections 3.2-3.3 yield good performances in designing plasmonic GRIN invisibility cloaks.

On the other side, contents of the previous Sections also emphasize two relevant drawbacks of such a solution. The first, and more obvious one, is related to the fact that one has to realize these continuous profiles, which could be eventually be done by some ad-hoc bulk materials organized into proper shells. But, then, a second difficulty comes into play. In fact, the spectral analysis of Sect.4.2 (as well as the result is [116, 161]) implies that in many cases one needs materials having $\chi < 0$, and one cannot find them in a bulk form. Hence, one has to recur to alternative strategies in order to realize some kind of artificial dielectrics.

By taking advantage from the tools and discussions of Chapter 3, a possible way to proceed is to exploit the same strategies as the ones introduced for the design of antennas [177]. Hence, by still looking at circularly symmetric dielectric profiles, so that a kind of 'full-aspect' invisibility could be achieved, the pertaining expansion for the unknown contrast function of the cloak reads as follow:

$$\Delta\chi(\boldsymbol{r}) = \sum_{k=1}^{K} \Delta\chi_k \sum_{h=1}^{H_k} \Pi_{kh}\left(\frac{\boldsymbol{r}-\boldsymbol{r}_{kh}}{a_k}\right), \quad \boldsymbol{r} \in \Omega \setminus \Sigma_0 \tag{4.7}$$

in which $\Delta\chi_k$ is the contrast value associated to the k-th ring of rods, K is the total number of the rings for the arrangement of the rods, H_k is the number of inclusions along the k-th ring, $\boldsymbol{r}_{kh}$ is the position of the center of the h-th rod belonging to the k-th ring, and $|\boldsymbol{r}_{kh}| = r_k$. Also in this case, the internal summation defines a composite window which is different from zero in each rod belonging to the k-th ring, and zero elsewhere.

As long as the expansion (4.7) is adopted in the minimization of the cost functional $\Phi(W, \Delta\chi)$, the synthesized cloak will be made up by rods arranged on K rings and, each of them, will exhibit a different permittivity value. As a consequence, the CSI method in conjunction with the expansion (4.7) give rise to the so-called GAM_R invisibility cloak system. Moreover, the original interchanging methodology developed in Section 3.5.2 can be still adopted in order to obtain a GAM_F invisibility system from the GAM_R one [177]. Clearly, such a possibility allows to look at more practical realizations of the invisibility devices, since a single material with permittivity ε_F is involved for the cloak.

The effectiveness of the GAMs synthesis procedure is demonstrated developing two different solutions (where the first one also acts as an input to the second). First,

the design of a GAM_R is tackled for different arrangements of the rods. In particular, the same structure shown in fig.3.11 is adopted in Σ and a numerical study has been performed by varying the number of rings K, periodicity of the unit cell d and the radius of rods. Then, the interchanging procedure is applied to design equivalent GAM_F invisible cloaks for different materials (i.e., ε_F).

By referring to the same object in fig.4.8, as a first study it was considered a GAMs cloak with radius $b = \lambda$ and made up of $K = 4$ rings of rods with radius $a = \lambda/15$ arranged with a periodicity $d = \lambda/7$. The synthesized GAM_R invisibility system is shown in fig.4.10(a) and, as it can be observed from the field in fig.4.10(b), it makes the detection of the impinging plane wave unperturbed behind it. Starting from such a well-functioning device, the interchanging procedure has been applied to retrieve the equivalent GAM_F invisibility systems depicted in figs.4.10(c)-4.10(d) when $\varepsilon_F = 5.5$ is chosen, and in figs.4.10(e)-4.10(f) for $\varepsilon_F = 10$ (note it is the same material of the object). In both cases, the incident field results unperturbed and no deterioration of performances with respect to the GAM_R case occurs.

In order to further reduce the complexity of the cloak's structure, a reduced number of rings has been defined ($K = 3$), while slightly increasing the dimension of the rods as well as the periodicity ($a = \lambda/11$, $d \simeq \lambda/5$). Interestingly, the synthesis procedure leads to a permittivity value equal to 1 for the inner ring, so that the overall GAM_R cloak is made up of 2 rings (see fig.4.11(a)), while providing excellent performances (see fig.4.11(b)). The same comment holds for the equivalent GAM_F cloaks in figs.4.11(c)-4.11(d) ($\varepsilon_F = 5$) and figs.4.11(e)-4.11(f) ($\varepsilon_F = 9$).

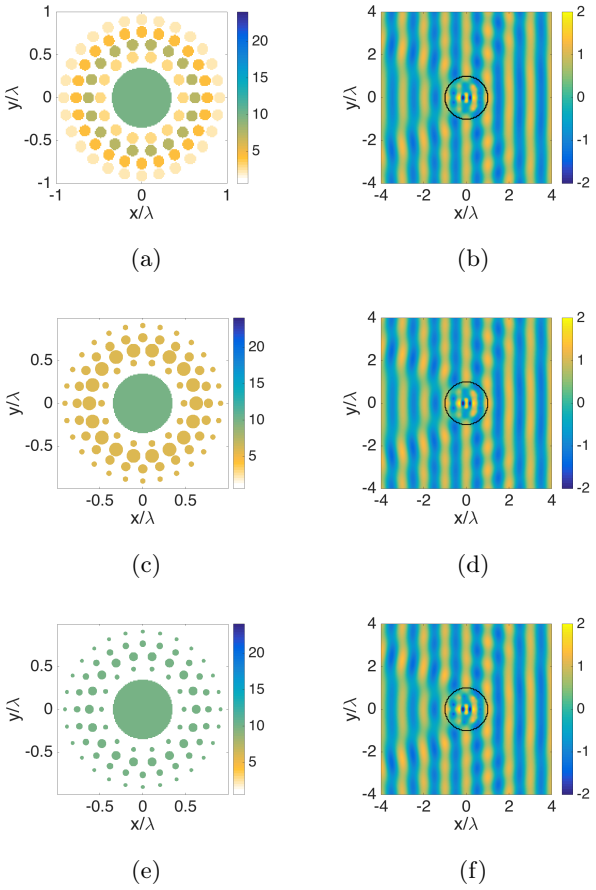

Fig. 4.10. *Full-aspect invisibility* for cylindrical object. From top to bottom: features of the GAMs cloaking system. On the left: synthesized permittivity function; on the right: real part of the total field on a larger domain with the contour of the system as a black line. Features and performances of (a)-(b) GAM_R with $K = 4$, $a = \lambda/15$ and $d = \lambda/7$ ($w_f = 1.3 \cdot 10^{-4}$); GAM_F for (c)-(d) $\varepsilon_F = 5.5$ and (e)-(f) $\varepsilon_F = 10$.

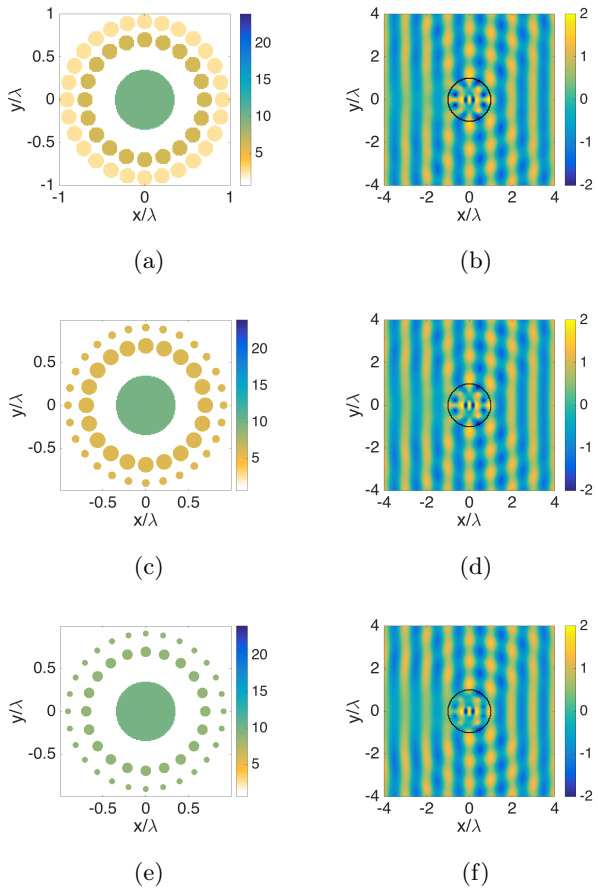

Fig. 4.11. *Full-aspect invisibility* for cylindrical object. From top to bottom: features of the GAMs cloaking system. On the left: synthesized permittivity function; on the right: real part of the total field on a larger domain with the contour of the system as a black line. Features and performances of (a)-(b) GAM_R with $K = 3$, $a = \lambda/11$ and $d \simeq \lambda/5$ ($w_f = 9.7 \cdot 10^{-5}$); GAM_F for (c)-(d) $\varepsilon_F = 5$ and (e)-(f) $\varepsilon_F = 9$.

4.4.1 Figures of merit and bandwidth performances

Appraising the results of the synthesized cloaks in terms of the total field generated in the investigation domain is not an unbiased method, since it only gives a *qualitative* analysis of the performances. In order to *quantitatively* appraise the results, the Figure of Merit (FoM) introduced in [163] is considered herein. In particular, it refers to the ratio between the *scattering cross-section* (SCS) of the bare and the covered object.

For the 2D problem at hand and for each given direction of arrival $\boldsymbol{r}_t$ of the plane wave, the SCS is defined as:

$$SCS(\boldsymbol{r}_t) = \frac{1}{2\pi|\boldsymbol{r}_o|}\sum_{o=1}^{N}\frac{|E_s(\boldsymbol{r}_t,\boldsymbol{r}_o)|^2}{|E_i(\boldsymbol{r}_t,\boldsymbol{r}_o)|^2} \tag{4.8}$$

$\boldsymbol{r}_o$ being the observation direction, while $|\boldsymbol{r}_o|$ is the radius of the (circular) observation curve.

Accordingly:

$$FoM = 10log_{10}(SCS_{bare}) - 10log_{10}(SCS_{obj+cover}). \tag{4.9}$$

Since the synthesized cloaks all exhibit a circular symmetry, a single direction of arrival $\boldsymbol{r}_t = 0$ has been considered for the calculation of the FoM[2], while $N = 72$ and $|\boldsymbol{r}_o| = 1.45b$ have been set for the observation points. In Table 4.1 are summarized the FoM relative to the examples above and they actually show the effectiveness of the synthesis procedure, i.e., the reduction of the SCS for the synthesized cloaks, in a quantitative fashion.

Table 4.1. Figures of merit for the synthesized cloaking devices.

Device	**FoM [dB]**
GRIN with circular symmetry (fig.4.9(a))	3.93
GRIN with circular symmetry and radial smoothness (fig.4.9(c))	4.36
GAM_R with $K = 4$ (fig.4.10(a))	5.47
equivalent GAM_F for $\varepsilon_F = 5.5$ (fig.4.10(c))	5.08
equivalent GAM_F for $\varepsilon_F = 10$ (fig.4.10(e))	4.75
GAM_R with $K = 3$ (fig.4.11(a))	2.74
equivalent GAM_F for $\varepsilon_F = 5$ (fig.4.11(c))	3.26
equivalent GAM_F for $\varepsilon_F = 9$ (fig.4.11(e))	2.74

Finally, the cloaking effect as a function of the frequency has been also analyzed. In particular, the SCS for each synthesized device has been calculated from 20GHz to

[2] The numerical value of the SCS when calculated for different directions of arrival does not substantially change.

30GHz with a step of 1GHz. In fig.4.12(a) it is shown a comparison between the GRIN and the GAM_R devices, while in fig.4.12(b) the GAM_R performances are compared to those of the relative GAM_F devices. As it can be seen, all the devices share the minimum at the design frequency of 25GHz and their SCS is actually reduced with respect to the bare case (black continuous line). Moreover, as expected, the frequency behavior of the GAM_F devices keeps almost unchanged with respect to the pertaining GAM_R profiles, thus confirming that the two structures can be considered similar.

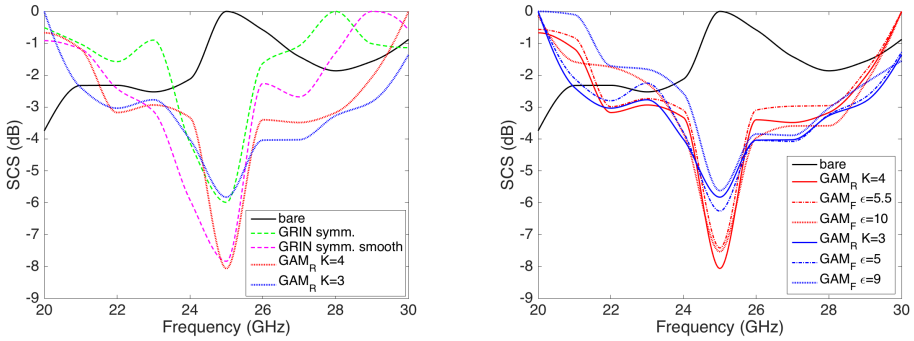

(a) (b)

Fig. 4.12. *Full-aspect invisibility* for cylindrical object. SCS calculated as a function of frequency for synthesized cloaks and comparison with the bare object.

4.5 'Quasi-invisibility' via inverse scattering methodologies

In all engineering applications (and beyond) relaxing requirements allow for an extended set of solutions, so that one can find solutions which are simpler or more convenient. This has been indeed the case by dropping the requirement for a universal cloak and looking instead for ad-hoc cloaks by means of SC or inverse scattering. This latter also has an extended flexibility with respect to SC as for as the geometry of the different scatterers is concerned. Along this line of reasoning, it is interesting to note that the general framework of inverse scattering also offers another possibility, which is the one of looking for "nearly invisible" objects, rather that for "exactly invisible" objects. In fact, inverse scattering can manage a number of situations of interest including "aspect-limited" invisibility (for example, just in Tx or Rx, or in a reduced set of angles), or situations where the scatterer is "quasi-invisible" (as discussed below), or any combination of the above.

In order to check for capabilities and performances, in the following different conditions for "*quasi-invisibility*" (QI) are considered, which turn into the design constraints reported below:

quasi-invisibility conditions

$$[QI\#1] \qquad E_s^{cloaked}(\boldsymbol{r}_t, \boldsymbol{r}_o) = c^2 E_s^{uncloaked}(\boldsymbol{r}_t, \boldsymbol{r}_o) \tag{4.10}$$

$$[QI\#2] \qquad E(\boldsymbol{r}_t, \boldsymbol{r}_o) = c^2 E_i(\boldsymbol{r}_t, \boldsymbol{r}_o) \tag{4.11}$$

$$[QI\#3] \qquad E(\boldsymbol{r}_t, \boldsymbol{r}_o) = E_i(\boldsymbol{r}_t, \boldsymbol{r}_o) e^{-j\alpha} \tag{4.12}$$

In particular, the $QI\#1$ is referred as a 'reduction of the transverse scattering cross-section', since it looks at a suitable cloak giving a percentage decay of the field scattered by the overall system with respect to the bare object. Conversely, the $QI\#2$ and $\#3$ aim at bring about a 'perturbation' of the incident field instead of cancel out the scattered field: the former turning into a drop of the energy of the field, the latter into a wave's delay. In both cases $QI\#2$ and $\#3$, the observer will still perceive the field as generated by the primary source (i.e., the unperturbed field) but for a reduction in amplitude and a delay, respectively. Note in both conditions one *is not* looking any more for $E_s = 0$.

In order to prove the effectiveness of the QI conditions, two different scenarios are considered in the following.

The first object is a circular cylinder, embedded in the free space, with diameter equal to 1λ, λ being the wavelength of the background at $f = 1$ GHz, while the dimension of the cloak's diameter is set to be 3λ. The discretization of the analysis domain has been fixed according to rules of the integral equation method (MoM) [108]; in particular, the side of the unit square cell has been set about equal to $\lambda_r/15$, λ_r being the wavelength with respect to the object ($\varepsilon_r = 2.3$), so that the entire domain $3\lambda \times 3\lambda$ large has been discretized into 70×70 cells. In order to possibly guarantee a 360-degree invisibility, a circularly symmetric cloak's profile is needed. To this end, the inverse scattering problem has been solved by considering the functional (4.5) with $T = 1$, by setting w_s equal to the area of the discretization cell. As far as the physical feasibility properties is concerned, at each iteration of the minimization of the CSI functional the negative contrast values have been forced to zero. Note that the starting point of the minimization procedure has been set by considering a permittivity distribution $\Delta\chi$ equal to the Maxwell fish-eye lens. Such a choice would allow to better encourage the rays' bending. The design constraints are imposed on a linear array Γ of 6 equispaced fictitious antennas located at $r_o \simeq 2\lambda$, just in front

of the direction of arrival of the plane wave, $\theta_t = 180°$. The considered object as well as the adopted measurement configuration are shown in Fig.4.13.

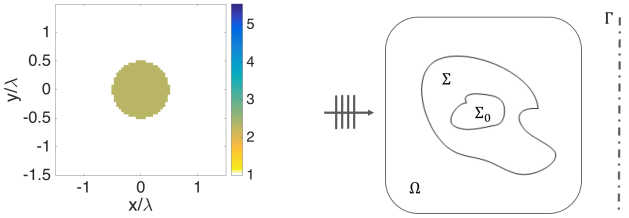

(a) (b)

Fig. 4.13. *Quasi-invisibility* for cylindrical object. (a) Permittivity function of the bare object. (b) Geometry of the adopted measurement configuration: the observation region Γ is a linear array at distance r_o from the origin of the reference system; the arrow on the left is the impinging plane wave from $\theta_t = 180°$.

In order to give a comparison in terms of convenience of the achieved solution, in fig.4.14(a) it is shown the synthesized cloak when the *full-invisibility* condition is attempted, while the corresponding radiated total field is reported in figs.4.14(b) and 4.14(c).

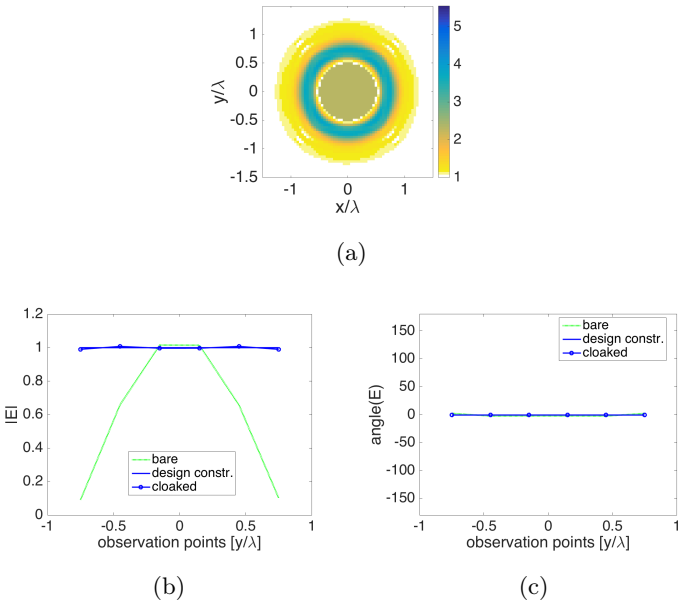

(a) (b) (c)

Fig. 4.14. *Quasi-invisibility* for cylindrical object. (a) Permittivity function of the synthesized cloak for a *full invisibility* requirement. (b) Magnitude and (c) phase of the radiated total field on Γ.

As first *quasi-invisibility* design constraint, the condition (4.10) is considered. In particular, the goal is to synthesize a coat allowing a reduction of 90% for the scattered field with respect to the bare case ($c^2 = 0.1$). The synthesized dielectric profile for the invisibility cloak is shown in Fig. 4.15(a). By comparing the magnitude and the phase of the scattered fields on Γ, respectively depicted in Fig. 4.15(c) and 4.15(e), it is possible to state that a 90% reduction of the scattering cross section is achieved by the coat at hand (marked blue line) with respect to the uncloacked object (continuous blue line).

The second design constraint deals with the condition (4.11). In this case, the goal is to synthesize a coat such that the detected total field arising from the cloaking system is almost the original incident field; in particular, a small perturbation (namely, a decreasing in its amplitude) is permitted ($c^2 = 0.9$). In Fig.4.15(b) the cloaking system arising from the minimization of functional (4.5), while forcing constraints (4.11), is reported. In order to verify the effectiveness of the $QI\#2$, the magnitude and phase of the total fields on Γ is plotted in Fig.4.15(d) and 4.15(f), respectively. As it can been seen, the synthesized cloak allows to perfectly reach the assigned specification.

Finally, the condition (4.12) is enforced in minimizing $\Phi'(W, \Delta\chi)$. Notably, $QI\#3$ entails an admissible delay in the propagation of the plane wave. The phase delay α in (4.12) has been set by spanning the angular circle. In fig.4.16 the achieved solutions are depicted for $\alpha = 70°$ (fig.4.16(a)), $\alpha = 220°$ (fig.4.16(b)), $\alpha = 250°$ (fig.4.16(c)) and $\alpha = 310°$ (fig.4.16(d)). As it can be observed, the synthesized cloaks are different from each other, but each of them satisfies the assigned specifications very well, see fig.4.16(e) and 4.16(f). Notably, some of the achieved cloaking systems are simpler with respect to solution in fig.4.14(a) and their practical realization would be more reasonable.

Moreover, it is possible to join conditions $QI\#2$ and $QI\#3$ in order to further relax the invisibility requirements. The synthesized cloaking systems for the same conditions of the previous case are shown in fig.4.17.

As a final comment, let us note that all the synthesized cloaks have (about) a 2λ diameter, while the Σ_1 region has been set to be a circle of radius 3λ. Therefore, inverse scattering allows to reach the assigned invisibility requirements with a coat even smaller that the given dimensions.

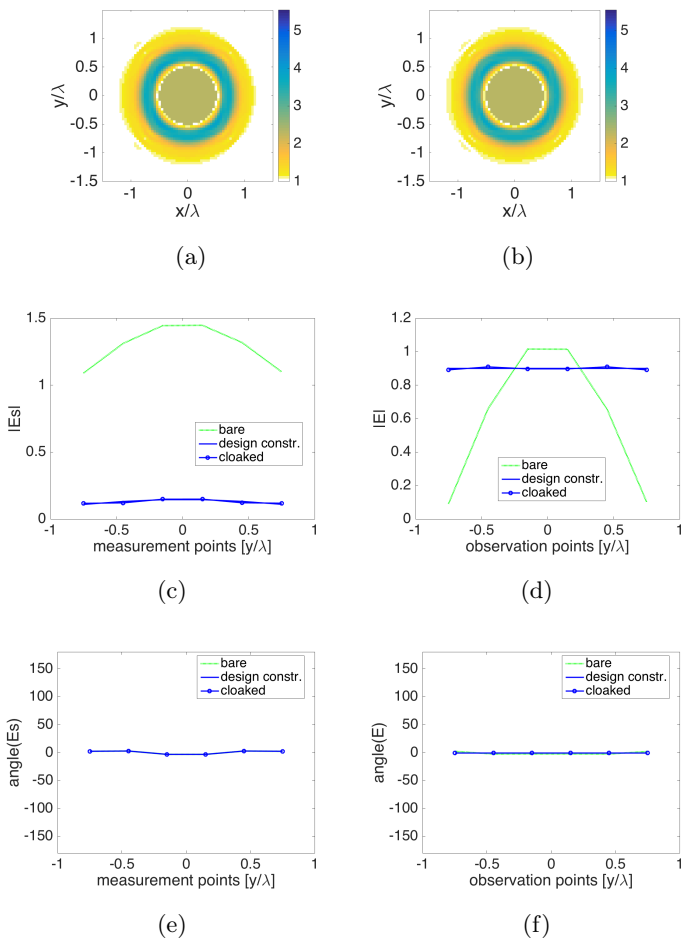

Fig. 4.15. *Quasi-invisibility* for cylindrical object. Features of the synthesized cloaking system for: $QI\#1$ on the left, $QI\#2$ on the right. From top to bottom: (a)-(b) permittivity function; comparison of the performances in term of magnitude and phase of the (c)-(e) scattered and (d)-(f) total field on Γ. The continuous blue line is the assigned design constraint, while the dotted green line and the marked blue line are the fields from the bare and cloaked object, respectively.

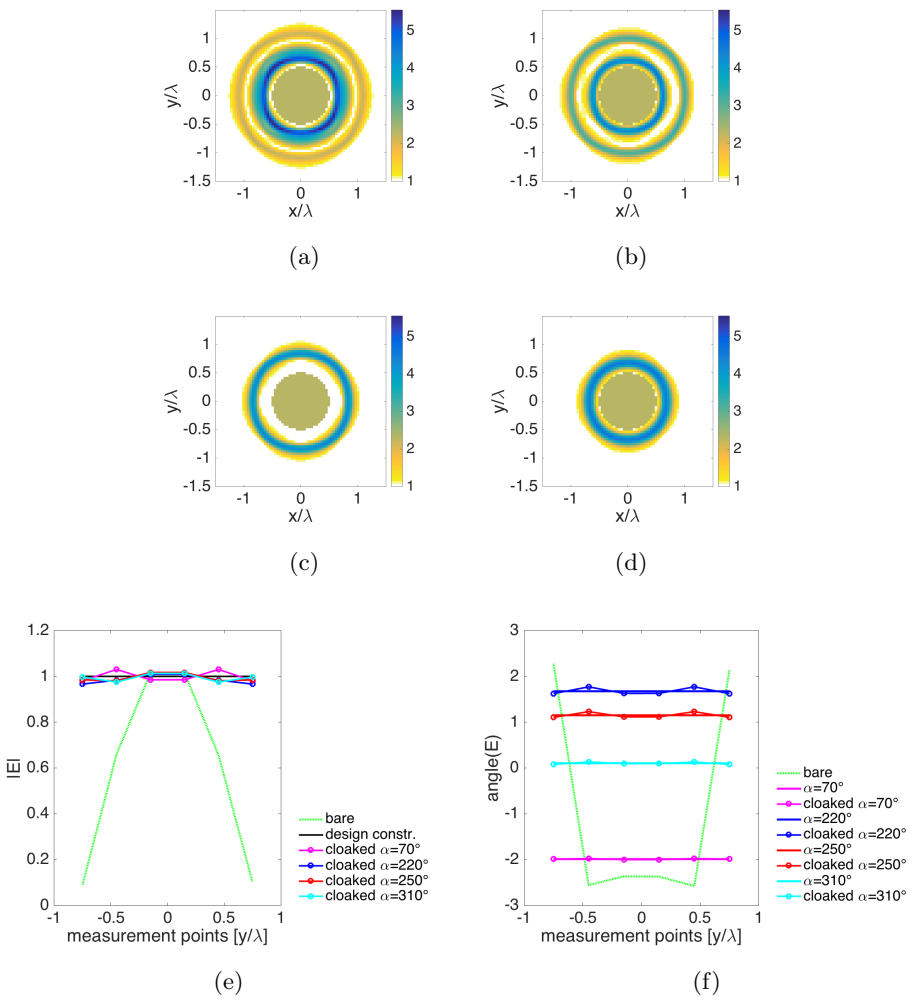

Fig. 4.16. *Quasi-invisibility* for cylindrical object. Features of the synthesized cloaking system for $QI\#3$. Synthesized permittivity function for (a) $\alpha = 70°$, (b) $\alpha = 220°$, (c) $\alpha = 250°$ and (d) $\alpha = 310°$. Comparison of the performances in term of (e) magnitude and (f) phase of the total field on Γ. The dotted green line is relative to the bare object, while the continuous and marked lines are relative to the assigned design constraints and the achieved solutions, respectively.

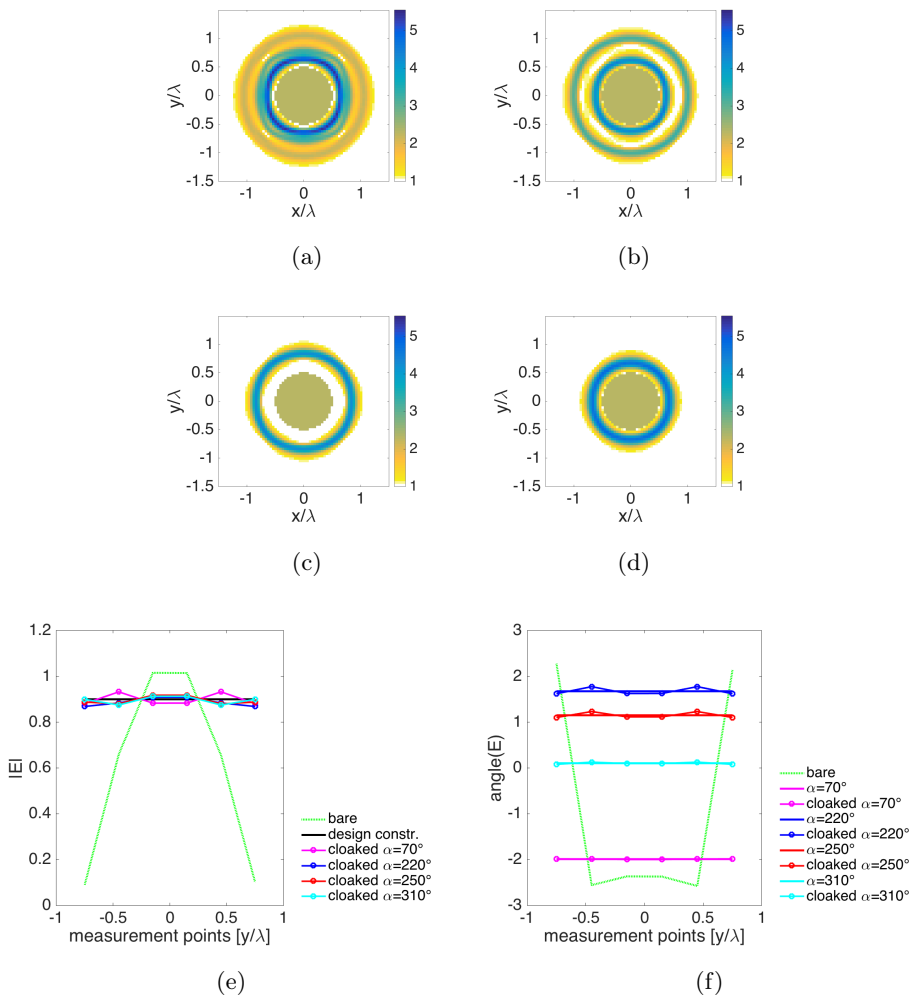

Fig. 4.17. *Quasi-invisibility* for cylindrical object. Features of the synthesized cloaking system for joint $QI\#2$-$QI\#3$. Synthesized permittivity function for (a) $\alpha = 70°$, (b) $\alpha = 220°$, (c) $\alpha = 250°$ and (d) $\alpha = 310°$. Comparison of the performances in term of (e) magnitude and (f) phase of the total field on Γ. The dotted green line is relative to the bare object, while the continuous and marked lines are relative to the assigned design constraints and the achieved solutions, respectively.

The second test case refers to the grid of square objects depicted in fig.4.18(a), with $\varepsilon_r = 2$ and whose leading dimension is about 1.5λ. The cover region is set to be a square of side 2λ, while the entire analysis domain is $3\lambda \times 3\lambda$ large. Following [108], it has been discretized into 90×90 square cells about $\lambda_r/20$ large. In this case, the minimization of $\Phi'(W, \Delta\chi)$ is pursued by considering $w_s = 0$, since no circular symmetry is required for the square cloak, while no physical feasibility constraints have been imposed. The design constraints (4.10)-(4.12) are assigned on 4 linear arrays, each of them made by 43 equispaced fictitious antennas, located at distance $r_o \simeq 2.10\lambda$ from the origin and in front of the impinging plane waves from $\theta_t = 0, 90°, 180°, 270°$, respectively, see fig.4.18(b).

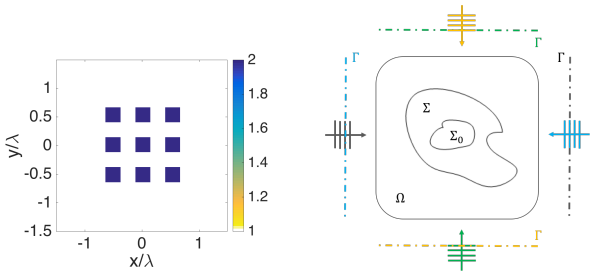

(a) (b)

Fig. 4.18. *Quasi-invisibility* for grid object. (a) Permittivity function of the bare object. (b) Geometry of the adopted measurement configuration: the observation region Γ is composed by four linear arrays at distance r_o from the origin of the reference system; the arrows represent the corresponding impinging plane waves from $\theta_t = 0°, 90°, 180°, 270°$.

The invisibility conditions to be reached by the synthesized devices have been set as for the previous example. In fig.4.19 the synthesized cloaking systems for $QI\#1$ (left) and $QI\#2$ (right) are shown. For the sake of brevity, it is shown only the field on Γ in front of the impinging plane wave from $\theta_t = 180°$. As in can be observed, the two solutions in fig.4.19(a) and 4.19(b) match very well the assigned design constraints, as demonstrated by the radiated scattered and total field, respectively, on the observation points, see figs.4.19(c)-4.19(e) and figs.4.19(d)-4.19(f). Notably, the achieved profiles are quite similar and therefore in this case inverse scattering allows to accommodate more than one requirement with essentially the same permittivity distribution.

Then, a numerical study has been performed in order to retrieve the performances of the cloaking systems under the condition (4.12) for different requirements on the phase delay. In particular, in fig.4.20 the results obtained for $\alpha = 10°$, $\alpha = 70°$,

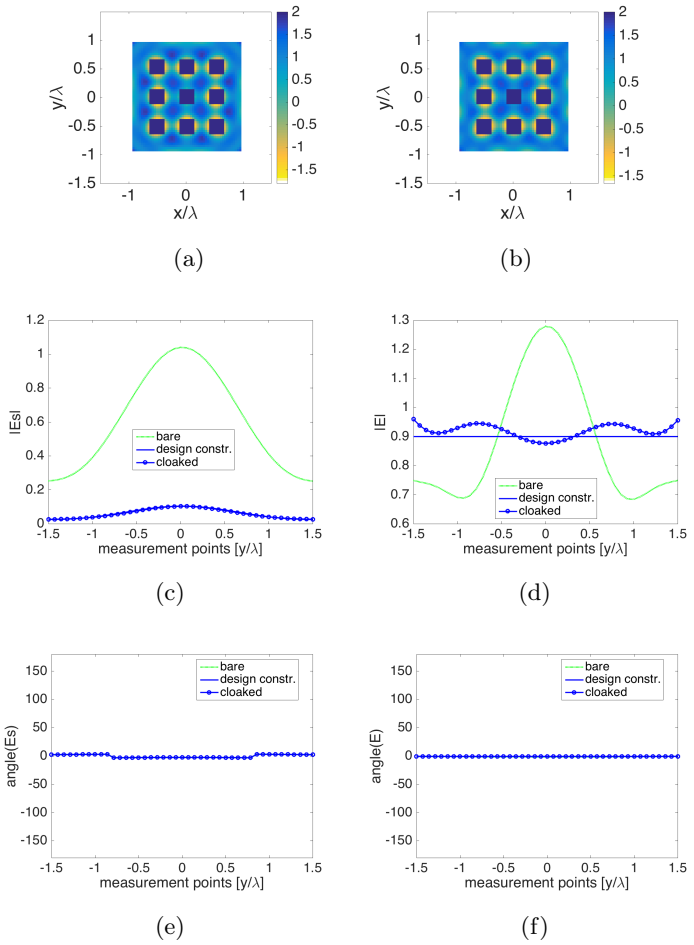

Fig. 4.19. *Quasi-invisibility* for grid object. Features of the synthesized cloaking system for: $QI\#1$ on the left, $QI\#2$ on the right. From top to bottom: (a)-(b) permittivity function; comparison of the performances in term of magnitude and phase of the (c)-(e) scattered and (d)-(f) total field on Γ. The continuous blue line is the assigned design constraint, while the dotted green line and the marked blue line are the fields from the bare and cloaked object, respectively.

$\alpha = 210°$ and $\alpha = 350°$ are shown. As it can be seen, the matching of the assigned specifications is quite good, even if power losses are present in some case.

Finally, in fig.4.21 are reported the results achieved when condition (4.12) is exploited in conjunction with condition (4.11). Also in this case, it is possible to observe a good matching of the design constraints.

In conclusion, it can be state that the inverse scattering procedures are suitable to design dielectric cloaks for canonical and non-canonical objects, which yield to *quasi-invisibility* behaviors and that work beyond the quasi-static regime. Note that results for the non-canonical scenario are just preliminary results and hence a detailed study

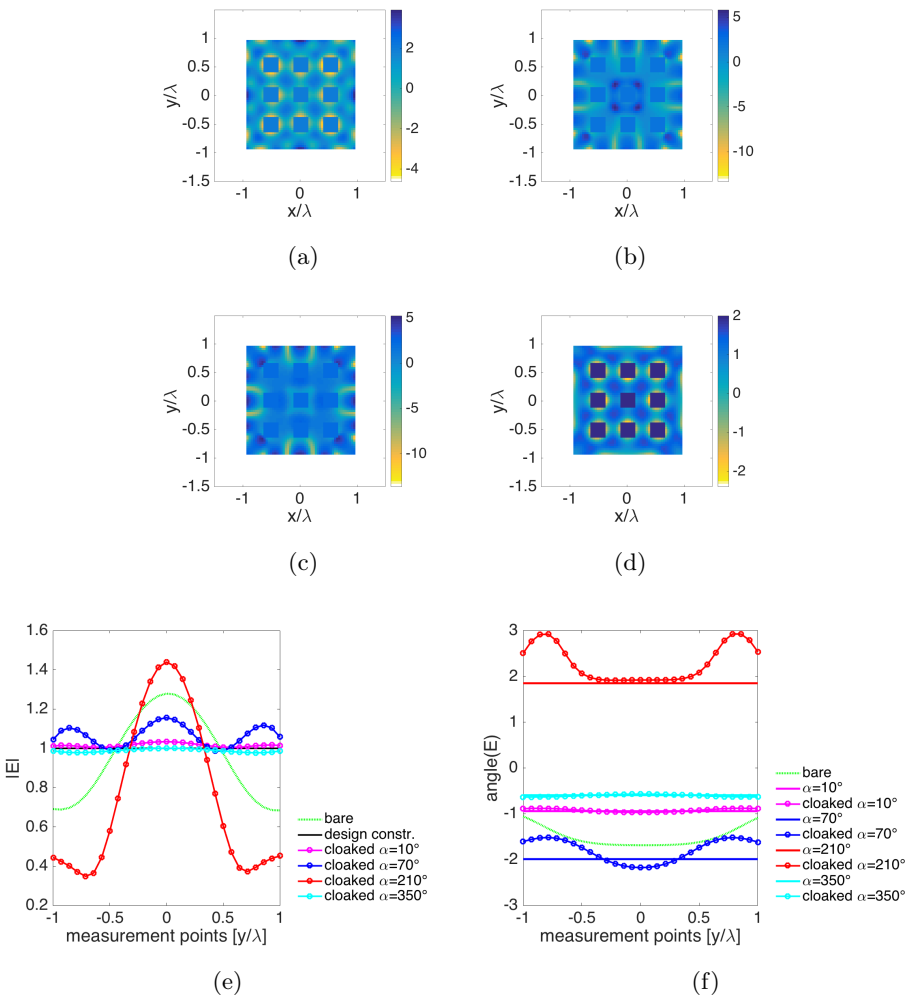

Fig. 4.20. *Quasi-invisibility* for grid object. Features of the synthesized cloaking system for $QI\#3$. Synthesized permittivity function for (a) $\alpha = 10^\circ$, (b) $\alpha = 70^\circ$, (c) $\alpha = 210^\circ$ and (d) $\alpha = 350^\circ$. Comparison of the performances in term of (e) magnitude and (f) phase of the total field on Γ. The dotted green line is relative to the bare object, while the continuous and marked lines are relative to the assigned design constraints and the achieved solutions, respectively.

on the actual performances of inverse scattering in dealing with such a case is an on going activity.

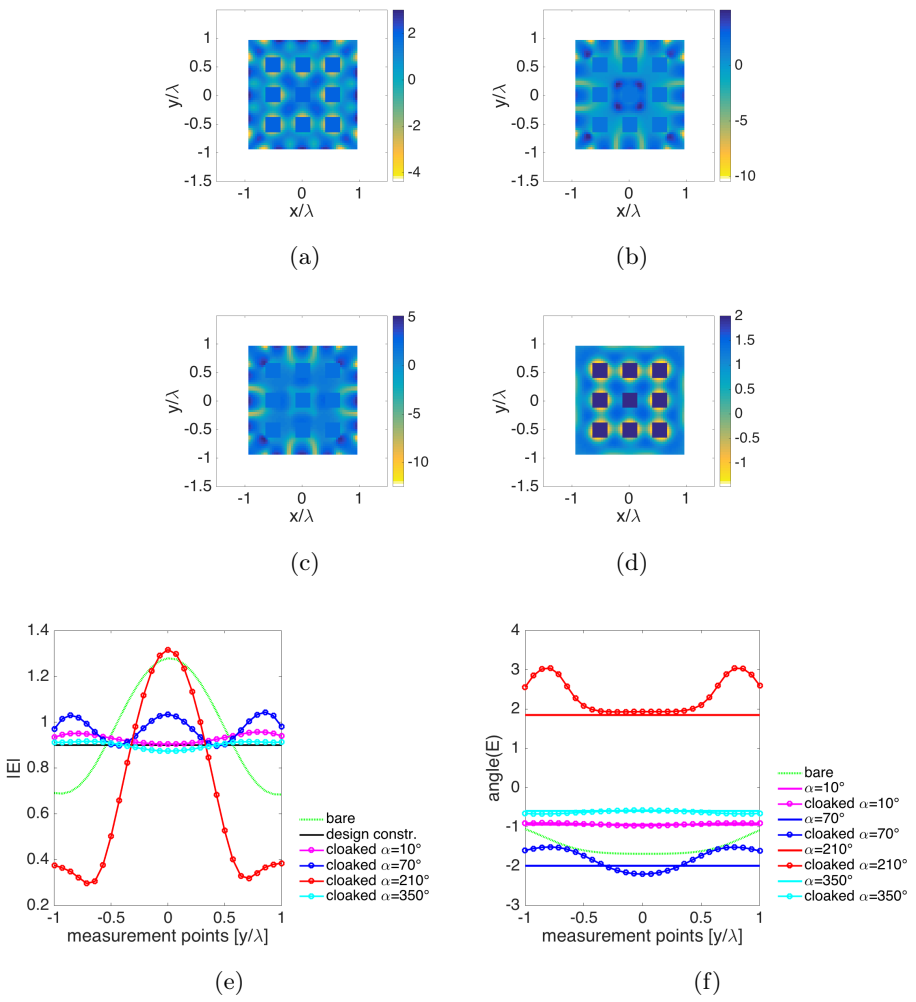

Fig. 4.21. *Quasi-invisibility* for grid object. Features of the synthesized cloaking system for joint $QI\#2$-$QI\#3$. Synthesized permittivity function for (a) $\alpha = 10°$, (b) $\alpha = 70°$, (c) $\alpha = 210°$ and (d) $\alpha = 350°$. Comparison of the performances in term of (e) magnitude and (f) phase of the total field on Γ. The dotted green line is relative to the bare object, while the continuous and marked lines are relative to the assigned design constraints and the achieved solutions, respectively.

4.6 Concluding remarks

In this Chapter new approaches for invisibility applications, as well as for the reduction of observability, have been proposed. As a first contribution, the invisibility within approximated models has been dealt with and some interesting guidelines have been proposed and detailed to design invisible objects. Second, the synthesis strategy proposed and discussed in the previous Chapter has been herein applied to design GRIN dielectric cloaks. Interestingly, the GAMs based synthesis procedure has been successfully exploited, thus showing the effectiveness of the developed tool and its capability in realizing artificial dielectrics (which are indeed mandatory for a large class of objects to be hidden). Finally, by taking advantage from the general framework of the inverse scattering problem, the synthesis of 'nearly invisible' object has been pursued by just admitting a perturbation (i.e., a reduction in amplitude or/and a delay) of the primary source perceived by the observer, and in order to achieve simpler or more convenient solutions.

5

SUMMARY AND POSSIBLE DEVELOPMENTS

Differently from the large majority of contributions on the subject, in this thesis inverse scattering procedures and methodologies have been exploited as an electromagnetic *design* tool. In fact, the most common goal of an inverse scattering problem is the non-invasive diagnostics of an unknown target by means of an effective processing of the measured scattered field. To this aim, a huge number of contributions can be found in literature which propose innovative and practical inversion strategies devoted to simplify the solution of the problem and make it as accurate as possible.

Conversely, a different point of view of the inverse scattering problem has been considered in the thesis. In fact, by simply substituting the measured scattered field with some desired specifications for the field, the original diagnostics problem is turned into a synthesis problem. In this way, it is possible to design innovative dielectric devices by keeping unchanged the mathematical formulation of the inverse scattering problem.

Interestingly, regularization techniques usually exploited in imaging problems become here ways to enforce given properties, multi-view imaging problems turn into multi-purpose design problems, multi-frequency inverse scattering may serve to realize multi-band devices, thus opening the way to a large number of relatively simple possibilities.

More in detail, the contributions of the thesis can be summarized as it follows.

After a brief recall of the inverse scattering problem formulation and properties in the first Chapter, in the second Chapter the main approximated solution strategies of the inverse scattering problem have been first discussed using a spectral based analysis. In particular, by paralleling results holding for the Born approximation (BA), a Fourier relationship between the scattered field and the unknown of the problem has been derived for the *extended Born approximation* and the *strong permittivity fluctuation* approximation.

Then, by referring to the recently introduced 'virtual experiment' (VE) framework and

linear approximation (VELI), two inversion strategies have been also proposed which aim at extending the VELI approximation to more complex scenarios: the *distorted virtual experiment* (DVE) method deals with the retrieving of anomalies occurring in known (or partially known) inhomogeneous scenarios, while the *distorted iterated virtual experiment* (DIVE) approach aims at enlarging the range of applicability of the VE-based approximation (i.e., non-weak targets are dealt) by exploiting the DVE procedures in an iterative scheme. Notably, the assessment of the strategies has been carried out in case of both numerical and experimental data, and the satisfactory results have shown the actual capability of the approaches to image non-weak scatterers and to overcome the canonical strategies arising from the BA.
Finally, by taking inspiration from the main results by Devaney and Wolf [24], a novel representation for (a class of) non-radiating currents has been derived, which allows a general representation by means of a constrained orthonormal expansion basis. Such a result is indeed of interest in the design of antennas, in inverse scattering based diagnostics techniques (where radiating currents are easily found, so that non radiating harder ones are of interest) and, of course, in the design of invisibility devices.

The third Chapter has been devoted to the adoption of inverse scattering facilities as a design tool. To this aim, a modified version of the Contrast Source Inversion (CSI) method has been developed by considering one more set of unknowns which are the amplitudes of the primary sources (usually assumed unitary). Interestingly, the fields' amplitudes arising from the minimization of the new functional involved in the CSI allow a proper rescaling of the field itself in order to guarantee a better and easier fitting of the design equation. Further manipulations of the CSI functional have been performed to enforce desired behaviors of the unknown dielectric profile. In this respect, the CSI scheme has been constrained by adding penalty terms able to design dielectric devices exhibiting physically feasible, circularly symmetric and gently varying profiles. Moreover, the Compressive Sensing tool has been also exploited as design facilitator to enforce *sparsity* on the radial variation of the permittivity function. Notably, such a condition deals with piece-wise constant profiles which are more suitable for manufacturing.
The formulation of the CSI method as a design tool, as well as the adoption of design facilitators allowing to synthesize more easily realizable devices, are important results by themselves, as up to now the exploitation of GRIN antennas has been limited to the case of canonical solutions (like Luneburg or Maxwell fish-eye lenses). Besides allowing the introduction of non canonical GRIN devices, the power of the synthesis strategy has been considerably enlarged by defining a novel representation basis for

the unknown contrast function which allows to directly synthesize dielectric inclusions of small size and fixed arrangement embedded in a vacuum background. Such a kind of profile is the basic structure of an Artificial Materials (AMs) device, in which the gradient of the refractive index, or of the filling factor, or even of the lattice, guides the in-plane electromagnetic field path. In this respect, two strategies have been proposed, the first one dealing with the design of the permittivity values for the inclusions and the second one concerning the determination of their dimensions. Note that the first result is of interest by itself, since a discrete profile is directly looked for, while avoiding post-discretization procedures (e.g., by means of homogenization theories) that lead to an unavoidable performances degradation. Moreover, the latter allows to further reduce the complexity of the synthesized device, since a single material would be involved in manufacturing. Interestingly, the proposed procedures have shown the capability of design dielectric profile antennas emulating canonical lenses (and beyond) as well as antennas generating generic given patterns.

Finally, the fourth Chapter has been devoted to the synthesis of cloaking devices. As is known, invisibility requirements have been always an interesting topic in many application fields. For this reason, several approaches, such as *scattering cancellation* and *transformation optics*, have been proposed. However, the physical properties underlying the problem lead to deal with cloaks made up by artificial materials. In this respect, the inverse scattering framework constitutes a powerful tool, since by simply modifying the data of the problem (i.e., by imposing a null scattered field on an observation domain) it allows to synthesize the dielectric properties of an invisibility cloak. In the chapter, the design of GRIN profiles has been firstly carried out in order to prove the effectiveness of the approach. In this spirit, several examples have been considered by pursuing both a 'full aspect invisibility' as well as 'quasi-invisibility' conditions, these latter allowing a sort of relaxation of invisibility requirements (i.e., an attenuation and/or a delay of the incident field are allowed). Then, the tool developed in the previous chapter for design AMs-based antennas has been applied also in this case, so that graded Artificial Materials cloaks have been synthesized and very good performances have been reached.

In addition to that, the spectral analysis discussed in the second Chapter has been reformulated in order to give useful guidelines for design invisibility devices. As a matter of fact, the existing Fourier relationship between the scattered field and the auxiliary unknown function can be handled to enforce null scattered fields. In particular, such a condition can be reached by synthesizing a contrast function (for the cloaking region) such that the contrast function of the overall system has a null Fourier transform

inside the Ewald sphere. Notably, such a result seems to include results implicitly or explicitly given in [161] and [116], respectively. Hints for a simple design procedure have been given and work is in progress on the subject.

Possible developments

Starting from the solution of an inverse scattering problem, new innovative tools have been proposed for the design of two-dimensional variable dielectric profiles and graded AMs devices. Interestingly, the proposed synthesis approaches and tools are not restricted to the realization of 'canonical' fields, so that they can be applied to generic field specifications, thus looking forward the design of innovative devices.

Because of the achieved results, additional possible developments are worth being mentioned.

Firstly, an extension of the procedures for AM based design to the out-of-plane propagation could allow to handle AMs-based fibers. In particular, by properly synthesizing the electromagnetic properties of inclusions surrounding the defect could lead to a better confinement of the propagating field. Also, the exploitation of the above concepts and tools for the synthesis of antennas based on metasurfaces [127] is indeed expected.

Strongly related with the above cases, a second possibility concerns the adoption of the generalized Scattering Matrix Method tool developed in [178–180], in which a convenient aggregation into macrocells has been exploited for the analysis of two-dimensional Electromagnetic Band Gap structures. In this respect, from a synthesis point of view, one could in principle determine the response of a macrocell in a first step and its internal structure at a second stage, thus obtaining remarkable benefits in terms of computational time and complexity of the scattering problem at hand. In fact, some modularity and multiscale characteristic can also be inserted in the design problem one is dealing with.

As far as the invisibility problem is concerned, several possibilities also come into play. First, as already sketched, spectral solutions can be developed. As a second possibility, one could exploit inverse scattering methodologies to achieve universal cloaks; in fact, a null field could be enforced on a limited domain so that whatever the object inside such a region would become invisible. Third, the invisibility problem could be dealt with by looking for contrast sources of the kind described by the original representation in Section 2.5.

All the introduced approaches have been discussed with reference to the canonical scalar electromagnetic TM case. The (needed) extension to the 3D case, which is

conceptually simple, requires anyway non trivial effort, and represents one of the activities currently running at the LEMMA group in Reggio Calabria.

A

Appendix A

Mathematical basics of Compressive Sensing

In order to recall the basics of Compressive Sensing (CS) theory, let us consider a generic linear problem:

$$\mathbf{y} = \mathbf{A}\mathbf{x} \tag{A.1}$$

where $\mathbf{y}$ is the $M \times 1$ data vector, $\mathbf{x}$ is the $N \times 1$ vector that represents the unknown function, while $\mathbf{A}$ is the $M \times N$ matrix which relates the unknown vector to the data vector. By assuming the usual CS terminology, $\mathbf{A}$ represents the sensing matrix.

Let us now suppose to adopt a convenient representation $M \times N$ matrix $\boldsymbol{\Psi}$ for the unknown:

$$\mathbf{x} = \boldsymbol{\Psi}\mathbf{s} \tag{A.2}$$

so that the columns of $\boldsymbol{\Psi}$ contain the basis function, while the representation coefficients $\mathbf{s}$ are sparse (i.e. only few coefficients are different from zero). Accordingly, the new formulation of the linear problem reads [43]:

$$\mathbf{y} = \mathbf{A}\boldsymbol{\Psi}\mathbf{s} = \boldsymbol{\Theta}\mathbf{s} \tag{A.3}$$

According to CS theory, by taking advantage from the sparsity of the unknown coefficients $\mathbf{s}$, it is possible to solve the inverse problem even if M is (much) less than N, but it is anyway sufficiently larger than the number S of coefficients different from zero (with $S < M < N$). In particular, the correct number of measurements M, necessary to obtain a faithful solution, is lower-bounded and has to satisfy the inequality $M \geq M^{'}$, where $M^{'}$ is proportional to S and to $logN$ [42, 43].

A very relevant non intuitive circumstance is that it is not just the number of measurements which plays a role, since also the kind of performed measurements plays a role as well. Intuitively, the matrix $\boldsymbol{\Theta} = \mathbf{A}\boldsymbol{\Psi}$ has to be deeply different from a subset of the identity matrix and should not cancel out any information about the

original signal. In particular, the image of the columns of $\boldsymbol{\Psi}$ should be spread out in the domain defined by the rows of $\mathbf{A}$. As a matter of fact, the larger this incoherence, the better the possibility to retrieve sparse signals by compressed measurements. Moreover, the matrix $\boldsymbol{\Theta}$ should approximately preserve the Euclidean length of S-sparse signals, so each S-sparse vector cannot be mapped in the null space of $\boldsymbol{\Theta}$, and each S-sparse vector has to show a non-negligible image in the space of data. The exact requirements can be formalized by means of the so-called Restricted Isometry Property (RIP) [43, 64], which guarantees conditions for an exact recovery.

Provided the above conditions are fulfilled, it is possible to solve the linear problem (A.3) by means of the following optimization constrained problem:

$$\min_{\boldsymbol{s}} \|\boldsymbol{s}\|_{\ell_1} \quad \textit{subject to} \quad \|\boldsymbol{\Theta}\mathbf{s} - \boldsymbol{y}\|_{\ell_2} \leq \delta \tag{A.4}$$

where $\|\cdot\|_{\ell_1}$ is the ℓ_1-norm and δ is a positive parameter which depends on the level of required accuracy as well as on the modeling and measurement errors.

The problem (A.4) is known as Basis Pursuit denoising (BPDN) or Least Absolute Shrinkage and Selection Operator (LASSO) problem [181]. In eq.(A.4) the minimization of the ℓ_1-norm promotes the search of sparse solutions, while the constraint enforces the data consistency. In other words, among all solutions which are consistent with the measured data within a given error, the sparsest one is sought. Note that, while the optimization problem should consider indeed the so called ℓ_0-norm [43], the relaxation into ℓ_1-norm adopted in eq.(A.4) reduces the problem to a convex programming one, and it has been shown that the two formulations are equivalent for a very wide range of cases [42, 64].

Moreover, by referring to fig.A.1 it is possible to understand the reason why the ℓ_1-norm is considered instead of the more usual ℓ_2-norm. As a matter of fact, the set of all $\mathbf{x}$ vectors that satisfy (A.3) is a plane. The ℓ_2 minimization is equivalent to blowing up a hypersphere and picking point where it touches the solution plane. Since ℓ_2 ball is spherical, usually it picks points away from coordinate axes (non-sparse members of solution plane), whereas ℓ_1 ball has aligned shape axes which help to introduce a preference for sparse members of solution set [43, 94].

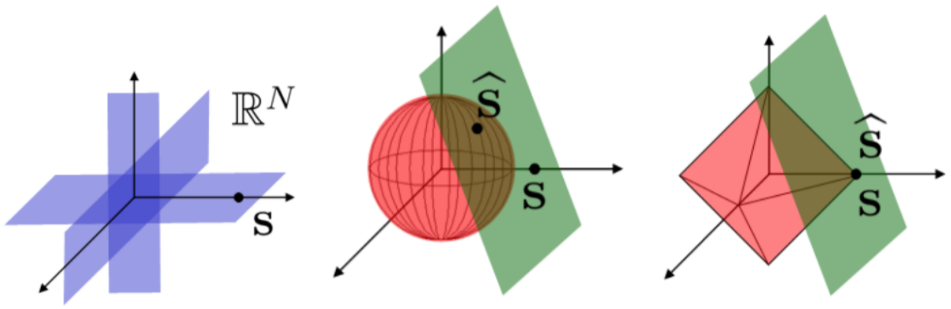

(a) (b) (c)

Fig. A.1. Graphical representation for Compressive Sensing understanding. (a) A sparse vector $\boldsymbol{s}$ lies on a K-dimensional hyperplane aligned with the coordinate axes in $\mathcal{R}^N$ and thus close to the axes. (b) Compressive sensing recovery via ℓ_2 minimization does not find the correct sparse solution $\boldsymbol{s}$ on the translated nullspace (green hyperplane) but rather the non-sparse vector $\hat{\boldsymbol{s}}$. (c) With enough measurements, recovery via ℓ_1 minimization does find the correct sparse solution $\boldsymbol{s}$.

B

Appendix B

Analytic expression for non-radiating sources

Let us recall the given expression for $f(\boldsymbol{r},\omega)$ involved in (2.45):

$$f(x,y) = \sum_{n=-\infty}^{+\infty} \sum_{m=-\infty}^{+\infty} a_{nm}\ e^{j\left(\frac{n\pi}{a}x + \frac{m\pi}{b}y\right)} \tag{B.1}$$

In order to evaluate the *non-radiating* sources W_{NR}, the Helmholtz operator must be applied on $f(\boldsymbol{r},\omega)$. Since the bi-dimensional Laplace operator is $\nabla^2 = \frac{\partial^2}{\partial x^2} + \frac{\partial^2}{\partial y^2}$, where x and y are the standard Cartesian coordinates of the xy-plane, we evaluate:

$$f'_x(x,y) = \frac{\partial f(x,y)}{\partial x} = \sum_{n=-\infty}^{+\infty} \sum_{m=-\infty}^{+\infty} j\frac{n\pi}{a}\ a_{nm}\ e^{j\left(\frac{n\pi}{a}x + \frac{m\pi}{b}y\right)} \tag{B.2}$$

$$f''_x(x,y) = \frac{\partial f'_x(x,y)}{\partial x} = \sum_{n=-\infty}^{+\infty} \sum_{m=-\infty}^{+\infty} -\left(\frac{n\pi}{a}\right)^2 a_{nm}\ e^{j\left(\frac{n\pi}{a}x + \frac{m\pi}{b}y\right)} \tag{B.3}$$

$$f'_y(x,y) = \frac{\partial f(x,y)}{\partial y} = \sum_{n=-\infty}^{+\infty} \sum_{m=-\infty}^{+\infty} j\frac{m\pi}{b}\ a_{nm}\ e^{j\left(\frac{n\pi}{a}x + \frac{m\pi}{b}y\right)} \tag{B.4}$$

$$f''_y(x,y) = \frac{\partial f'_y(x,y)}{\partial y} = \sum_{n=-\infty}^{+\infty} \sum_{m=-\infty}^{+\infty} -\left(\frac{m\pi}{b}\right)^2 a_{nm}\ e^{j\left(\frac{n\pi}{a}x + \frac{m\pi}{b}y\right)} \tag{B.5}$$

then, the final expression for W_{NR} reads:

$$W_{NR}(x,y) = \sum_{n=-\infty}^{+\infty} \sum_{m=-\infty}^{+\infty} \left[k_b^2 - \pi^2\left(\frac{n^2}{a^2} + \frac{m^2}{b^2}\right)\right] a_{nm}\ e^{j\left(\frac{n\pi}{a}x + \frac{m\pi}{b}y\right)} \tag{B.6}$$

Once the expressions for derivatives is given, constraints in (2.48) can be evaluated. In particular, let us refer to the first condition in (2.48):

$$f(x=a,y) = f(x=-a,y) = 0 \quad \Longrightarrow \quad \sum_{n=-\infty}^{+\infty} \sum_{m=-\infty}^{+\infty} a_{nm}\ e^{\pm jn\pi}\ e^{j\frac{m\pi}{b}y} = 0 \tag{B.7}$$

in which $e^{\pm jn\pi} = (-1)^n$; by inverting the order of the summations and defining $\alpha_m = \sum_{n=-\infty}^{+\infty} a_{nm}(-1)^n$, one achieves:

$$\sum_{m=-\infty}^{+\infty} \alpha_m \; e^{j\frac{m\pi}{b}y} = 0 \tag{B.8}$$

which holds if and only if $\alpha_m = 0$ for each index m. Therefore, the first constraint arises:

$$\sum_{n=-\infty}^{+\infty} a_{nm}(-1)^n = 0 \quad \forall m \tag{B.9}$$

Notably, by inverting the relation (2.50) and substituting the expression for a_{nm}, eq. (B.9) turns into the first condition in (2.51).

The same procedure can be applied for the other conditions in (2.48).

Appendix C

The contrast source inversion scheme

The contrast source inversion (CSI) method [20, 34, 35] is one of the most popular and effective inversion scheme which allows to face the inverse scattering problem in its full non-linearity by contemporary looking for both the unknown contrast χ and the auxiliary unknown W. The solution of the problem is iteratively built by minimizing the following cost functional, which takes into account the data-to-unknown relationship and the physical model [34, 35]:

$$\Phi(\chi, W^{(1)}, W^{(2)}, \dots, W^{(V)}) = \Phi_\Gamma(W^{(1)}, W^{(2)}, \dots, W^{(T)}) + \Phi_\Omega(\chi, W^{(1)}, W^{(2)}, \dots, W^{(T)}) \quad \text{(C.1)}$$

in which:

$$\Phi_\Gamma = \sum_{v=1}^{T} w_\Gamma^{(v)} \left\| \mathcal{A}_e \left[W^{(v)} \right] - E_s^{(v)} \right\|_\Gamma^2 \quad \text{(C.2)}$$

$$\Phi_\Omega = \sum_{v=1}^{T} w_\Omega^{(v)} \left\| \chi \mathcal{A}_i \left[W^{(v)} \right] + \chi E_i^{(v)} - W^{(v)} \right\|_\Omega^2 \quad \text{(C.3)}$$

where $\|\cdot\|$ is the ℓ_2-norm, T is the number of impinging directions and $w_\Gamma^{(v)}$ and $w_\Omega^{(v)}$ are normalization coefficients defined as follow:

$$w_\Gamma^{(v)} = \frac{1}{\left\| E_s^{(v)} \right\|_\Gamma^2} \qquad w_\Omega^{(v)} = \frac{1}{\left\| E_i^{(v)} \right\|_\Omega^2} \quad \text{(C.4)}$$

Note that, as far as the normalization coefficient $w_\Omega^{(v)}$ concerns, the definition in (C.4) is non the usual one proposed in [20]. In fact, it is usually set equal to the norm of the product of the contrast function times the incident field, but such a metric will change at each iteration of the minimization procedure in an unpredictable way.

The equation (C.1) allows to define the estimates of the contrast parameters and of the contrast source parameters inside the object (for each view), as the solution of the nonlinear least square problem:

$$(\hat{\chi}, \hat{W}^{(1)}, \hat{W}^{(2)}, \ldots, \hat{W}^{(V)}) = \underset{(\chi, W^{(1)}, W^{(2)}, \ldots, W^{(V)})}{\arg\min} \Phi(\chi, W^{(1)}, W^{(2)}, \ldots, W^{(V)}) \quad \text{(C.5)}$$

Since (C.1) is a non-quadratic functional of the unknowns, it may depends on thousand of variables and hence the problem arise of how to find the global minimum. As a matter of fact, global optimization procedures lead to a high computational burden, while gradient-based minimization schemes could be trapped into local minima [19] unless a very favorable initial guess is provided.

As a suitable compromise between convergence properties and computational burden, the solution of (C.5) is pursed by following a quasi-Newton minimization procedure, whose scheme is:

$$\begin{bmatrix} \chi_{k+1} \\ W_{k+1} \end{bmatrix} = \begin{bmatrix} \chi_k \\ W_k \end{bmatrix} + \lambda_k \mathcal{H}_k \begin{bmatrix} \nabla\chi_k \\ \nabla W_k \end{bmatrix} \quad \text{(C.6)}$$

in which, k and $(k+1)$ indicate the k-th and $(k+1)$-th iteration, respectively, $\nabla\chi$ and ∇W are the gradient of the functional Φ with respect to χ and W, while λ_k is a scalar parameter that has to be evaluated at each iteration in order to guarantee the maximum decrease of the functional along the direction given by $\mathcal{H}\nabla\Phi$ ($\mathcal{H}$ being evaluated by means of a Polak-Ribiere scheme) [34].

As far as the numerical efficiency of the single minimization step is concerned, first note that the line minimization step can be performed in a very efficient and precise manner through the solution of the optimization problem:

$$\lambda_k = \arg\min \Phi(\chi_k + \lambda_k \Delta\chi_k, W_k^{(1)} + \lambda_k \Delta W_k^{(1)}, \ldots, W_k^{(T)} + \lambda_k \Delta W_k^{(T)}) \quad \text{(C.7)}$$

where $\Delta\chi_k$ and ΔW_k represent the descent research directions considered at the k-th iteration.

Notably, in [34] it has been shown that (due to the involved operators) eq.(C.7) implies the solution of a third degree algebraic equation available in a closed form. Accordingly, the solution of the line minimization steps involved in the overall optimization problem is fast and accurate. Moreover, differently from [20] in which the unknowns are alternatively updated, χ and $W^{(v)}$ are herein contemporary updated at each step of the optimization scheme.

For more details about the general structure of the optimization procedure and computation of the gradient of the functional Φ with respect to χ and W, the reader is deferred to [34].

D

Appendix D

Modified Contrast Source Inversion scheme

Let us refer to the modified functional (3.3). As found in [34], the mathematical formulation of the functional evaluated along an arbitrary line whose direction is given by $\underline{W} = [W^{(1)} + \lambda \Delta W^{(1)}, \cdots, W^{(T)} + \lambda \Delta W^{(T)}]$, $\underline{\chi} = [\chi + \lambda \Delta \chi]$, $\underline{\tau} = [\tau^{(1)} + \lambda \Delta \tau^{(1)}, \cdots, \tau^{(T)} + \lambda \Delta \tau^{(T)}]$ can still be written as a fourth degree polynomial:

$$\Phi(\underline{W}, \underline{\chi}, \underline{\tau}) = \tilde{a}_4 \lambda^4 + \tilde{a}_3 \lambda^3 + \tilde{a}_2 \lambda^2 + \tilde{a}_1 \lambda + \tilde{a}_0 \tag{D.1}$$

in which the new coefficients are the following:

$$\tilde{a}_4 = \sum_{v=1}^{T} \left\{ \left\| \Delta\chi \left[\Delta\tau^{(v)} \widehat{E}_i^{(v)} + \mathcal{A}_i[\Delta W^{(v)}] \right] \right\|_{w_\Omega}^2 \right\} \tag{D.2}$$

$$\begin{aligned} \tilde{a}_3 = 2Re \sum_{v=1}^{T} \Big\{ < \Delta\chi \left[\Delta\tau^{(v)} \widehat{E}_i^{(v)} + \mathcal{A}_i[\Delta W^{(v)}] \right], \Delta\chi \left[\tau^{(v)} \widehat{E}_i^{(v)} + \mathcal{A}_i[W^{(v)}] \right] \\ + \chi \left[\Delta\tau^{(v)} \widehat{E}_i^{(v)} + \mathcal{A}_i[\Delta W^{(v)}] \right] - \Delta W^{(v)} >_{w_\Omega} \Big\} \end{aligned} \tag{D.3}$$

$$\begin{aligned} \tilde{a}_2 = \sum_{v=1}^{T} \Big\{ \left\| \mathcal{A}_e[\Delta W^{(v)}] + \Delta\tau^{(v)} \widehat{E}_i^{(v)} \right\|_{w_\Gamma}^2 + 2Re < \Delta\chi \left[\Delta\tau^{(v)} \widehat{E}_i^{(v)} + \mathcal{A}_i[\Delta W^{(v)}] \right], \\ \chi \left[\tau^{(v)} \widehat{E}_i^{(v)} + \mathcal{A}_i[W^{(v)}] \right] - W^{(v)} >_{w_\Omega} \\ + \left\| \Delta\chi \left[\tau^{(v)} \widehat{E}_i^{(v)} + \mathcal{A}_i[W^{(v)}] \right] + \chi \left[\Delta\tau^{(v)} \widehat{E}_i^{(v)} + \mathcal{A}_i[\Delta W^{(v)}] \right] - \Delta W^{(v)} \right\|_{w_\Omega}^2 \Big\} \end{aligned} \tag{D.4}$$

$$\begin{aligned} \tilde{a}_1 = 2Re \sum_{v=1}^{T} \Big\{ < \mathcal{A}_e[\Delta W^{(v)}] + \Delta\tau^{(v)} \widehat{E}_i^{(v)}, \mathcal{A}_e[W^{(v)}] - E^{(v)} + \tau^{(v)} \widehat{E}_i^{(v)} >_{w_\Gamma} \\ + < \Delta\chi \left[\tau^{(v)} \widehat{E}_i^{(v)} + \mathcal{A}_i[W^{(v)}] \right] + \chi \left[\Delta\tau^{(v)} \widehat{E}_i^{(v)} + \mathcal{A}_i[\Delta W^{(v)}] \right] - \Delta W^{(v)}, \\ \chi \left[\tau^{(v)} \widehat{E}_i^{(v)} + \mathcal{A}_i[W^{(v)}] \right] - W^{(v)} >_{w_\Omega} \Big\} \end{aligned} \tag{D.5}$$

$$\tilde{a}_0 = \sum_{v=1}^{T} \left\{ \left\| \mathcal{A}_e[W^{(v)}] - E^{(v)} + \tau^{(v)} \widehat{E}_i^{(v)} \right\|_{w_\Gamma}^2 + \left\| \chi \left[\tau^{(v)} \widehat{E}_i^{(v)} + \mathcal{A}_i[W^{(v)}] \right] - W^{(v)} \right\|_{w_\Omega}^2 \right\} \tag{D.6}$$

Note, the subscripts w_Γ and w_Ω stand for a normalization of the term at hand with respect to $\left\|E^{(v)}\right\|_2^2$ and $\left\|\widehat{E}_i^{(v)}\right\|_2^2$, respectively, in which $\|\cdot\|_2$ is the ℓ_2-norm.

As far as the gradient of the functional is concerned, due to an increment $\Delta W^{(v)}$, $\Delta\chi$ and $\Delta\tau^{(v)}$, respectively, by following [34] it gets:

$$\nabla W = 2 \sum_{v=1}^{T} \left(\frac{\mathcal{A}_e^\dagger \left[\mathcal{A}_e[W^{(v)}] - E^{(v)} + \tau^{(v)} \widehat{E}_i^{(v)} \right]}{\left\|E^{(v)}\right\|_2^2} - \frac{\chi \left[\tau^{(v)} \widehat{E}_i^{(v)} + \mathcal{A}_i[W^{(v)}] \right] - W^{(v)}}{\left\|\widehat{E}_i^{(v)}\right\|_2^2} + \frac{\mathcal{A}_i^\dagger \left\{ \chi^* \left[\chi \left(\tau^{(v)} \widehat{E}_i^{(v)} + \mathcal{A}_i[W^{(v)}] \right) - W^{(v)} \right] \right\}}{\left\|\widehat{E}_i^{(v)}\right\|_2^2} \right) \tag{D.7}$$

$$\nabla \chi = 2 \sum_{v=1}^{T} \left(\frac{\left[\tau^{(v)} \widehat{E}_i^{(v)} + \mathcal{A}_i[W^{(v)}] \right]^* \left\{ \chi \left[\tau^{(v)} \widehat{E}_i^{(v)} + \mathcal{A}_i[W^{(v)}] \right] - W^{(v)} \right\}}{\left\|\widehat{E}_i^{(v)}\right\|_2^2} \right) \tag{D.8}$$

$$\nabla \tau = 2 \sum_{v=1}^{T} \left(\frac{\widehat{E}_i^{(v)*} \left[\mathcal{A}_e[W^{(v)}] - E^{(v)} + \tau^{(v)} \widehat{E}_i^{(v)} \right]}{\left\|E^{(v)}\right\|_2^2} + \frac{\left[\widehat{E}_i^{(v)} \chi \right]^* \left\{ \chi \left[\tau^{(v)} \widehat{E}_i^{(v)} + \mathcal{A}_i[W^{(v)}] \right] - W^{(v)} \right\}}{\left\|\widehat{E}_i^{(v)}\right\|_2^2} \right) \tag{D.9}$$

Addition of physical feasibility penalty term

The addition of penalty terms to the cost functional entails a modification on the parameters reported above. In particular, when the term related to physical feasibility constraints (3.6) is involved, the new expressions read:

$$\tilde{a}_2 = \tilde{a}_2 + \|\Delta\chi\|_2^2 \tag{D.10}$$

$$\tilde{a}_1 = \tilde{a}_1 + 2Re\left[< \chi, \Delta\chi > - < \Delta\chi, f(\chi) > \right] \tag{D.11}$$

$$\tilde{a}_0 = \tilde{a}_0 + \|\chi\|_2^2 + \|f(\chi)\|_2^2 - 2Re < \chi, f(\chi) > \tag{D.12}$$

$$\nabla\chi = \nabla\chi + 2\left[\chi - f(\chi)\right] \tag{D.13}$$

Addition of circular symmetry penalty term

When the penalty term (3.7) is added to the cost functional, the coefficients and the gradient of the overall functional with respect to the contrast function modify as follow:

$$\tilde{a}_2 = \tilde{a}_2 + \left\| \frac{\partial \Delta\chi}{\partial\theta} \right\|_2^2 \tag{D.14}$$

$$\tilde{a}_1 = \tilde{a}_1 + 2Re < \frac{\partial\chi}{\partial\theta}, \frac{\partial\Delta\chi}{\partial\theta} > \tag{D.15}$$

$$\tilde{a}_0 = \tilde{a}_0 + \left\| \frac{\partial\chi}{\partial\theta} \right\|_2^2 \tag{D.16}$$

$$\nabla\chi = \nabla\chi - 2\frac{\partial^2\chi}{\partial\theta^2} \tag{D.17}$$

Addition of sparsity promoting penalty term

The introduction of the sparsity promoting penalty term does not allow anymore to reduce the line minimization procedure to the solution of an algebraic equation. As a consequence, the step length must be evaluated numerically, thus affecting the computational burden.

As far as the gradient of the functional concerns, it is worth to note that this latter is non-differentiable when its argument is equal to zero. This drawback can be overcome by considering the sub-gradients technique [140,141] as in [77], thus leading to:

$$\nabla\chi = -\frac{\partial}{\partial\rho}\left[\frac{\partial\chi/\partial\rho}{|\partial\chi/\partial\rho|}\right] \tag{D.18}$$

E

Appendix E

Synthesis of Σ/Δ patterns

The aim of the field synthesis procedure is the determination of the target fields E on the observation points $\boldsymbol{r}_o \in \Gamma_o$ in the near field region, such to fulfill given mask constraints and specifications on the corresponding far fields. To this end, let us consider an expansion of the Σ-field in circular harmonics for a 2D TM polarization:

$$E_\Sigma\left(\theta, r_{o_{FF}}\right) = \sum_{n=-\lceil k_b R\rceil}^{\lceil k_b R\rceil} \widehat{\gamma}_n e^{jn\theta} \tag{E.1}$$

where θ denotes the angular variable, R is the radius of the lens, $r_{o_{FF}}$ is the radius of a far field observation circle, and:

$$\widehat{\gamma}_n = \gamma_n H_n^{(2)}\left(k_b r_{o_{FF}}\right) \tag{E.2}$$

are the expansion's coefficients. In eq.(E.1), the summation has been limited to $-\lceil k_b R\rceil$, $\lceil k_b R\rceil$ in accordance with the finite number of degrees of freedom associated to a source enclosed in a circle of radius R [17].
Then, the Δ-field can be expressed as a linear combination of two Σ-fields shifted by θ_t, namely:

$$\begin{aligned} E_\Delta\left(\theta, r_{o_{FF}}\right) &= E_\Sigma\left(\theta-\theta_t, r_{o_{FF}}\right) - E_\Sigma\left(\theta+\theta_t, r_{o_{FF}}\right) \\ &= \sum_{n=-\lceil k_b R\rceil}^{\lceil k_b R\rceil} \widehat{\gamma}_n \left[e^{jn(\theta-\theta_t)} - e^{jn(\theta+\theta_t)}\right] = \sum_{n=-\lceil k_b R\rceil}^{\lceil k_b R\rceil} \widehat{\gamma}_n \left[e^{-jn\theta_t} - e^{jn\theta_t}\right] e^{jn\theta} \\ &= \sum_{n=-\lceil k_b R\rceil}^{\lceil k_b R\rceil} \widehat{\delta}_n e^{jn\theta} \end{aligned} \tag{E.3}$$

where $\widehat{\delta}_n = -2j\sin(n\theta_t)\widehat{\gamma}_n$. By so doing, only one between the $\widehat{\gamma}_n$ and $\widehat{\delta}_n$ sets of coefficients has to be evaluated in order to perform the synthesis (the other one being

related to it by a simple linear relationship).

Then, by noticing that expressions (E.1) and (E.3) resemble the expression of uniformly spaced array factors, one can follow the approaches respectively developed in the optimal "separate" synthesis of pencil [182] and difference [183] beams, as well as recent extensions to reconfigurable fields [146, 147]. By exploiting these results, the unknown coefficients can be finally determined by solving the following Convex Programming problem:

$$\min_{\widehat{\gamma}_n}\left\{-Re\left[\left.\frac{dE_{\Delta}(\theta)}{d\theta}\right|_{\theta=0}\right]\right\} \tag{E.4}$$

subject to:

$$\begin{cases} Re\left[\left.\dfrac{dE_{\Delta}(\theta)}{d\theta}\right|_{\theta=0}\right] \geq 0 & \text{(E.5a)} \\ E_{\Delta}\left(\theta=0\right)=0 & \text{(E.5b)} \\ \left|E_{\Delta}(\theta)\right|^2 \leq UB^{\Delta}(\theta) & \text{(E.5c)} \\ Re\left[E_{\Sigma}\left(\theta\right)|_{\theta=0}\right]=1 & \text{(E.5d)} \\ Im\left[E_{\Sigma}\left(\theta\right)|_{\theta=0}\right]=0 & \text{(E.5e)} \\ \left|E_{\Sigma}(\theta)\right|^2 \leq UB^{\Sigma}(\theta) & \text{(E.5f)} \end{cases}$$

where the objective function (E.4) and constraint (E.5a) allow to maximize the amplitude of the derivative of E_{Δ} in the target direction, constraints (E.5b),(E.5d) and (E.5e) define the amplitude of the two fields in the target direction, and constraints (E.5c) and (E.5f) allow to keep under control the sidelobes level of the two power patterns (UB^{Δ} and UB^{Σ} being suitable user-defined upper-bound masks).

As far as θ_t is concerned, it is easy to show that an optimal choice is the first null of the sum pattern. In fact, this allows a physical superposition between the difference pattern' maxima and the pencil beam's null.

After solving problem (E.4)-(E.5), the final expression of the two patterns on $\boldsymbol{r}_o \in \Gamma_o$ can be identified by a field backpropagation, i.e.,

$$E_{\Sigma}\left(\theta, r_o\right)=\sum_{n=-\lceil k_b R\rceil}^{\lceil k_b R\rceil}\gamma_n H_n^{(2)}\left(k_b, r_o\right)e^{jn\theta} \tag{E.6}$$

$$E_{\Delta}\left(\theta, r_o\right)=E_{\Sigma}\left(\theta-\theta_t, r_o\right)-E_{\Sigma}\left(\theta+\theta_t, r_o\right) \tag{E.7}$$

wherein, by virtue of (E.2), it is $\gamma_n=\widehat{\gamma}_n/H_n^{(2)}\left(k_b, r_{o_{FF}}\right)$.

References

1. D. Colton and R. Kress, *Inverse acoustic and electromagnetic scattering theory.* Springer Science & Business Media, 2012, vol. 93.
2. K. Hopcraft and P. R. Smith, *An introduction to electromagnetic inverse scattering.* Springer Science & Business Media, 2013, vol. 7.
3. M. Pastorino, *Microwave Imaging.* John Wiley & Sons, 2010, vol. 208.
4. M. Bertero and P. Boccacci, *Introduction to inverse problems in imaging.* CRC press, 1998.
5. M. Bertero, "Linear inverse and ill-posed problems," in *Advances in electronics and electron physics.* Elsevier, 1989, vol. 75, pp. 1–120.
6. D. J. Daniels, *Ground Penetrating Radar.* Wiley Online Library, 2005.
7. R. Persico, *Introduction to ground penetrating radar: inverse scattering and data processing.* John Wiley & Sons, 2014.
8. F. Soldovieri and L. Crocco, "Electromagnetic tomography," in *Subsurface Sensing.* NY: John Wiley & Sons, 2011, ch. 5.2, pp. 228–254.
9. L. Crocco and F. Soldovieri, "Electromagnetic tomography," in *Subsurface Sensing.* NY: John Wiley & Sons, 2011, ch. 5.5, pp. 365–376.
10. A. Massa, M. Donelli, M. Pastorino, and A. Rosani, "Microwave imaging for non-destructive evaluation of civil structures," *Insight-Non-Destructive Testing and Condition Monitoring*, vol. 47, no. 1, pp. 11–14, 2005.
11. G. Bozza, M. Brignone, M. Pastorino, M. Piana, and A. Randazzo, "Crack detection in dielectric structures by a linear sampling approach," *International Journal of Signal and Imaging Systems Engineering*, vol. 3, no. 2, pp. 73–80, 2010.
12. R. Zoughi, *Microwave non-destructive testing and evaluation principles.* Springer Science & Business Media, 2012, vol. 4.
13. F. Ahmad and M. G. Amin, "Through-the-wall human motion indication using sparsity-driven change detection," *IEEE Transactions on Geoscience and Remote Sensing*, vol. 51, no. 2, pp. 881–890, 2013.
14. A. M. Hassan and M. El-Shenawee, "Review of electromagnetic techniques for breast cancer detection," *IEEE Reviews in Biomedical Engineering*, vol. 4, pp. 103–118, 2011.

15. S. Y. Semenov and D. R. Corfield, "Microwave tomography for brain imaging: Feasibility assessment for stroke detection," *International Journal of Antennas and Propagation*, vol. 2008, 2008.
16. O. Bucci and G. Franceschetti, "On the spatial bandwidth of scattered fields," *IEEE Transactions on Antennas and Propagation*, vol. 35, no. 12, pp. 1445–1455, 1987.
17. O. M. Bucci and G. Franceschetti, "On the degrees of freedom of scattered fields," *IEEE Transactions on Antennas and Propagation*, vol. 37, no. 7, pp. 918–926, 1989.
18. O. Bucci and T. Isernia, "Electromagnetic inverse scattering: Retrievable information and measurement strategies," *Radio Science*, vol. 32, no. 6, pp. 2123–2137, 1997.
19. T. Isernia, V. Pascazio, and R. Pierri, "On the local minima in a tomographic imaging technique," *IEEE Transactions on Geoscience and Remote Sensing*, vol. 39, no. 7, pp. 1596–1607, 2001.
20. P. M. Van Den Berg and R. E. Kleinman, "A contrast source inversion method," *Inverse Problems*, vol. 13, no. 6, p. 1607, 1997.
21. M. D'Urso, T. Isernia, and A. F. Morabito, "On the solution of 2-D inverse scattering problems via source-type integral equations," *IEEE Transactions on Geoscience and Remote Sensing*, vol. 48, no. 3, pp. 1186–1198, 2010.
22. D. Colton and L. Päivärinta, "The uniqueness of a solution to an inverse scattering problem for electromagnetic waves," *Archive for Rational Mechanics and Analysis*, vol. 119, no. 1, pp. 59–70, 1992.
23. A. I. Nachman, "Global uniqueness for a two-dimensional inverse boundary value problem," *Annals of Mathematics*, pp. 71–96, 1996.
24. A. Devaney and E. Wolf, "Radiating and nonradiating classical current distributions and the fields they generate," *Physical Review D*, vol. 8, no. 4, p. 1044, 1973.
25. A. Baran, J. LoVetri, D. Kurrant, and E. Fear, "Immersion medium independent microwave breast imaging," in *2017 XXXIInd General Assembly and Scientific Symposium of the International Union of Radio Science (URSI GASS)*, 2017.
26. M. Asefi and J. LoVetri, "Use of field-perturbing elements to increase nonredundant data for microwave imaging systems," *IEEE Transactions on Microwave Theory and Techniques*, 2017.
27. A. N. Tikhonov, A. Goncharsky, V. Stepanov, and A. G. Yagola, *Numerical methods for the solution of ill-posed problems*. Springer Science & Business Media, 2013, vol. 328.
28. G. Oliveri, N. Anselmi, and A. Massa, "Compressive sensing imaging of non-sparse 2D scatterers by a total-variation approach within the born approximation," *IEEE Transactions on Antennas and Propagation*, vol. 62, no. 10, pp. 5157–5170, 2014.
29. P. Van den Berg and R. E. Kleinman, "A total variation enhanced modified gradient algorithm for profile reconstruction," *Inverse Problems*, vol. 11, no. 3, p. L5, 1995.
30. P. M. van den Berg, A. Abubakar, and J. T. Fokkema, "Multiplicative regularization for contrast profile inversion," *Radio Science*, vol. 38, no. 2, 2003.
31. L. Crocco and T. Isernia, "Inverse scattering with real data: detecting and imaging homogeneous dielectric objects," *Inverse Problems*, vol. 17, no. 6, p. 1573, 2001.

32. I. Catapano, L. Crocco, and T. Isernia, "A simple two-dimensional inversion technique for imaging homogeneous targets in stratified media," *Radio Science*, vol. 39, no. 1, 2004.

33. O. M. Bucci, L. Crocco, T. Isernia, and V. Pascazio, "Subsurface inverse scattering problems: quantifying, qualifying, and achieving the available information," *IEEE Transactions on Geoscience and Remote Sensing*, vol. 39, no. 11, pp. 2527–2538, 2001.

34. T. Isernia, V. Pascazio, and R. Pierri, "A nonlinear estimation method in tomographic imaging," *IEEE Transactions on Geoscience and Remote Sensing*, vol. 35, no. 4, pp. 910–923, 1997.

35. T. Isernia, L. Crocco, and M. D'Urso, "New tools and series for forward and inverse scattering problems in lossy media," *IEEE Geoscience and Remote Sensing Letters*, vol. 1, no. 4, pp. 327–331, 2004.

36. I. Catapano, L. Di Donato, L. Crocco, O. M. Bucci, A. F. Morabito, T. Isernia, and R. Massa, "On quantitative microwave tomography of female breast," *Progress In Electromagnetics Research*, vol. 97, pp. 75–93, 2009.

37. R. Scapaticci, I. Catapano, and L. Crocco, "Wavelet-based adaptive multiresolution inversion for quantitative microwave imaging of breast tissues," *IEEE Transactions on Antennas and Propagation*, vol. 60, no. 8, pp. 3717–3726, 2012.

38. R. Scapaticci, P. Kosmas, and L. Crocco, "Wavelet-based regularization for robust microwave imaging in medical applications," *IEEE Transactions on Biomedical Engineering*, vol. 62, no. 4, pp. 1195–1202, 2015.

39. M. Li, O. Semerci, and A. Abubakar, "A contrast source inversion method in the wavelet domain," *Inverse Problems*, vol. 29, no. 2, p. 025015, 2013.

40. R. Lencrerot, A. Litman, H. Tortel, and J.-M. Geffrin, "Imposing zernike representation for imaging two-dimensional targets," *Inverse Problems*, vol. 25, no. 3, p. 035012, 2009.

41. L. Di Donato, M. T. Bevacqua, L. Crocco, and T. Isernia, "Inverse scattering via virtual experiments and contrast source regularization," *IEEE Transactions on Antennas and Propagation*, vol. 63, no. 4, pp. 1669–1677, 2015.

42. D. L. Donoho, "Compressed sensing," *IEEE Transactions on Information Theory*, vol. 52, no. 4, pp. 1289–1306, 2006.

43. R. G. Baraniuk, "Compressive sensing [lecture notes]," *IEEE Signal Processing Magazine*, vol. 24, no. 4, pp. 118–121, 2007.

44. A. Devaney, "Geophysical diffraction tomography," *IEEE Transactions on Geoscience and Remote Sensing*, no. 1, pp. 3–13, 1984.

45. A. Devaney and M. Oristaglio, "Inversion procedure for inverse scattering within the distorted-wave born approximation," *Physical Review Letters*, vol. 51, no. 4, p. 237, 1983.

46. A. Devaney, "Inverse-scattering theory within the rytov approximation," *Optics Letters*, vol. 6, no. 8, pp. 374–376, 1981.

47. L. Tsang and J. Kong, "Scattering of electromagnetic waves from random media with strong permittivity fluctuations," *Radio Science*, vol. 16, no. 03, pp. 303–320, 1981.

48. J. Ma, W. C. Chew, C.-C. Lu, and J. Song, "Image reconstruction from te scattering data using equation of strong permittivity fluctuation," *IEEE Transactions on Antennas and Propagation*, vol. 48, no. 6, pp. 860–867, 2000.

49. A. Brancaccio, V. Pascazio, and R. Pierri, "A quadratic model for inverse profiling: the one-dimensional case," *Journal of Electromagnetic Waves and Applications*, vol. 9, no. 5-6, pp. 673–696, 1995.

50. R. Pierri, F. Soldovieri, A. Liseno, and F. De Blasio, "Dielectric profiles reconstruction via the quadratic approach in 2-d geometry from multifrequency and multifrequency/-multiview data," *IEEE Transactions on Geoscience and Remote Sensing*, vol. 40, no. 12, pp. 2709–2718, 2002.

51. Y. Wang and W. C. Chew, "An iterative solution of the two-dimensional electromagnetic inverse scattering problem," *International Journal of Imaging Systems and Technology*, vol. 1, no. 1, pp. 100–108, 1989.

52. W. C. Chew and Y.-M. Wang, "Reconstruction of two-dimensional permittivity distribution using the distorted born iterative method," *IEEE transactions on Medical Imaging*, vol. 9, no. 2, pp. 218–225, 1990.

53. T. M. Habashy, R. W. Groom, and B. R. Spies, "Beyond the Born and Rytov approximations: A nonlinear approach to electromagnetic scattering," *Journal of Geophysical Research: Solid Earth*, vol. 98, no. B2, pp. 1759–1775, 1993.

54. A. Abubakar, P. M. van den Berg, and T. M. Habashy, "Application of the multiplicative regularized contrast source inversion method on tm-and te-polarized experimental fresnel data," *Inverse Problems*, vol. 21, no. 6, p. S5, 2005.

55. C. Torres-Verdin and T. M. Habashy, "A two-step linear inversion of two-dimensional electrical conductivity," *IEEE Transactions on Antennas and Propagation*, vol. 43, no. 4, pp. 405–415, 1995.

56. A. Abubakar, T. M. Habashy, P. M. van den Berg, and D. Gisolf, "The diagonalized contrast source approach: an inversion method beyond the born approximation," *Inverse Problems*, vol. 21, no. 2, p. 685, 2005.

57. L. Crocco, M. D'Urso, and T. Isernia, "Testing the contrast source extended born inversion method against real data: the TM case," *Inverse Problems*, vol. 21, no. 6, p. S33, 2005.

58. R. E. Kleinman and P. Van den Berg, "An extended range-modified gradient technique for profile inversion," *Radio Science*, vol. 28, no. 05, pp. 877–884, 1993.

59. L. Souriau, B. Duchêne, D. Lesselier, and R. E. Kleinman, "Modified gradient approach to inverse scattering for binary objects in stratified media," *Inverse Problems*, vol. 12, no. 4, p. 463, 1996.

60. X. Chen, "Subspace-based optimization method for solving inverse-scattering problems," *IEEE Transactions on Geoscience and Remote Sensing*, vol. 48, no. 1, pp. 42–49, 2010.

61. B. Kashin, "The widths of certain finite dimensional sets and classes of smooth functions, Izvestia 41 (1977), 334–351," *MR0481792 (58: 1891)*, 1891.

62. E. D. Gluskin, "Norms of random matrices and widths of finite-dimensional sets," *Mathematics of the USSR-Sbornik*, vol. 48, no. 1, p. 173, 1984.

63. L. I. Rudin, S. Osher, and E. Fatemi, "Nonlinear total variation based noise removal algorithms," *Physica D: Nonlinear Phenomena*, vol. 60, no. 1-4, pp. 259–268, 1992.

64. E. J. Candès, J. Romberg, and T. Tao, "Robust uncertainty principles: Exact signal reconstruction from highly incomplete frequency information," *IEEE Transactions on Information Theory*, vol. 52, no. 2, pp. 489–509, 2006.

65. E. J. Candès and M. B. Wakin, "An introduction to compressive sampling," *IEEE Signal Processing Magazine*, vol. 25, no. 2, pp. 21–30, 2008.

66. S. Qaisar, R. M. Bilal, W. Iqbal, M. Naureen, and S. Lee, "Compressive sensing: From theory to applications, a survey," *Journal of Communications and networks*, vol. 15, no. 5, pp. 443–456, 2013.

67. A. C. Gurbuz, J. H. McClellan, and W. R. Scott Jr, "Compressive sensing for subsurface imaging using ground penetrating radar," *Signal Processing*, vol. 89, no. 10, pp. 1959–1972, 2009.

68. W. Zhang, M. G. Amin, F. Ahmad, A. Hoorfar, and G. E. Smith, "Ultrawideband impulse radar through-the-wall imaging with compressive sensing," *International Journal of Antennas and Propagation*, vol. 2012, 2012.

69. M. Ambrosanio and V. Pascazio, "A compressive-sensing-based approach for the detection and characterization of buried objects," *IEEE Journal of Selected Topics in Applied Earth Observations and Remote Sensing*, vol. 8, no. 7, pp. 3386–3395, 2015.

70. M. Lustig, D. L. Donoho, J. M. Santos, and J. M. Pauly, "Compressed sensing MRI," *IEEE Signal Processing Magazine*, vol. 25, no. 2, pp. 72–82, 2008.

71. X. Zhu, Z. Zhao, J. Wang, J. Song, and Q. H. Liu, "Microwave-induced thermal acoustic tomography for breast tumor based on compressive sensing," *IEEE Transactions on Biomedical Engineering*, vol. 60, no. 5, pp. 1298–1307, 2013.

72. M. Azghani, P. Kosmas, and F. Marvasti, "Microwave medical imaging based on sparsity and an iterative method with adaptive thresholding," *IEEE Transactions on Medical Imaging*, vol. 34, no. 2, pp. 357–365, 2015.

73. M. T. Bevacqua, L. Crocco, L. Di Donato, T. Isernia, and R. Palmeri, "Exploiting sparsity and field conditioning in subsurface microwave imaging of nonweak buried targets," *Radio Science*, vol. 51, no. 4, pp. 301–310, 2016.

74. R. Palmeri, M. T. Bevacqua, L. Di Donato, L. Crocco, and T. Isernia, "Microwave imaging of non-weak targets in stratified media via virtual experiments and compressive sensing," in *Antennas and Propagation (EUCAP), 2017 11th European Conference on*. IEEE, 2017, pp. 1711–1715.

75. L. Poli, G. Oliveri, and A. Massa, "Microwave imaging within the first-order born approximation by means of the contrast-field bayesian compressive sensing," *IEEE Transactions on Antennas and Propagation*, vol. 60, no. 6, pp. 2865–2879, 2012.

76. A. Desmal and H. Bağcı, "Shrinkage-thresholding enhanced born iterative method for solving 2D inverse electromagnetic scattering problem," *IEEE Transactions on Antennas and Propagation*, vol. 62, no. 7, pp. 3878–3884, 2014.

77. M. T. Bevacqua, L. Crocco, L. Di Donato, and T. Isernia, "Non-linear inverse scattering via sparsity regularized contrast source inversion," *IEEE Transactions on Computational Imaging*, vol. 3, no. 2, pp. 296–304, 2017.

78. M. D. Migliore, "A compressed sensing approach for array diagnosis from a small set of near-field measurements," *IEEE Transactions on Antennas and Propagation*, vol. 59, no. 6, pp. 2127–2133, 2011.

79. ——, "Array diagnosis from far-field data using the theory of random partial fourier matrices," *IEEE Antennas and Wireless Propagation Letters*, vol. 12, pp. 745–748, 2013.

80. B. Fuchs, L. Le Coq, and M. D. Migliore, "Fast antenna array diagnosis from a small number of far-field measurements," *IEEE Transactions on Antennas and Propagation*, vol. 64, no. 6, pp. 2227–2235, 2016.

81. A. F. Morabito, R. Palmeri, and T. Isernia, "A compressive-sensing-inspired procedure for array antenna diagnostics by a small number of phaseless measurements," *IEEE Transactions on Antennas and Propagation*, vol. 64, no. 7, pp. 3260–3265, 2016.

82. A. J. Devaney, *Mathematical foundations of imaging, tomography and wavefield inversion*. Cambridge University Press, 2012.

83. W. Chew, *Waves and Fields in Inhomogeneous Media*, ser. IEEE Press series on electromagnetic waves. Van Nostrand Reinhold, 1990.

84. L. Crocco, I. Catapano, L. Di Donato, and T. Isernia, "The linear sampling method as a way to quantitative inverse scattering," *IEEE Transactions on Antennas and Propagation*, vol. 60, no. 4, pp. 1844–1853, 2012.

85. L. Di Donato and L. Crocco, "Model-based quantitative cross-borehole gpr imaging via virtual experiments," *IEEE Transactions on Geoscience and Remote Sensing*, vol. 53, no. 8, pp. 4178–4185, 2015.

86. L. Di Donato, R. Palmeri, G. Sorbello, T. Isernia, and L. Crocco, "Assessing the capabilities of a new linear inversion method for quantitative microwave imaging," *International Journal of Antennas and Propagation*, vol. 2015, 2015.

87. ——, "A new linear distorted-wave inversion method for microwave imaging via virtual experiments," *IEEE Transactions on Microwave Theory and Techniques*, vol. 64, no. 8, pp. 2478–2488, 2016.

88. M. T. Bevacqua, L. Crocco, L. Di Donato, and T. Isernia, "An algebraic solution method for nonlinear inverse scattering," *IEEE Transactions on Antennas and Propagation*, vol. 63, no. 2, pp. 601–610, 2015.

89. ——, "Microwave imaging of nonweak targets via compressive sensing and virtual experiments," *IEEE Antennas and Wireless Propagation Letters*, vol. 14, pp. 1035–1038, 2015.

90. M. T. Bevacqua and L. Di Donato, "Improved TV-CS approaches for inverse scattering problem," *The Scientific World Journal*, vol. 2015, 2015.

91. R. Palmeri, M. T. Bevacqua, L. Crocco, T. Isernia, and L. Di Donato, "Microwave imaging via distorted iterated virtual experiments," *IEEE Transactions on Antennas and Propagation*, vol. 65, no. 2, pp. 829–838, 2017.

92. R. Palmeri, M. T. Bevacqua, R. Scapaticci, A. F. Morabito, L. Crocco, and T. Isernia, "Biomedical imaging via wavelet-based regularization and distorted iterated virtual experiments," in *Electromagnetics in Advanced Applications (ICEAA), 2017 International Conference on*. IEEE, 2017, pp. 1381–1384.

93. L. Di Donato, "New Paradigms and Simple Methods for Inverse Scattering problems," PhD Thesis, Università "Mediterranea" di Reggio Calabria, 2011/2012.

94. M. T. Bevacqua, "Quantitative Inverse Scattering via Virtual Experiments and Compressive Sensing," PhD Thesis, Università "Mediterranea" di Reggio Calabria, 2014/2015.

95. L. Crocco, L. Di Donato, D. A. Iero, and T. Isernia, "An adaptive method to focusing in an unknown scenario," *Progress In Electromagnetics Research*, vol. 130, pp. 563–579, 2012.

96. D. Colton, H. Haddar, and M. Piana, "The linear sampling method in inverse electromagnetic scattering theory," *Inverse Problems*, vol. 19, no. 6, p. S105, 2003.

97. F. Cakoni and D. Colton, *Qualitative methods in inverse scattering theory: An introduction*. Springer Science & Business Media, 2005.

98. I. Catapano, L. Crocco, and T. Isernia, "On simple methods for shape reconstruction of unknown scatterers," *IEEE Transactions on Antennas and Propagation*, vol. 55, no. 5, pp. 1431–1436, 2007.

99. I. Catapano, L. Crocco, M. D'Urso, and T. Isernia, "3D microwave imaging via preliminary support reconstruction: Testing on the Fresnel 2008 database," *Inverse Problems*, vol. 25, no. 2, p. 024002, 2009.

100. I. Catapano and L. Crocco, "An imaging method for concealed targets," *IEEE Transactions on Geoscience and Remote sensing*, vol. 47, no. 5, pp. 1301–1309, 2009.

101. L. Crocco, L. Di Donato, I. Catapano, and T. Isernia, "An improved simple method for imaging the shape of complex targets," *IEEE Transactions on Antennas and Propagation*, vol. 61, no. 2, pp. 843–851, 2013.

102. P. C. Hansen, "The discrete picard condition for discrete ill-posed problems," *BIT Numerical Mathematics*, vol. 30, no. 4, pp. 658–672, 1990.

103. P. C. Hansen and D. P. O'Leary, "The use of the L-curve in the regularization of discrete ill-posed problems," *SIAM Journal on Scientific Computing*, vol. 14, no. 6, pp. 1487–1503, 1993.

104. R. Palmeri, A. F. Morabito, and T. Isernia, "Design of a varying dielectric profile antenna generating reconfigurable Σ—Δ pattern via inverse scattering theory," in *Electromagnetics in Advanced Applications (ICEAA), 2017 International Conference on*. IEEE, 2017, pp. 1303–1306.

105. M. T. Bevacqua, R. Palmeri, L. Di Donato, L. Crocco, and T. Isernia, "Microwave imaging via iterated virtual experiments," in *Antennas and Propagation (EuCAP), 2016 10th European Conference on*. IEEE, 2016, pp. 1–5.

106. K. Belkebir and M. Saillard, "Testing inversion algorithms against experimental data: inhomogeneous targets," *Inverse Problems*, vol. 21, no. 6, p. S1, 2005.

107. L. Fu, S. Liu, and L. Liu, "Internal structure characterization of living tree trunk cross-section using GPR: Numerical examples and field data analysis," in *Ground Penetrating Radar (GPR), 2014 15th International Conference on*. IEEE, 2014, pp. 155–160.

108. J. Richmond, "Scattering by a dielectric cylinder of arbitrary cross section shape," *IEEE Transactions on Antennas and Propagation*, vol. 13, no. 3, pp. 334–341, 1965.

109. L. Di Donato, M. T. Bevacqua, T. Isernia, I. Catapano, and L. Crocco, "Improved quantitative microwave tomography by exploiting the physical meaning of the linear sampling method," in *Antennas and Propagation (EUCAP), Proceedings of the 5th European Conference on*. IEEE, 2011, pp. 3828–3831.

110. K. Belkebir and M. Saillard, "Special section: Testing inversion algorithms against experimental data," *Inverse Problems*, vol. 17, no. 6, p. 1565, 2001.

111. C. Gilmore, P. Mojabi, and J. LoVetri, "Comparison of an enhanced distorted born iterative method and the multiplicative-regularized contrast source inversion method," *IEEE Transactions on Antennas and Propagation*, vol. 57, no. 8, pp. 2341–2351, 2009.

112. A. J. Devaney and E. A. Marengo, "A method for specifying non-radiating, monochromatic, scalar sources and their fields," *Pure and Applied Optics: Journal of the European Optical Society Part A*, vol. 7, no. 5, p. 1213, 1998.

113. E. Martini, S. Maci, and A. D. Yaghjian, "Cloaking in Terms of Nonradiating Cancelling Currents," in *Selected Topics in Photonic Crystals and Metamaterials*. World Scientific, 2011, ch. 11.

114. G. Gbur, "Invisibility Physics: Past, Present, and Future," in *Progress in Optics*, ser. Progress in Optics. Elsevier, 2013, vol. 58, ch. 11.

115. E. Hurwitz and G. Gbur, "Null-field radiationless sources," *Optics Letters*, vol. 39, no. 22, pp. 6529–6532, 2014.

116. G. Labate and L. Matekovits, "Invisibility and cloaking structures as weak or strong solutions of devaney-wolf theorem," *Optics Express*, vol. 24, no. 17, pp. 19 245–19 253, 2016.

117. G. Labate, A. Alù, and L. Matekovits, "Surface-admittance equivalence principle for nonradiating and cloaking problems," *Physical Review A*, vol. 95, no. 6, p. 063841, 2017.

118. A. J. Devaney, "Nonradiating surface sources," *JOSA A*, vol. 21, no. 11, pp. 2216–2222, 2004.

119. R. K. Luneburg and M. Herzberger, *Mathematical Theory of Optics*. University of California, 1964.

120. S. P. Morgan, "General solution of the Luneberg lens problem," *Journal of Applied Physics*, vol. 29, no. 9, pp. 1358–1368, 1958.

121. W. Thomson and N. M. Ferrers, *The Cambridge and Dublin Mathematical Journal*. Macmillan, 1847, vol. 2.

122. H. Mosallaei and Y. Rahmat-Samii, "Nonuniform Luneburg and two-shell lens antennas: radiation characteristics and design optimization," *IEEE Transactions on Antennas and Propagation*, vol. 49, no. 1, pp. 60–69, 2001.

123. B. Fuchs, O. Lafond, S. Rondineau, and M. Himdi, "Design and characterization of half Maxwell fish-eye lens antennas in millimeter waves," *IEEE Transactions on Microwave Theory and Techniques*, vol. 54, no. 6, pp. 2292–2300, 2006.

124. B. Fuchs, L. Le Coq, O. Lafond, S. Rondineau, and M. Himdi, "Design optimization of multishell Luneburg lenses," *IEEE Transactions on Antennas and Propagation*, vol. 55, no. 2, pp. 283–289, 2007.

125. J. B. Pendry, D. Schurig, and D. R. Smith, "Controlling electromagnetic fields," *science*, vol. 312, no. 5781, pp. 1780–1782, 2006.

126. I. Aghanejad, H. Abiri, and A. Yahaghi, "Design of high-gain lens antenna by gradient-index metamaterials using transformation optics," *IEEE Transactions on Antennas and Propagation*, vol. 60, no. 9, pp. 4074–4081, 2012.

127. M. Bosiljevac, M. Casaletti, F. Caminita, Z. Sipus, and S. Maci, "Non-uniform metasurface luneburg lens antenna design," *IEEE Transaction on Antennas and Propagation*, vol. 60, no. 9, pp. 4065–4073, 2012.

128. J. Zhang, Y. Luo, H. Chen, and B.-I. Wu, "Manipulating the directivity of antennas with metamaterial," *Optics Express*, vol. 16, no. 15, pp. 10 962–10 967, 2008.

129. Z. Duan, B.-I. Wu, J. A. Kong, F. Kong, and S. Xi, "Enhancement of radiation properties of a compact planar antenna using transformation media as substrates," *Progress In Electromagnetics Research*, vol. 83, pp. 375–384, 2008.

130. W. X. Jiang, T. J. Cui, H. F. Ma, X. M. Yang, and Q. Cheng, "Layered high-gain lens antennas via discrete optical transformation," *Applied Physics Letters*, vol. 93, no. 22, p. 221906, 2008.

131. P.-H. Tichit, S. N. Burokur, and A. de Lustrac, "Ultradirective antenna via transformation optics," *Journal of Applied Physics*, vol. 105, no. 10, p. 104912, 2009.

132. I. Gallina, G. Castaldi, and V. Galdi, "Transformation media for thin planar retrodirective reflectors," *IEEE Antennas and Wireless Propagation Letters*, vol. 7, pp. 603–605, 2008.

133. M. Moccia, G. Castaldi, V. Galdi, A. Alù, and N. Engheta, "Dispersion engineering via nonlocal transformation optics," *Optica*, vol. 3, no. 2, pp. 179–188, 2016.

134. O. M. Bucci, I. Catapano, L. Crocco, and T. Isernia, "Synthesis of new variable dielectric profile antennas via inverse scattering techniques: a feasibility study," *IEEE Transactions on Antennas and Propagation*, vol. 53, no. 4, pp. 1287–1297, 2005.

135. T. Isernia, R. Palmeri, A. F. Morabito, and L. Di Donato, "Inverse scattering and compressive sensing as advanced e.m. design tool," in *International Symposium on Antennas and Propagation*. IEEE, 2017.

136. L. Di Donato, L. Crocco, M. T. Bevacqua, and T. Isernia, "Quasi Invisibility via inverse scattering techniques," in *Antenna Measurements & Applications (CAMA), 2014 IEEE Conference on*. IEEE, 2014, pp. 1–2.

137. L. Di Donato, T. Isernia, G. Labate, and L. Matekovits, "Towards printable natural dielectric cloaks via inverse scattering techniques," *Scientific Reports*, vol. 7, no. 1, p. 3680, 2017.

138. P. M. Van den Berg, A. Van Broekhoven, and A. Abubakar, "Extended contrast source inversion," *Inverse Problems*, vol. 15, no. 5, p. 1325, 1999.

139. A. Abubakar and P. M. Van Den Berg, "Total variation as a multiplicative constraint for solving inverse problems," *IEEE Transactions on Image Processing*, vol. 10, no. 9, pp. 1384–1392, 2001.

140. S. Boyd, J. Duchi, and L. Vandenberghe, "Subgradients, lecture notes for ee364b," 2011.

141. M. Schmidt, G. Fung, and R. Rosales, "Fast optimization methods for l1 regularization: A comparative study and two new approaches," in *European Conference on Machine Learning*. Springer, 2007, pp. 286–297.

142. E. J. Candes, M. B. Wakin, and S. P. Boyd, "Enhancing sparsity by reweighted l1-minimization," *Journal of Fourier analysis and applications*, vol. 14, no. 5, pp. 877–905, 2008.

143. R. S. Elliot, *Antenna theory and design*. John Wiley & Sons, 2006.

144. T.-S. Lee and T.-K. Tseng, "Subarray-synthesized low-side-lobe sum and difference patterns with partial common weights," *IEEE Transactions on Antennas and Propagation*, vol. 41, no. 6, pp. 791–800, 1993.

145. F. Ares, J. Rodriguez, E. Moreno, and S. Rengarajan, "Optimal compromise among sum and difference patterns," *Journal of Electromagnetic Waves and Applications*, vol. 10, no. 11, pp. 1543–1555, 1996.

146. A. F. Morabito and P. Rocca, "Optimal synthesis of sum and difference patterns with arbitrary sidelobes subject to common excitations constraints," *IEEE Antennas Wireless Propagation Letters*, vol. 9, pp. 623–626, 2010.

147. P. Rocca and A. F. Morabito, "Optimal synthesis of reconfigurable planar arrays with simplified architectures for monopulse radar applications," *IEEE Transaction on Antennas and Propagation*, vol. 63, no. 3, pp. 1048–1058, 2015.

148. C. A. Balanis, *Antenna Theory*. John Wiley & Sons, 1982.

149. J. D. Joannopoulos, S. G. Johnson, J. N. Winn, and R. D. Meade, *Photonic crystals: molding the flow of light*. Princeton University, 2011.

150. B. Vasić, G. Isić, R. Gajić, and K. Hingerl, "Controlling electromagnetic fields with graded photonic crystals in metamaterial regime," *Optics Express*, vol. 18, no. 19, pp. 20 321–20 333, 2010.

151. Y. L. Loo, Y. Yang, N. Wang, Y. G. Ma, and C. K. Ong, "Broadband microwave Luneburg lens made of gradient index metamaterials," *JOSA A*, vol. 29, no. 4, pp. 426–430, 2012.

152. X.-H. Sun, Y.-L. Wu, W. Liu, Y. Hao, and L.-D. Jiang, "Luneburg lens composed of sunflower-type graded photonic crystals," *Optics Communications*, vol. 315, pp. 367–373, 2014.

153. Y.-Y. Zhao, Y.-L. Zhang, M.-L. Zheng, X.-Z. Dong, X.-M. Duan, and Z.-S. Zhao, "Anisotropic and omnidirectional focusing in Luneburg lens structure with gradient photonic crystals," *Journal of Optics*, vol. 19, no. 1, p. 015605, 2016.

154. F. Gaufillet and E. Akmansoy, "Graded photonic crystals for Luneburg lens," *IEEE Photonics Journal*, vol. 8, no. 1, pp. 1–11, 2016.

155. W. Liu, X. Sun, M. Gao, and S. Wang, "Luneburg and flat lens based on graded photonic crystal," *Optics Communications*, vol. 364, pp. 225–232, 2016.

156. D. S. Jones, *Acoustic and electromagnetic waves*. Oxford University Press, 1986.

157. M. Abramowitz and I. A. Stegun, *Handbook of mathematical functions: with formulas, graphs, and mathematical tables*. Courier Corporation, 1964, vol. 55.

158. A. H. Sihvola, *Electromagnetic mixing formulas and applications*. Iet, 1999, no. 47.

159. P.-Y. Chen, J. Soric, and A. Alù, "Invisibility and cloaking based on scattering cancellation," *Advanced Materials*, vol. 24, no. 44, 2012.

160. A. Alù and N. Engheta, "Cloaking a sensor," *Physical Review Letters*, vol. 102, no. 23, p. 233901, 2009.

161. ——, "Achieving transparency with plasmonic and metamaterial coatings," *Physical Review E*, vol. 72, no. 1, p. 016623, 2005.

162. M. G. Silveirinha, A. Alù, and N. Engheta, "Parallel-plate metamaterials for cloaking structures," *Physical Review E*, vol. 75, no. 3, p. 036603, 2007.

163. F. Bilotti, S. Tricarico, and L. Vegni, "Electromagnetic cloaking devices for te and tm polarizations," *New Journal of Physics*, vol. 10, no. 11, p. 115035, 2008.

164. B. Edwards, A. Alù, M. G. Silveirinha, and N. Engheta, "Experimental verification of plasmonic cloaking at microwave frequencies with metamaterials," *Physical Review Letters*, vol. 103, no. 15, p. 153901, 2009.

165. S. Tricarico, F. Bilotti, A. Alù, and L. Vegni, "Plasmonic cloaking for irregular objects with anisotropic scattering properties," *Physical Review E*, vol. 81, no. 2, p. 026602, 2010.

166. A. Monti, A. Alù, A. Toscano, and F. Bilotti, "Optical scattering cancellation through arrays of plasmonic nanoparticles: a review," in *Photonics*, vol. 2, no. 2. Multidisciplinary Digital Publishing Institute, 2015, pp. 540–552.

167. A. Alù and N. Engheta, "Polarizabilities and effective parameters for collections of spherical nanoparticles formed by pairs of concentric double-negative, single-negative, and/ or double-positive metamaterial layers," *Journal of Applied Physics*, vol. 97, no. 9, p. 094310, 2005.

168. U. Leonhardt, "Optical conformal mapping," *Science*, vol. 312, no. 5781, pp. 1777–1780, 2006.

169. D. Schurig, J. Mock, B. Justice, S. A. Cummer, J. B. Pendry, A. Starr, and D. Smith, "Metamaterial electromagnetic cloak at microwave frequencies," *Science*, vol. 314, no. 5801, pp. 977–980, 2006.

170. W. Cai, U. K. Chettiar, A. V. Kildishev, V. M. Shalaev, and G. W. Milton, "Nonmagnetic cloak with minimized scattering," *Applied Physics Letters*, vol. 91, no. 11, p. 111105, 2007.

171. G. Castaldi, I. Gallina, and V. Galdi, "Nearly perfect nonmagnetic invisibility cloaking: Analytic solutions and parametric studies," *Physical Review B*, vol. 80, no. 12, p. 125116, 2009.

172. G. Castaldi, I. Gallina, V. Galdi, A. Alù, and N. Engheta, "Power scattering and absorption mediated by cloak/anti-cloak interactions: A transformation-optics route toward invisible sensors," *JOSA B*, vol. 27, no. 10, pp. 2132–2140, 2010.

173. G.-H. Song and S.-Y. Shin, "Design of corrugated waveguide filters by the gel'fand–levitan–marchenko inverse-scattering method," *JOSA A*, vol. 2, no. 11, pp. 1905–1915, 1985.

174. P. P. Roberts and G. E. Town, "Design of microwave filters by inverse scattering," *IEEE Transactions on Microwave Theory and Techniques*, vol. 43, no. 4, pp. 739–743, 1995.

175. R. C. Rumpf, M. A. Fiddy, and M. E. Testorf, "Design of generalized invisible scatterers," *Optics Express*, vol. 15, no. 8, pp. 4735–4744, 2007.

176. L. Gubin, B. Polyak, and E. Raik, "The method of projections for finding the common point of convex sets," *USSR Computational Mathematics and Mathematical Physics*, vol. 7, no. 6, pp. 1–24, 1967.

177. R. Palmeri, M. T. Bevacqua, A. F. Morabito, and T. Isernia, "Inverse scattering methods as a tool for the design of GPCs devices," in *Antenna Measurements and Applications (CAMA), 2017 International Conference on.* IEEE, 2017, pp. 130—-132.

178. L. Crocco, F. Cuomo, and T. Isernia, "Improved scattering matrix method for the analysis of two-dimensional pbg devices," *Microwave and Optical Technology Letters*, vol. 48, no. 12, pp. 2564–2570, 2006.

179. ——, "Generalized scattering-matrix method for the analysis of two-dimensional photonic bandgap devices," *JOSA A*, vol. 24, no. 10, pp. A12–A22, 2007.

180. F. Cuomo, "An Effective "Mesoscopic" Approach for the Analysis of PBG-Based Structures and New Applications," PhD Thesis, Università "Mediterranea" di Reggio Calabria, 2007/2008.

181. R. Tibshirani, "Regression shrinkage and selection via the lasso," *Journal of the Royal Statistical Society. Series B (Methodological)*, pp. 267–288, 1996.

182. T. Isernia, P. Di Iorio, and F. Soldovieri, "An effective approach for the optimal focusing of array fields subject to arbitrary upper bounds," *IEEE Transaction on Antennas and Propagation*, vol. 48, no. 12, pp. 1837–1847, 2000.

183. O. Bucci, M. D'Urso, and T. Isernia, "Optimal synthesis of difference patterns subject to arbitrary sidelobe bounds by using arbitrary array antennas," *IEE Proceedings-Microwaves, Antennas and Propagation*, vol. 152, no. 3, pp. 129–137, 2005.

Publications

1. M. T. Bevacqua, L. Crocco, L. Di Donato, T. Isernia, and R. Palmeri, "Exploiting virtual experiments for the solution of inverse scattering problem," in *Electromagnetics in Advanced Applications (ICEAA), 2015 International Conference on.* IEEE, 2015, pp. 836–838.
2. L. Di Donato, R. Palmeri, G. Sorbello, T. Isernia, and L. Crocco, "Assessing the capabilities of a new linear inversion method for quantitative microwave imaging," *International Journal of Antennas and Propagation*, vol. 2015, 2015.
3. M. T. Bevacqua, L. Crocco, L. D. Donato, T. Isernia, and R. Palmeri, "Exploiting sparsity and field conditioning in subsurface microwave imaging of nonweak buried targets," *Radio Science*, vol. 51, no. 4, pp. 301–310, 2016.
4. L. Di Donato, R. Palmeri, G. Sorbello, T. Isernia, and L. Crocco, "A new linear distorted-wave inversion method for microwave imaging via virtual experiments," *IEEE Transactions on Microwave Theory and Techniques*, vol. 64, no. 8, pp. 2478–2488, 2016.
5. A. F. Morabito, R. Palmeri, and T. Isernia, "A compressive-sensing-inspired procedure for array antenna diagnostics by a small number of phaseless measurements," *IEEE Transactions on Antennas and Propagation*, vol. 64, no. 7, pp. 3260–3265, 2016.
6. M. T. Bevacqua, L. Crocco, L. Di Donato, R. Palmeri, and T. Isernia, "A 'virtual experiments' setting for inverse scattering problems," in *Antenna Technology and Applied Electromagnetics (ANTEM), 2016 17th International Symposium on.* IEEE, 2016, pp. 1–2.
7. M. T. Bevacqua, L. Crocco, L. Di Donato, T. Isernia, and R. Palmeri, "Virtual experiments and compressive sensing for subsurface microwave tomography," in *Compressive Sensing of Earth Observations.* CRC Press, 2017, ch. 8.
8. M. T. Bevacqua, R. Palmeri, L. Di Donato, L. Crocco, and T. Isernia, "Microwave imaging via iterated virtual experiments," in *Antennas and Propagation (EuCAP), 2016 10th European Conference on.* IEEE, 2016, pp. 1–5.
9. R. Palmeri, M. T. Bevacqua, L. Crocco, T. Isernia, and L. Di Donato, "Microwave imaging via distorted iterated virtual experiments," *IEEE Transactions on Antennas and Propagation*, vol. 65, no. 2, pp. 829–838, 2017.

10. R. Palmeri, M. T. Bevacqua, L. Di Donato, L. Crocco, and T. Isernia, "Microwave imaging of non-weak targets in stratified media via virtual experiments and compressive sensing," in *Antennas and Propagation (EUCAP), 2017 11th European Conference on*. IEEE, 2017, pp. 1711–1715.
11. T. Isernia, R. Palmeri, A. F. Morabito, and L. Di Donato, "Inverse scattering and compressive sensing as advanced e.m. design tool," in *International Symposium on Antennas and Propagation*. IEEE, 2017.
12. R. Palmeri, A. F. Morabito, and T. Isernia, "Design of a varying dielectric profile antenna generating reconfigurable Σ-Δ pattern via inverse scattering theory," in *Electromagnetics in Advanced Applications (ICEAA), 2017 International Conference on*. IEEE, 2017, pp. 1303–1306.
13. R. Palmeri, M. T. Bevacqua, R. Scapaticci, A. F. Morabito, L. Crocco, and T. Isernia, "Biomedical imaging via wavelet-based regularization and distorted iterated virtual experiments," in *Electromagnetics in Advanced Applications (ICEAA), 2017 International Conference on*. IEEE, 2017, pp. 1381–1384.
14. R. Palmeri, M. T. Bevacqua, A. F. Morabito, and T. Isernia, "Inverse scattering methods as a tool for the design of GPCs devices," in *Antenna Measurements and Applications (CAMA), 2017 International Conference on*. IEEE, 2017, pp. 130—-132.